UNIVERSITY OF SOUTHAMPTON

Isospin-breaking corrections and QED finite-volume effects for meson masses and the hadronic vacuum polarisation

by

James C. Harrison

ORCID 0000-0002-3643-0489

A thesis submitted for the degree of
Doctor of Philosophy

in the
Faculty of Engineering and Physical Sciences
Physics and Astronomy

March 2019

UNIVERSITY OF SOUTHAMPTON

ABSTRACT

FACULTY OF ENGINEERING AND PHYSICAL SCIENCES
PHYSICS AND ASTRONOMY

Doctor of Philosophy

ISOSPIN-BREAKING CORRECTIONS AND QED FINITE-VOLUME EFFECTS FOR MESON MASSES AND THE HADRONIC VACUUM POLARISATION

by James C. Harrison

The search for new physics requires experimental tests of the Standard Model, with the aim of identifying the limits of its validity. In an effort to produce more precise theoretical predictions with which to confront experimental results, lattice quantum chromodynamics calculations of some hadronic quantities are now reaching a precision at which isospin-breaking corrections become significant. An example is the hadronic vacuum polarisation (HVP) contribution to the muon anomalous magnetic moment. In the first part of this work, we compare two different methods for including electro-quenched QED corrections in lattice QCD calculations; a non-perturbative, stochastic approach, and a perturbative approach. We calculate isospin-breaking corrections to meson masses and the HVP on a $24^3 \times 64$ lattice with pion mass $m_\pi = 340\,\mathrm{MeV}$ and inverse lattice spacing $a^{-1} = 1.78\,\mathrm{GeV}$. We find agreement between results obtained using the two methods, up to $\mathcal{O}\left(\alpha^2\right)$ effects which are present only in the data from the stochastic method. We find that the electromagnetic correction to the HVP contribution to the muon anomalous magnetic moment is less than 1% for the up quark and 0.1% for the strange quark, and the strong isospin-breaking correction is $\approx 0.9\%$. These results constituted the first calculation of isospin-breaking corrections to the HVP, although this is an exploratory calculation at larger-than-physical light quark mass. Comparing the precision achievable with the same computational cost from each method, we find that the stochastic method can produce results with smaller statistical errors.

Large systematic effects typically arise as a result of restricting QED to a finite volume, and correcting for these effects in lattice calculations including QED is an important area of study. In the second part of this work, we develop a new technique for numerical calculation of QED finite volume effects using efficient lattice simulations of scalar QED. We verify the method by comparing numerical calculations of QED finite volume effects for the self energy of a scalar particle and for the HVP with analytical calculations of the same effects. We find that our numerical method can produce results with sufficiently high precision to resolve discretisation effects, and that after correcting for these effects our results agree with the analytical predictions up to exponentially-suppressed finite volume effects neglected in the analytical calculations. We find that the leading QED finite volume correction to the HVP is $\mathcal{O}\left(1/L^3\right)$, meaning that these effects are negligible in lattice calculations of the HVP at current achievable precision. We also implement a new technique to suppress QED finite volume effects by modifying the photon action, and demonstrate that it can be used to suppress the relative size of scalar mass finite volume effects to less than 1%. The numerical method we have developed is applicable to a wider range of processes, towards cases where analytical computations would be difficult.

Contents

List of Figures

List of Tables

List of Accompanying Materials

Dataset for Isospin-breaking corrections and QED finite-volume effects for meson masses and the hadronic vacuum polarisation, DOI: 10.5258/SOTON/D0852

Acronyms

CG	Conjugate gradient
EM	Electromagnetism
FFT	Fast Fourier transform
FV	Finite volume
HLbL	Hadronic light-by-light
HMC	Hybrid Monte Carlo
HVP	Hadronic vacuum polarisation
IR	Infrared
LO	Leading order
NLO	Next-to-leading order
NNLO	Next-to-next-to-leading order
NRQED	Non-relativistic QED
QCD	Quantum chromodynamics
QED	Quantum electrodynamics
SM	Standard Model
StN	Signal-to-noise
SUSY	Supersymmetry
UV	Ultraviolet

Declaration of Authorship

I, James C. Harrison, declare that this thesis entitled *Isospin-breaking corrections and QED finite-volume effects for meson masses and the hadronic vacuum polarisation* and the work presented in it are my own and have been generated by me as the result of my own original research.

I confirm that:

1. This work was done wholly or mainly while in candidature for a research degree at this University;
2. Where any part of this thesis has previously been submitted for a degree or any other qualification at this University or any other institution, this has been clearly stated;
3. Where I have consulted the published work of others, this is always clearly attributed;
4. Where I have quoted from the work of others, the source is always given. With the exception of such quotations, this thesis is entirely my own work;
5. I have acknowledged all main sources of help;
6. Where the thesis is based on work done by myself jointly with others, I have made clear exactly what was done by others and what I have contributed myself;
7. Parts of this work have been published as [3–7], or submitted for publication as [8].

Signed:

Date:

Acknowledgements

I would like to thank my supervisor, Andreas Jüttner, for all of his support and guidance throughout my PhD. I would also like to thank Antonin Portelli, whose help and advice has been very valuable.

I would like to thank Vera Gülpers, with whom I worked closely on the comparative study of isospin-breaking methods presented in this work, and also my other co-authors Chris Sachrajda, Christoph Lehner, Martin Savage, Zohreh Davoudi, Tadeusz Janowski, Nils Hermansson Truedsson and Hans Bijnens for their collaboration. I am particularly grateful to Peter Boyle for his effort developing the Grid library, which has been of great value for my research.

I am grateful to members of the RBC/UKQCD collaboration, with whom I have had useful conversations, and particularly to Norman Christ for hosting me at Columbia University for a month.

I extend my thanks to past and present members of the lattice group in Southampton, especially to Matt Spraggs, Tobi Tsang and Francesco Sanfilippo for helping me to understand concepts of lattice QCD.

Finally, I am extremely grateful to Emma for her huge support at all times, and to Astrid for reminding me to stop working and feed her at regular intervals.

I am supported financially by the EPSRC Centre for Doctoral Training in Next Generation Computational Modelling grant EP/L015382/1. I acknowledge computational resources used on the Hyak High performance Computing and Data Ecosystem at the UW, the IRIDIS High Performance Computing Facility at the University of Southampton, and DiRAC HPC facilities including the Blue Gene Q Shared Petaflop system and Tesseract Extreme Scaling service at the University of Edinburgh.

Chapter 1

Introduction

The Standard Model (SM) is currently our best theoretical description of the universe at the smallest length scales, and has been verified by many experimental measurements [9–12]. However, there are observations that the SM is unable to explain, including the nature of dark matter and dark energy [13], and it is also unable to describe gravitational interactions. Physicists hope that, by improving the precision of both theoretical predictions and experimental measurements, a discrepancy between the SM and experiment will be found which gives clues as to the nature of new physics beyond the SM. While there are discrepancies between SM predictions and experimental measurements of some quantities, none have yet reached the significance of 5 standard deviations required to constitute a discovery of new physics [10].

One example of a quantity for which there is a discrepancy between theory and experiment is the muon anomalous magnetic moment, a_μ. For many years there has been a tension between Standard Model predictions and experimental measurements of a_μ, which currently stands at 3.5 standard deviations [10]. New experiments E989 at Fermilab [14] and E34 at J-PARC [15] are set to reduce the experimental error in the measurement, and the proposed MUonE experiment [16] will measure the leading-order hadronic contribution to a_μ. It is therefore important to also increase the precision of the SM prediction. The largest source of theoretical uncertainty in the SM prediction of a_μ comes from the hadronic sector, described by quantum chromodynamics (QCD) [10].

The low-energy regime of QCD cannot be studied from first principles using perturbative techniques, due to the strong coupling. Lattice QCD is a non-perturbative numerical approach which can be used to calculate QCD expectation values. Until recently, lattice QCD calculations usually used an isospin-symmetric approximation, in which electromagnetic interactions are neglected and the up and down quarks are treated as identical particles. This choice was justified, as isospin-breaking corrections enter at $\mathcal{O}(\alpha)$ and $\mathcal{O}\left((m_d - m_u)/\Lambda_{\mathrm{QCD}}\right)$, where α is the fine-structure constant, m_u and m_d are the masses of the up and down quarks, respectively, and Λ_{QCD} is the energy scale at which QCD becomes strongly coupled, and these corrections are therefore expected to be $\mathcal{O}(1\%)$ of the isospin-symmetric values. Until recently, these effects were smaller than the typical error in lattice QCD results, and could therefore be neglected. However, lattice calculations of some quantities, including the leading hadronic contribution to a_μ, are now approaching 1% precision [17], at which point isospin-breaking corrections become important.

There are challenges involved with the inclusion of isospin-breaking effects in lattice QCD calculations. The numerical simulations involved in lattice QCD require significant computational resources, and this computational cost is increased by the necessity to treat up and down quarks as non-identical particles. Several methods for including electromagnetic effects on the lattice have been developed and used by different groups within the lattice QCD community [18–25]. In the first part of this work, we make a direct comparison of results from two commonly-used methods, in order to establish which method produces the more precise results. We also assess practical issues with the interpretation of results from these methods. As a part of this comparative study we also make a first exploratory calculation of isospin-breaking corrections to the leading hadronic contribution to a_μ, for unphysical simulation parameters, and find that they are of the order of 1%, as expected [3].

A further issue arises when electromagnetic interactions are included in lattice QCD calculations. These interactions have an infinite range, and electromagnetic corrections therefore suffer from large systematic effects when restricted to a finite volume [21]. Calculations of these finite volume (FV) effects are required so that they can be used to correct lattice results. In the second part of this work we develop a numerical framework for calculating electromagnetic FV effects. We compare our numerical calculations of FV effects with analytical predictions, to validate both the numerical method and the analytical calculations, and we demonstrate that electromagnetic FV effects are negligible in lattice calculations of a_μ at the precision currently achievable [7, 8]. We also implement a method to suppress electromagnetic FV effects in lattice calculations, and demonstrate its effect on calculations of the mass of a scalar particle.

This thesis begins with a review of some theoretical details. In Chapter 2 I introduce the Standard Model, with a particular focus on quantum electrodynamics (QED), the theory describing electromagnetic interactions, and QCD, describing the strong interaction. Chapter 3 contains an overview of lattice quantum field theory, including the formulation of QCD on a discrete space-time lattice, calculating correlation functions on the lattice, and methods for extracting observables from lattice simulation data. Chapter 4 introduces the muon anomalous magnetic moment, with an overview of experimental measurements and SM predictions of a_μ, followed by a method for calculating the hadronic vacuum polarisation (HVP) from lattice QCD, and the connection between the HVP and the leading hadronic contribution to a_μ. The chapter concludes with a brief review of lattice calculations of the HVP and its contribution to a_μ.

Chapter 5 begins with an overview of efforts to include isospin-breaking corrections in lattice QCD calculations. This is followed in Sec. 5.1 by a formulation of QED on the lattice. Sec. 5.2 introduces a non-perturbative method for calculating QED corrections to hadronic observables through the stochastic generation of QED gauge field configurations, a method which we call the "stochastic method". Sec. 5.3 describes an alternative method to calculate QED corrections, through a perturbative expansion of correlators in powers of the electromagnetic coupling. We refer to this method as the "perturbative method". The chapter finishes with a brief discussion of isospin-breaking effects arising from the different masses of the up and down quarks in Sec. 5.4.

An exploratory study of isospin-breaking corrections using both the stochastic and the perturbative method is presented in Chapter 6. Parameters used in the simulations are summarised in Sec. 6.1. In Sec. 6.2, we calculate isospin-breaking corrections to pseudoscalar meson masses. We start by introducing two different techniques required to extract mass corrections from data generated using the two different methods, before comparing results from the two methods

and checking that they are consistent. We calculate isospin-breaking corrections to the HVP in Sec. 6.3, and again compare results from the two methods. In Sec. 6.4, statistical errors in results calculated using the two methods are compared.

In Chapter 7 we present a numerical study of QED finite volume effects. After a review of previous work, an efficient numerical method for calculating QED FV effects using lattice simulations of scalar QED is detailed in Sec. 7.1. This method is applied to the calculation of QED FV effects for the self energy of a scalar particle in Sec. 7.2, extending previous calculations of scalar mass FV effects. A detailed derivation of methods for extracting the self energy from lattice correlators, and a calculation of excited-state contributions which contaminate the lattice data, is followed by a comparison of data from our numerical calculations with analytical expressions. The section finishes with the implementation of a method to suppress QED FV effects by modifying the photon action, which we call "infrared improvement". In Sec. 7.3, our numerical method is applied to calculate QED FV effects for the HVP. We first derive the conserved vector current in our lattice formulation of scalar QED, before describing the method used to calculate QED FV effects for the HVP numerically. After deriving the counterterms necessary to renormalise the calculation, our numerical results are compared with analytical calculations of the FV effects.

Finally, we summarise our results and draw conclusions in Chapter 8.

Chapter 2

The Standard Model

There are four fundamental interactions which describe the phenomena seen in nature. These are the electromagnetic and gravitational interactions, which are familiar in our macroscopic experience of the universe, along with two short-range interactions: the weak interaction, which is responsible for radioactive decay, and the strong interaction, which binds together atomic nuclei. The Standard Model (SM) provides a theoretical description of the electromagnetic, weak and strong interactions as consequences of local gauge symmetries.

The SM has been verified through many experimental tests [9–12], but there are observations which it fails to explain. These include the existence of dark matter, inferred from astrophysical and cosmological observations including galaxy rotation curves [26] and the cosmic microwave background [13], and the non-zero neutrino masses required to explain experimentally-observed neutrino oscillations [27, 28]. There are other measurements which are showing tension with SM predictions, although none are yet significant at 5 standard deviations, the accepted requirement for a new discovery in particle physics [10]. One example of such a tension is the muon anomalous magnetic moment [1], for which there is currently a 3.5σ discrepancy between experimental measurements and SM predictions [10]. This will be discussed further in Chapter 4. It is hoped that by improving the precision of both experimental measurements and SM predictions, discrepancies will be found which can give clues as to the nature of new physics beyond the SM.

In this chapter we will introduce the SM, with a particular focus on the electromagnetic and strong interactions, which play an important role in this work. We start by summarising the particle content of the SM in Sec. 2.1. An action describing free fermions is introduced in Sec. 2.2, and this is modified in Sec. 2.3 to produce an action which is invariant under local U(1) gauge transformations. This section also summarises a procedure for fixing the gauge in a quantum field theory. In Sec. 2.4 the theory of quantum electrodynamics (QED), which describes electromagnetic interactions in a quantum field theory, is introduced. The U(1) gauge-symmetric action is generalised to the case of non-Abelian SU(N) symmetries in Sec. 2.5, and this is used to define the theory of quantum chromodynamics (QCD), which describes the strong interaction, in Sec. 2.6. The electroweak theory, describing the weak and electromagnetic interactions, is introduced in Sec. 2.7 along with the Higgs mechanism which breaks electroweak symmetry. Sec. 2.8 introduces Ward identities, and the chapter finishes in Sec. 2.9 with a discussion of chiral symmetry in QCD, including the isospin symmetry which is of particular relevance to the work presented in this thesis.

2.1 Particle content

The SM is described by an action which is invariant under Lorentz and local $\mathrm{SU}(3)\times\mathrm{SU}(2)\times\mathrm{U}(1)$ gauge transformations.

The elementary particles of the SM can be categorised according to their spin. The fermions have spin $\frac{1}{2}$ and are described by anti-commutative spinor fields, and the bosons have integer spin and are commutative.

There are twelve fermions which fall into three generations, with particles in different generations differing only by their masses. The fermions are further categorised into quarks, which interact via all three of the fundamental gauge interactions, and leptons which do not interact via the strong interaction. The leptons consist of the electron and its heavier cousins the muon and tau, which have charge -1, and the neutrinos (one for each generation of electron-type lepton) which are electromagnetically neutral and only interact through the weak interaction. Within the SM, neutrinos are massless particles, although experimental observations of neutrino oscillations show that they actually have very small but non-zero masses [10, 27, 28].

The up-type quarks (up, charm and top) have electromagnetic charge $+\frac{2}{3}$, and the down-type quarks (down, strange and bottom) have charge $-\frac{1}{3}$ (in units of the positron charge e). The quarks also carry a colour charge, with three components labelled red, green and blue, which describes their coupling to the strong interactions. At low energies the theory of strong interactions exhibits confinement, causing quarks to be bound together into colour-neutral states called hadrons. The hadrons fall into two categories: baryons, consisting of three quarks, and mesons, consisting of one quark and one anti-quark. The property of confinement will be introduced in more detail in Sec. 2.6.

The three gauge interactions are mediated by vector bosons, with spin 1. Electromagnetism is carried by the photon, which is a massless, chargeless boson. The massive $W^{\pm}$ and Z bosons carry the weak interaction, and their masses are responsible for the short range of this interaction. The $W^{\pm}$ bosons have charges ±1 and therefore interact electromagnetically, while the Z is charge-neutral. The strong interaction is carried by the gluons. Like the photon, gluons are massless and charge-neutral. The finite range of the strong interaction is due to confinement.

The SM also contains the Higgs boson, a scalar boson (spin 0) which is responsible for the masses of the weak bosons through spontaneous symmetry breaking. The recent experimental detection of the Higgs boson at the LHC completed the experimental verification of the matter content of the SM [11, 12].

Some properties of the SM elementary particles are summarised in Table 2.1.

2.2 The Dirac fermion action

The action for a fermion ψ, without interactions, is [29]

$$S_{\mathrm{Dirac}}\left[\psi.\bar{\psi}\right] = \int d^4x\, \bar{\psi}\left(x\right) D\psi\left(x\right) \,, \tag{2.1}$$

where D is the Dirac operator

Particle	Spin	EM charge	Interactions
up-type quarks (u,c,t)	$\frac{1}{2}$	$+\frac{2}{3}$	EM, strong, weak
down-type quarks (d,s,b)	$\frac{1}{2}$	$-\frac{1}{3}$	EM, strong, weak
charged leptons (e,μ,τ)	$\frac{1}{2}$	-1	EM, weak
neutrinos (ν_e,ν_μ,ν_τ)	$\frac{1}{2}$	0	weak
photon (γ)	1	0	EM
$W^\pm$	1	± 1	EM, weak
Z	1	0	weak
gluons (g)	1	0	strong
Higgs (H)	0	0	weak

TABLE 2.1: Summary of the Standard Model particles, along with some of their properties.

$$D = i\gamma^\mu \partial_\mu - m\,, \tag{2.2}$$

and m is the mass of the fermion. Throughout this chapter we will use the Einstein summation convention, where repeated indices are summed over. The Dirac gamma matrices γ_μ are 4×4 matrices which obey the Clifford algebra [30]

$$\{\gamma_\mu, \gamma_\nu\} = 2g_{\mu\nu}\mathbb{1}\,. \tag{2.3}$$

In the chiral representation, the gamma matrices are

$$\gamma^0 = \begin{pmatrix} 0 & \mathbb{1} \\ \mathbb{1} & 0 \end{pmatrix}, \qquad \gamma^i = \begin{pmatrix} 0 & \sigma_i \\ -\sigma_i & 0 \end{pmatrix}, \tag{2.4}$$

where each element here represents a 2×2 matrix, and σ_i are the Pauli matrices [31]

$$\sigma_1 = \begin{pmatrix} 0 & 1 \\ 1 & 0 \end{pmatrix}, \qquad \sigma_2 = \begin{pmatrix} 0 & -i \\ i & 0 \end{pmatrix}, \qquad \sigma_3 = \begin{pmatrix} 1 & 0 \\ 0 & -1 \end{pmatrix}. \tag{2.5}$$

In this representation, the four-component spinor ψ can be written $\psi = \begin{pmatrix} \psi_L \\ \psi_R \end{pmatrix}$, where ψ_L and ψ_R are the left-handed and right-handed components of ψ, respectively.

We can define a fifth gamma matrix $\gamma_5 = i\gamma_0\gamma_1\gamma_2\gamma_3$, which satisfies $\{\gamma_5, \gamma_\mu\} = 0$. In the chiral representation this takes the form

$$\gamma^5 = \begin{pmatrix} -\mathbb{1} & 0 \\ 0 & \mathbb{1} \end{pmatrix}. \tag{2.6}$$

Using γ_5 we can define the chiral projection operators

$$P_{\pm} = \frac{1}{2}\left(\mathbb{1} \pm \gamma_5\right) , \tag{2.7}$$

such that $\psi_L = P_- \psi$ and $\psi_R = P_+ \psi$. The only term in the action which mixes the left- and right-handed components is $m\bar{\psi}\psi = m\left(\bar{\psi}_L \psi_R + \bar{\psi}_R \psi_L\right)$, so for massless fermions these components are independent, resulting in chiral symmetry which will be discussed in Sec. 2.9.

2.3 U(1) gauge symmetry

2.3.1 U(1) gauge-invariant action

In addition to Lorentz invariance, the Dirac action in Eq. (2.1) is invariant under a global U(1) transformation $\psi \to e^{i\omega}\psi$, for constant phase ω. However, if the phase ω is allowed to vary with position (i.e. $\psi(x) \to e^{i\omega(x)}\psi(x)$) then the action is not invariant due to the derivative in the Dirac operator acting on the phase factor $e^{i\omega(x)}$. The action can be made gauge invariant under local U(1) gauge transformations by replacing the derivative ∂_μ by a gauge-covariant derivative

$$D_\mu = \partial_\mu + igA_\mu , \tag{2.8}$$

where A_μ is a vector gauge field which transforms as

$$A_\mu(x) \to A_\mu(x) + \frac{1}{g}\partial_\mu \omega(x) , \tag{2.9}$$

and g is the coupling of the gauge field to the fermion. We can also include in the action any Lorentz- and gauge-invariant term which depends only on A_μ. The most general U(1) gauge-invariant action is

$$S\left[\psi, \bar{\psi}, A\right] = \int d^4x \, \left(\mathcal{L}_\psi[\psi, \bar{\psi}, A] + \mathcal{L}_A[A]\right) , \tag{2.10}$$

$$\mathcal{L}_\psi[\psi, \bar{\psi}, A] = \bar{\psi}\left(x\right)\left(i\gamma^\mu D_\mu - m\right)\psi\left(x\right) , \tag{2.11}$$

$$\mathcal{L}_A[A] = -\frac{1}{4}F^{\mu\nu}(x)F_{\mu\nu}(x) , \tag{2.12}$$

where $F_{\mu\nu}$ is the antisymmetric field strength tensor

$$F_{\mu\nu}(x) = [D_\mu, D_\nu](x) = \partial_\mu A_\nu(x) - \partial_\nu A_\mu(x) . \tag{2.13}$$

2.3.2 Quantisation and gauge fixing

A quantum field theory described by the action in Eq. (2.10) can be derived by defining the expectation value of an observable O through the path integral [32]

$$\langle O \rangle = \frac{1}{Z}\int \mathcal{D}\left[\psi, \bar{\psi}, A\right] O\left[\psi, \bar{\psi}, A\right] e^{iS\left[\psi, \bar{\psi}, A\right]} , \tag{2.14}$$

where $\mathcal{D}\left[\psi, \bar{\psi}, A\right]$ is the integration measure and the integral runs over all possible configurations of the fields ψ, $\bar{\psi}$ and A_μ. The partition function

$$Z = \int \mathcal{D}\left[\psi, \bar{\psi}, A\right] e^{iS\left[\psi, \bar{\psi}, A\right]} \tag{2.15}$$

normalises the path integral so that $\langle 1 \rangle = 1$.

Since the action is invariant under a U(1) gauge transformation, physical observables must also be gauge invariant. As a result, integrating over all possible field configurations includes integration over an infinite set of physically equivalent fields. For the path integral to be well-defined, the integral over the gauge field A_μ must be restricted to a domain over which all field configurations are physically distinct. Such a domain can be described by a gauge-fixing condition $F[A_\mu] = 0$, and choices for this condition include the Lorenz gauge $F[A_\mu] = \partial^\mu A_\mu$ [33] and the Coulomb gauge $F[A_\mu] = \partial_i A_i$, $i = 1, 2, 3$ [34].

The following procedure can be used to fix the gauge in the path integral [35]. Considering a gauge transformation $A_\mu \to A^\omega_\mu = A_\mu + \frac{1}{g}\partial_\mu \omega$, we have the identity

$$\int \mathcal{D}\omega \delta\left(F\left[A^\omega_\mu\right]\right) \det\left(\frac{\delta F\left[A^\omega_\mu\right]}{\delta \omega}\right) \equiv 1\,, \tag{2.16}$$

Inserting this into Eq. (2.14) gives

$$\langle O \rangle = \frac{1}{Z} \int \mathcal{D}\left[\psi, \bar{\psi}, A\right] \mathcal{D}\omega \delta\left(F\left[A^\omega_\mu\right]\right) \det\left(\frac{\delta F\left[A^\omega_\mu\right]}{\delta \omega}\right) O\left[\psi, \bar{\psi}, A\right] e^{iS\left[\psi, \bar{\psi}, A\right]}\,. \tag{2.17}$$

We can see from Eq. (2.9) that $\det\left(\delta F\left[A^\omega_\mu\right]/\delta\omega\right)$ is independent of A_μ, so this can be factorised out of the integral over A_μ. As the action and the operator O are gauge-invariant, we can change the variable $A^\omega_\mu \to A_\mu$. The integral over ω can then be factorised out, leaving

$$\langle O \rangle = \frac{1}{Z}\left[\int \mathcal{D}\omega \det\left(\frac{\delta F\left[A^\omega_\mu\right]}{\delta \omega}\right)\right] \int \mathcal{D}\left[\psi, \bar{\psi}, A\right] \delta\left(F\left[A_\mu\right]\right) O\left[\psi, \bar{\psi}, A\right] e^{iS\left[\psi, \bar{\psi}, A\right]}\,. \tag{2.18}$$

The same factorisation can be applied to the partition function, so that the integral over ω cancels, and the gauge-fixed path integral is

$$\langle O \rangle = \frac{1}{Z} \int \mathcal{D}\left[\psi, \bar{\psi}, A\right] \delta\left(F\left[A_\mu\right]\right) O\left[\psi, \bar{\psi}, A\right] e^{iS\left[\psi, \bar{\psi}, A\right]}\,, \tag{2.19}$$

$$Z = \int \mathcal{D}\left[\psi, \bar{\psi}, A\right] \delta\left(F\left[A_\mu\right]\right) e^{iS\left[\psi, \bar{\psi}, A\right]}\,. \tag{2.20}$$

Alternatively, the Dirac delta function $\delta\left(F\left[A_\mu\right]\right)$ can be replaced by a Gaussian function [35]:

$$\langle O \rangle = \frac{1}{Z} \int \mathcal{D}\left[\psi, \bar{\psi}, A\right] O\left[\psi, \bar{\psi}, A\right] e^{iS\left[\psi, \bar{\psi}, A\right]} e^{-i\frac{1}{2\xi}\int d^4x F[A_\mu(x)]^2}\,. \tag{2.21}$$

Choosing $F[A_\mu] = \partial^\mu A_\mu$, this defines the R_ξ gauges. In the limit $\xi \to 0$ this is the Landau gauge [36], which is equivalent to the Lorenz gauge, and the choice $\xi = 1$ defines the Feynman gauge [37].

2.4 Quantum electrodynamics

In a classical field theory defined by the action in Eq. (2.10), the Euler-Lagrange equation for the field ψ is the Dirac equation [29]

$$(i\gamma^\mu D_\mu - m)\,\psi = 0\,, \tag{2.22}$$

and the Euler-Lagrange equations for A_μ are Maxwell's equations of electromagnetism

$$\partial_\mu F^{\mu\nu} = j^\nu\,, \tag{2.23}$$

with $j^\nu = g\bar{\psi}\gamma^\nu\psi$. After quantisation, this is a quantum field theory describing the electromagnetic interactions of fermion fields ψ with photon fields A_μ, and the coupling g is the electromagnetic charge of the fermion. This is the theory of quantum electrodynamics (QED) [37–44], and the U(1) symmetry corresponds to conservation of the electromagnetic current $j^\mu(x)$, as will be shown in Sec. 2.8.

The charge of an electron is $-e$, where e is usually expressed through the fine structure constant $\alpha = \frac{e^2}{4\pi} \approx \frac{1}{137}$. Expectation values in QED can be calculated by Taylor expanding the path integral in powers of e. Since the action is invariant under charge conjugation $e \to -e$, physical observables must also share this symmetry, and therefore terms in the expansion with odd powers of e cannot contribute. Each successive term in the expansion of the path integral has one higher power of α than the previous term, and thus gives an $\mathcal{O}(1\%)$ correction. A full result can be obtained with a given precision by calculating all terms in the path integral expansion up to sufficiently high order in α.

There is a problem which arises when attempting to make these perturbative calculations. Beyond the leading order, Feynman diagrams involve integration over the momentum in closed loops, and some of these integrals are divergent. As a result, calculations of expectation values give infinite results. In QED there are three divergent one-loop diagrams, shown in Fig. 2.1. A solution to this problem is to "renormalise" the theory by absorbing the infinities into the parameters of the theory [45, 46]. Denoting the bare parameters with a subscript 0, we can define renormalised parameters by introducing renormalisation constants:

$$\psi_0 = \sqrt{Z_\psi}\psi_R\,, \quad A_0^\mu = \sqrt{Z_A}A_R^\mu\,, \quad m_0 = Z_m m_R\,, \quad g_0 = Z_g g_R\,. \tag{2.24}$$

The constants Z_i can be chosen to absorb the infinite parts of the divergent terms, so that the renormalised parameters are finite. The Lagrangian can be written as a sum of two contributions $\mathcal{L} = \mathcal{L}_R + \mathcal{L}_{CT}$, where $\mathcal{L}_R$ is the original Lagrangian with bare parameters replaced by renormalised ones, and $\mathcal{L}_{CT}$ depends on the renormalisation constants. Additional tree-level diagrams, called counterterms, arise from the Lagrangian $\mathcal{L}_{CT}$, and these counterterms cancel

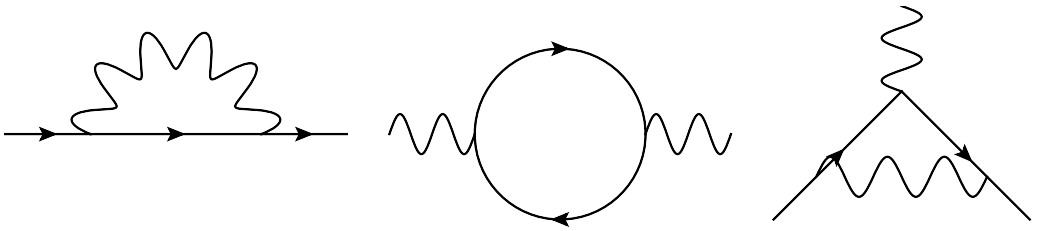

FIGURE 2.1: The three divergent one-loop diagrams in QED: self-energy, vacuum polarisation and vertex correction.

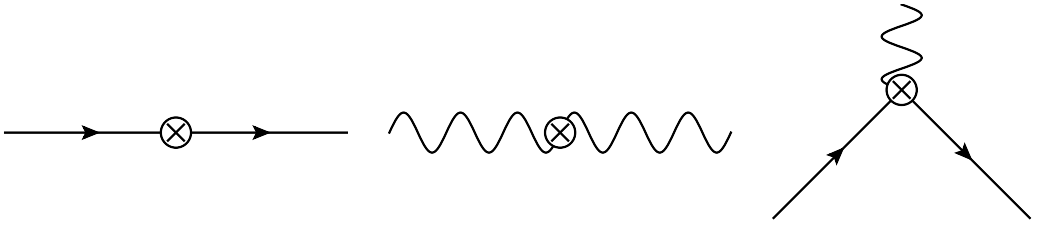

FIGURE 2.2: The three counterterms which cancel the divergent one-loop diagrams shown in Fig. 2.1.

the infinite parts of the divergent one-loop terms. The three counterterms in QED are shown in Fig. 2.2.

A consequence of this renormalisation procedure is that the renormalised parameters depend on the energy scale at which they are defined.

2.5 SU(N) gauge symmetry

Suppose that the fermion field ψ in Eq. (2.1) is not just a single fermion, but a multiplet of N fermion fields $\psi^i(x)$, $i = 1, \ldots, N$. The free fermion action in this case is invariant under a global SU(3) rotation $\psi(x) \to e^{i\omega^a T^a}\psi(x)$, where the $N^2 - 1$ matrices T^a are the generators of the group SU(N). The T^a are basis elements of the Lie algebra su(N), which obey

$$\left[T^a, T^b\right] = if^{abc}T^c\,, \tag{2.25}$$

where f^{abc} are the fully antisymmetric structure constants of su(N). This global symmetry of the action can be promoted to a local gauge symmetry $\psi(x) \to e^{i\omega^a(x)T^a}\psi(x)$ by replacing the partial derivative by the gauge-covariant derivative

$$D_\mu = \partial_\mu + igA^a_\mu(x)T^a\,, \tag{2.26}$$

with vector fields A^a_μ which transform as $A^a_\mu(x) \to A^a_\mu(x) + \frac{1}{g}D_\mu\omega^a(x)$.

Defining a field strength tensor $F_{\mu\nu} = [D_\mu, D_\nu]$, as in the U(1) case, we find $F_{\mu\nu} = F^a_{\mu\nu}T^a$, where

$$F^a_{\mu\nu}(x) = \partial_\mu A^a_\nu(x) - \partial_\nu A^a_\mu(x) - gf^{abc}A^b_\mu(x)A^c_\mu(x)\,, \tag{2.27}$$

and we can define a local SU(N) gauge-invariant Lagrangian [47]

$$\mathcal{L}\left[\psi,\bar{\psi},A\right]=\bar{\psi}\left(x\right)\left(i\gamma^{\mu}D_{\mu}-m\right)\psi\left(x\right)-\frac{1}{4}F^{\mu\nu,a}(x)F^{a}_{\mu\nu}(x)\,. \tag{2.28}$$

One significant difference between this theory and QED is the term $gf^{abc}A^{b}_{\mu}(x)A^{c}_{\mu}(x)$ in the field strength tensor. As a result, terms involving three or four vector fields A^{a}_{μ} appear in the Lagrangian, leading to self-interactions of the gauge bosons through three-boson and four-boson vertices. A further consequence, which is not relevant for the work presented here, is that the Jacobian determinant in Eq. (2.17) depends on the gauge field and cannot be factorised out of the path integral. This complicates the gauge-fixing procedure due to the introduction of unphysical degrees of freedom [35].

2.6 Quantum chromodynamics

The theory of quantum chromodynamics (QCD) describes the strong interaction, which couples quarks and gluons. Quarks carry colour charge, and are represented as triplets of spinor fields ψ^{i}, $i=r,g,b$. QCD is described by the SU(3) gauge-invariant Lagrangian [48, 49]

$$\mathcal{L}_{\mathrm{QCD}}\left[\psi,\bar{\psi},A\right]=\sum_{f}\bar{\psi}_{f}\left(x\right)\left(i\gamma^{\mu}D_{\mu}-m_{f}\right)\psi_{f}\left(x\right)-\frac{1}{4}F^{\mu\nu,a}(x)F^{a}_{\mu\nu}(x)\,, \tag{2.29}$$

where the index f runs over the six quark flavours. The field strength tensor $F^{a}_{\mu\nu}$ is defined as in Eq. (2.27), where $A^{a}_{\mu}(x)$ are the eight gluon fields. The covariant derivative is $D_{\mu}=\partial_{\mu}+ig_{s}A^{a}_{\mu}(x)t^{a}$, where g_{s} is the strong coupling and the generators of SU(3) are the 3×3 matrices $t^{a}=\frac{1}{2}\lambda_{a}$, where λ_{a} are the Gell-Mann matrices [49]

$$\lambda_{1}=\begin{pmatrix}0&1&0\\1&0&0\\0&0&0\end{pmatrix},\quad \lambda_{2}=\begin{pmatrix}0&-i&0\\i&0&0\\0&0&0\end{pmatrix},\quad \lambda_{3}=\begin{pmatrix}1&0&0\\0&-1&0\\0&0&0\end{pmatrix},$$
$$\lambda_{4}=\begin{pmatrix}0&0&1\\0&0&0\\1&0&0\end{pmatrix},\quad \lambda_{5}=\begin{pmatrix}0&0&-i\\0&0&0\\i&0&0\end{pmatrix},\quad \lambda_{6}=\begin{pmatrix}0&0&0\\0&0&1\\0&1&0\end{pmatrix},$$
$$\lambda_{7}=\begin{pmatrix}0&0&0\\0&0&-i\\0&i&0\end{pmatrix},\quad \lambda_{8}=\frac{1}{\sqrt{3}}\begin{pmatrix}1&0&0\\0&1&0\\0&0&-2\end{pmatrix}. \tag{2.30}$$

In analogy with the perturbative approach used to calculate QED processes, one could attempt to make QCD calculations by expanding the path integral in powers of the strong coupling g_{s}. However, this approach is only valid when the coupling is a small parameter, $g_{s}\ll1$. The renormalised strong coupling constant $\alpha_{s}=\frac{g_{s}}{4\pi}$ at energy scale μ is [50, 51]

$$\alpha_{s}\left(\mu^{2}\right)=\frac{2\pi}{\left(11-\frac{2}{3}N_{f}\right)\ln\left(\frac{\mu^{2}}{\Lambda^{2}_{\mathrm{QCD}}}\right)}\,, \tag{2.31}$$

where N_f is the number of quark flavours. The coupling constant $\alpha_s \to 0$ as $\mu \to \infty$, a property called asymptotic freedom [50, 51]. The coupling constant has a pole at the QCD scale $\mu = \Lambda_{\mathrm{QCD}}$, which is empirically observed to be $\Lambda_{\mathrm{QCD}} \sim 300\,\mathrm{MeV}$ [10]. At low energy the coupling constant $g_s \sim \mathcal{O}(1)$, and QCD becomes non-perturbative. This leads to the property of confinement, whereby the degrees of freedom of QCD at low energy are not quarks and gluons, but colour singlet states known as hadrons [52]. The hadrons fall into two categories: baryons, which are fermionic bound states of three quarks $\psi^r_{f_1}\psi^g_{f_2}\psi^b_{f_3}$, and mesons, which are bosonic states $\bar{\psi}^i_{f_1}\psi^i_{f_2}$ containing one quark and one anti-quark. Confinement leads to QCD having a mass gap, with the lightest states having a mass of $\mathcal{O}(\Lambda_{\mathrm{QCD}})$. The properties of hadrons cannot be studied using perturbation theory, and a non-perturbative approach is required to investigate QCD at low energies. One such approach is lattice QCD, which will be introduced in Chapter 3.

2.7 Electroweak sector

2.7.1 $\mathrm{SU}(2)_L \times \mathrm{U}(1)_Y$ symmetry

In the SM, the weak and electromagnetic interactions are combined in the electroweak theory [53–55]. The symmetry of the electroweak theory is $\mathrm{SU}(2)_L \times \mathrm{U}(1)_Y$, where the symmetry $\mathrm{SU}(2)_L$ applies only to the left-handed components of fermions, and the symmetry $\mathrm{U}(1)_Y$ corresponds to the conserved weak hypercharge Y. The left-handed fermion components are placed into SU(2) doublets

$$\Psi_L^{\mathrm{lepton}} = \begin{pmatrix} \nu_L \\ \ell_L \end{pmatrix}, \qquad \Psi_L^{\mathrm{quark}} = \begin{pmatrix} u_L \\ d_L \end{pmatrix}, \tag{2.32}$$

and the right-handed components Ψ_R are singlets. As the SM neutrinos are massless, and the mass term is the only source of mixing between the left-handed and right-handed components, the right-handed neutrinos are completely decoupled from the theory, and therefore do not appear in the SM.

The Lagrangian describing the dynamics of these fermions is

$$\mathcal{L}[\Psi_L, \Psi_R, W, B] = \sum_i \left[\bar{\Psi}_{L,i}(x)\left(i\gamma^\mu D_\mu\right)\Psi_{L,i}(x) + \bar{\Psi}_{R,i}(x)\left(i\gamma^\mu D_\mu\right)\Psi_{R,i}(x)\right] - \frac{1}{4}F^{\mu\nu}(x)F_{\mu\nu}(x), \tag{2.33}$$

where $F_{\mu\nu} = [D_\mu, D_\nu]$ and the covariant derivatives acting on the left-handed and right-handed fields are

$$D_\mu \Psi_L(x) = \left(\partial_\mu + igW^a_\mu(x)\tau^a + \frac{i}{2}g'B_\mu(x)Y\right)\Psi_L(x), \tag{2.34}$$

$$D_\mu \Psi_R(x) \left(\partial_\mu + \frac{i}{2}g'B_\mu(x)Y\right)\Psi_R(x). \tag{2.35}$$

The SU(2) generators are $\tau^a = \frac{1}{2}\sigma^a$, where σ^a are the Pauli matrices defined in Eq. (2.5). This Lagrangian is invariant under rotations of the form $\Psi_L(x) \to e^{i\omega^a(x)\tau^a} e^{i\beta(x)\frac{Y}{2}} \Psi_L(x)$ and $\Psi_R(x) \to e^{i\beta(x)\frac{Y}{2}} \Psi_R(x)$.

2.7.2 Electroweak symmetry breaking

Gauge invariance forbids us from adding explicit mass terms for the vector boson fields in Eq. (2.33) [53–55]. Since the weak vector bosons $W^\pm$ and Z are observed experimentally to be massive, a different method is required to introduce mass terms for these fields. This can be achieved by spontaneous symmetry breaking, using the Higgs mechanism [56–59].

We introduce a scalar field $\Phi(x)$ by adding to the Lagrangian the terms

$$\mathcal{L}_\phi [W, B, \Phi] = (D_\mu \Phi(x))^\dagger (D^\mu \Phi(x)) + \mu^2 \Phi^\dagger(x)\Phi(x) - \lambda \left(\Phi^\dagger(x)\Phi(x)\right)^2 , \tag{2.36}$$

where μ and λ are positive real constants. $\Phi(x)$ is an SU(2) doublet of complex scalar fields

$$\Phi = \frac{1}{\sqrt{2}} \begin{pmatrix} \phi_1 + i\phi_2 \\ \phi_3 + i\phi_4 \end{pmatrix} , \tag{2.37}$$

where ϕ_i are real scalar fields. $\Phi(x)$ transforms in the same way as a left-handed fermion under a gauge transformation: $\Phi(x) \to e^{i\omega^a(x)\tau^a} e^{i\beta(x)\frac{Y}{2}} \Phi(x)$. We can use gauge transformations to eliminate the fields $\phi_{1,2,4}$, leaving

$$\Phi(x) = \frac{1}{\sqrt{2}} \begin{pmatrix} 0 \\ \phi(x) \end{pmatrix} , \tag{2.38}$$

where $\phi(x)$ is a real scalar field.

The scalar Lagrangian $\mathcal{L}_\phi$ is invariant under $\mathrm{SU}(2)_L \times \mathrm{U}(1)_Y$ transformations. However, the potential $-\mu^2 \Phi^\dagger\Phi + \lambda \left(\Phi^\dagger\Phi\right)^2$ has a minimum at $\Phi^\dagger\Phi = \frac{\mu^2}{\lambda} = \frac{v^2}{2}$. The scalar field therefore has a non-zero vacuum expectation value

$$\langle\Phi\rangle = \frac{1}{\sqrt{2}} \begin{pmatrix} 0 \\ v \end{pmatrix} . \tag{2.39}$$

Rewriting Eq. (2.36) in terms of the fields

$$W^\pm_\mu(x) = \frac{1}{\sqrt{2}} \left(W^1_\mu(x) \mp i W^2_\mu(x)\right) , \tag{2.40}$$

$$Z_\mu(x) = \frac{1}{\sqrt{g^2 + g'^2}} \left(g W^3_\mu(x) - g' B_{mu}(x)\right) , \tag{2.41}$$

$$A_\mu(x) = \frac{1}{\sqrt{g^2 + g'^2}} \left(g W^3_\mu(x) + g' B_{mu}(x)\right) , \tag{2.42}$$

$$h(x) = \phi(x) - v , \tag{2.43}$$

the Lagrangian gains mass terms with masses

$$m_W = g\frac{v}{2}\,, \tag{2.44}$$

$$m_Z = \sqrt{g^2 + g'^2}\frac{v}{2}\,, \tag{2.45}$$

$$m_A = 0\,. \tag{2.46}$$

The spontaneous symmetry breaking gives mass to the $W^{\pm}$ and Z bosons. There is one massless boson remaining, corresponding to the unbroken $\mathrm{U}(1)_{EM}$ symmetry. This massless field $A_\mu(x)$ is the photon, and the remaining U(1) symmetry describes QED. The generator corresponding to A_μ is $Q = \tau^3 + Y$, which defines the conserved electromagnetic charge Q.

2.8 Ward identities

Having defined a Lagrangian which is symmetric under certain transformations of the fields, we can investigate the consequences of these symmetries. The identities which arise from symmetries of the Lagrangian are Ward identities [60, 61]; the quantum field theory equivalent of Noether's theorem [62], which relates symmetries of a Lagrangian to conservation laws in a classical field theory.

We start by generalising the path integral in Eq. (2.14) to a quantum field theory with fields $\phi_i(x)$:

$$\langle O\left[\phi\right]\rangle = \frac{1}{Z}\int \prod_i \mathcal{D}\phi_i O\left[\phi_i\right] e^{iS[\phi_i]}\,. \tag{2.47}$$

Consider a symmetry transformation of the fields $\phi \to \phi'$. If $\prod_i \mathcal{D}\phi_i e^{iS[\phi_i]}$ is invariant under this transformation, then

$$\begin{aligned}\langle O\left[\phi\right]\rangle &= \frac{1}{Z}\int \prod_i \mathcal{D}\phi_i' O\left[\phi_i'\right] e^{iS[\phi_i']} \\ &= \frac{1}{Z}\int \prod_i \mathcal{D}\phi_i O\left[\phi_i'\right] e^{iS[\phi_i]} \\ &= \langle O\left[\phi'\right]\rangle\ ,\end{aligned} \tag{2.48}$$

so the expectation value $\langle O\rangle$ is also invariant. Ward identities are derived from the condition $\delta\langle O\rangle = \langle O[\phi']\rangle - \langle O[\phi]\rangle = 0$.

It is possible that there are symmetries under which the action S is invariant but the integration measure $\prod_i \phi_i$ is not. This introduces an anomalous contribution to the Ward identity. An example is the axial anomaly, due to the non-invariance of the fermion integration measure under an axial vector rotation $\psi \to e^{i\alpha\gamma_5}\psi$, which leads to the non-conservation of the axial vector current $\bar{\psi}\gamma_\mu\gamma_5\psi$ [63–65].

Considering an infinitesimal transformation $\phi_i \to \phi_i + \delta\phi_i$, the infinitesimal changes to the operator O and action S are δO and δS, respectively. Assuming that the integration measure is invariant, so that there is no anomaly, we can calculate the terms in the path integral which are linear in infinitesimal quantities, finding

$$\delta \langle O \rangle = \langle \delta O \rangle + i \langle O \delta S \rangle = 0 \,. \tag{2.49}$$

As an example, consider the effect of an infinitesimal U(1) vector transformation $\psi(x) \to e^{i\varepsilon(x)}\psi(x) = (1+i\varepsilon(x))\psi(x)$ on the U(1) gauge-invariant action in Eq. (2.10). The Ward identity for the operator $O = 1$ is

$$i \langle \delta S \rangle = 0 \,. \tag{2.50}$$

The variation of the action under this transformation is

$$\delta S = -i \int d^4x \, \varepsilon(x) \partial_\mu \left(\bar{\psi}(x) \gamma^\mu \psi(x) \right) \,. \tag{2.51}$$

In order for the Ward identity $i \langle \delta S \rangle = 0$ to hold for arbitrary $\varepsilon(x)$, we require

$$\partial_\mu \left(\bar{\psi}(x) \gamma^\mu \psi(x) \right) = 0 \,, \tag{2.52}$$

so the vector current

$$j^\mu(x) = \bar{\psi}(x) \gamma^\mu \psi(x) \tag{2.53}$$

is conserved.

2.9 Chiral symmetry in QCD

As discussed in Sec. 2.2, the independence of left-handed and right-handed components in a theory of massless fermions leads to chiral symmetry, meaning that the action is invariant under global $\mathrm{U}(1)_V \times \mathrm{U}(1)_A$ transformations of the form $\psi \to e^{i\alpha_1} e^{i\alpha_2 \gamma_5} \psi$. In a theory with N_f flavours of massless fermions, the action is invariant under the larger symmetry group

$$\mathrm{U}\left(N_f\right)_L \times \mathrm{U}\left(N_f\right)_R = \mathrm{SU}\left(N_f\right)_L \times \mathrm{SU}\left(N_f\right)_R \times \mathrm{U}(1)_V \times \mathrm{U}(1)_A \,. \tag{2.54}$$

However, the $\mathrm{U}(1)_A$ symmetry is explicitly broken in the path integral by the axial anomaly [63–65], and the remaining flavour symmetry group is $\mathrm{SU}\left(N_f\right)_V \times \mathrm{SU}\left(N_f\right)_A \times \mathrm{U}(1)_V$.

We can introduce non-zero fermion masses, which explicitly break chiral symmetry. Defining the mass matrix $\mathcal{M} = \mathrm{diag}(m_1, \ldots, m_{N_f})$, and the fermion multiplet $\Psi = (\psi_1, \ldots, \psi_{N_f})$, the fermion action can be written as

$$\mathcal{L} = \bar{\Psi} \left(i \gamma^\mu D_\mu - \mathcal{M} \right) \Psi \,. \tag{2.55}$$

The Noether current associated to the $\mathrm{U}(1)_V$ symmetry is the vector current $\bar{\Psi}(x)\gamma_\mu\Psi(x)$, which is conserved even for non-zero, non-degenerate masses. The Noether currents for the $\mathrm{SU}(N_f)_V$ and $\mathrm{SU}(N_f)_A$ symmetries are

$$j_V^{\mu,a}(x) = \bar{\Psi}(x)\gamma^\mu T^a \Psi(x)\,, \tag{2.56}$$
$$j_A^{\mu,a}(x) = \bar{\Psi}(x)\gamma^\mu\gamma^5 T^a \Psi(x)\,, \tag{2.57}$$

where T^a are the generators of $\mathrm{SU}(N_f)$, and the Ward identities associated with these currents are

$$\partial_\mu j_V^{\mu,a} = \bar{\Psi}\left[\mathcal{M}, T^a\right]\Psi\,, \tag{2.58}$$
$$\partial_\mu j_A^{\mu,a} = \bar{\Psi}\left\{\mathcal{M}, T^a\right\}\gamma^5\Psi\,, \tag{2.59}$$

In the limit in which all flavours have the same mass, the commutator $[\mathcal{M}, T^a]$ is zero and $\mathrm{SU}(N_f)_V$ is an exact symmetry, called isospin symmetry [66, 67]. The $\mathrm{SU}(N_f)_A$ symmetry is only exact in the chiral limit, where $m_f = 0$ for all flavours f, and in the limit of degenerate quark masses the divergence of the current $j_A^{\mu,a}$ is proportional to the pseudoscalar density, $\partial_\mu j_A^{\mu,a} = 2m\bar{\Psi}T^a\gamma^5\Psi$ [68].

A consequence of the $\mathrm{SU}(N_f)_A$ symmetry is that for each state with positive parity there is a degenerate negative-parity state with the same isospin. In QCD, the three lightest quarks have masses $m_u, m_d, m_s \ll \Lambda_{\mathrm{QCD}}$, so the action has an approximate three-flavour chiral symmetry. Additionally, the strange quark mass m_s is an order of magnitude larger than the lightest quark masses m_u and m_d [10], so the QCD action could alternatively be considered to possess only a two-flavour approximate chiral symmetry. As a result, we would expect to find pairs of approximately mass-degenerate hadronic states with opposite parity. However, this phenomenon is not observed experimentally [49, 69].

This observation could be explained by spontaneous symmetry breaking, similar to the Higgs mechanism introduced in Sec. 2.7.2 to give mass to the weak bosons. If the scalar density has a non-zero vacuum expectation value $\langle\bar{u}u\rangle$, then the $\mathrm{SU}(N_f)_A$ symmetry is spontaneously broken in the QCD vacuum, and only the $\mathrm{SU}(N_f)_V \times \mathrm{U}(1)_V$ isospin and vector symmetries remain [70]. Although there is no analytical proof of this non-zero vacuum expectation value, it has been calculated using lattice QCD and found to be non-zero [17, 71–75]:

$$\Sigma^{1/3} = -\langle\bar{u}u\rangle^{1/3} = 272(5)\,\mathrm{MeV}\,. \tag{2.60}$$

Goldstone's theorem [53, 76] predicts the existence of $N_f^2 - 1$ massless bosons resulting from this spontaneous symmetry breaking. In the case $N_f = 2$, these are the three pions $\pi^\pm, \pi^0$. The pions are the lightest hadronic states, although their mass is non-zero due to the small explicit chiral symmetry breaking from the quark masses $m_u, m_d \neq 0$, and for this reason they are often referred to as "pseudo-Goldstone bosons". For $N_f = 3$, the eight pseudo-Goldstone bosons are the pseudoscalar octet, consisting of the pions along with the η meson and the kaons $K^\pm, K^0, \bar{K}^0$.

The approximate isospin symmetry $\mathrm{SU}(N_f)_V$ remains even after spontaneous symmetry breaking. Restricting to the case $N_f = 2$, the approximately degenerate u and d quarks can be grouped into a light-quark doublet ℓ with isospin $I = \frac{1}{2}$, where u and d are the eigenstates with $I_3 = \pm\frac{1}{2}$, respectively. The four pseudoscalar mesons $\bar{\ell}\ell$ form an $I = 1$ triplet of pions

$$\pi^+ = -\bar{d}u\,, \qquad \pi^0 = \frac{1}{\sqrt{2}}\left(\bar{u}u - \bar{d}d\right)\,, \qquad \pi^- = \bar{u}d\,, \tag{2.61}$$

and an $I = 0$ singlet

$$\eta = \frac{1}{\sqrt{2}}\left(\bar{u}u + \bar{d}d\right)\,. \tag{2.62}$$

This isospin symmetry is broken by the mass difference $m_d - m_u$, and by the different electromagnetic charges of the light quarks. The size of the mass isospin-breaking effect is $\mathcal{O}\left((m_d - m_u)/\Lambda_{\mathrm{QCD}}\right)$, and the size of the charge isospin-breaking effect is $\mathcal{O}(\alpha)$, where $\alpha \approx \frac{1}{137}$ is the fine-structure constant. Corrections from both of these isospin-breaking effects are therefore expected to be $\mathcal{O}(1\%)$ relative to isospin-symmetric quantities. The challenges involved in calculating isospin-breaking effects in lattice QCD will be discussed in Chapter 5.

Chapter 3

Lattice Quantum Chromodynamics

At low energies, perturbative calculations of QCD fail due to the strong coupling $\alpha_s \sim \mathcal{O}(1)$. A non-perturbative approach is required to make theoretical predictions for QCD processes. In this chapter we introduce lattice QCD, an ab initio method for non-perturbative calculation of QCD quantities. In this approach, QCD is formulated on a finite, discrete space-time lattice. This imposes ultraviolet and infrared cut-offs, regulating the theory in a non-perturbative manner, and is well-suited for numerical simulation. Extrapolation to the infinite-volume and continuum limits, in which the regulators are removed, allows numerically-calculated quantities to be compared with experimental results.

In this chapter I will outline a discretised formulation of QCD, and describe methods for numerical calculations of observables in this discretised theory. I will define the path integral on a space-time lattice in Sec. 3.1, and derive a discretised form of the QCD action in Sec. 3.2. In Sec. 3.3 the "fermion doubling" problem is discussed, and I define a discretised fermion action which does not suffer from this problem. I introduce an alternative fermion action, the domain wall fermions, in Sec. 3.4. Sec. 3.5 is an outline of the strategy used for numerical simulations of lattice QCD, and the chapter finishes in Sec. 3.6 with a method for calculating the ground-state energy from correlation functions computed on the lattice. More comprehensive reviews of lattice QCD can be found, for example, in textbooks including [77, 78].

3.1 Discretising the path integral

Lattice QCD calculations are carried out in Euclidean space-time (with metric $\delta_{\mu\nu}$) via Wick rotation $t \to i\,t$ [79]. After this Wick rotation, the path integral in Eq. (2.47) becomes [52, 80]

$$\langle O \rangle = \frac{1}{Z} \int \mathcal{D}\left[\Phi\right] O\left[\Phi\right] e^{-S[\Phi]}\,, \tag{3.1}$$

where Φ represents all relevant fields, which in QCD are fermion fields $\psi, \bar{\psi}$ and gluon fields A.

We wish to define this theory on a four-dimensional rectangular space-time lattice

$$\Lambda = \left\{ x = an = a\left(n_1, n_2, n_3, n_4\right),\, n_\mu = 0, 1, 2, \ldots, N_\mu - 1 \right\}\,, \tag{3.2}$$

where a is the distance between neighbouring lattice sites, or "lattice spacing", with mass dimension -1. The physical extent of the lattice in direction μ is $L_\mu = aN_\mu$. Commonly, the lattice extent is equal in the three spatial directions, and the notation $L_4 = T$, $L_i = L$, $i = 1, 2, 3$ is used.

In this discretised space-time, derivatives ∂_μ can be replaced by finite differences δ_μ, defined as

$$\delta_\mu f(x) = \frac{1}{a}\left(f(x + a\hat{\mu}) - f(x)\right), \tag{3.3}$$

$$\delta^*_\mu f(x) = \frac{1}{a}\left(f(x) - f(x - a\hat{\mu})\right), \tag{3.4}$$

where $\hat{\mu}$ is the unit vector in direction μ, and integrals become Riemann sums

$$\int d^4x\, f(x) \to a^4 \sum_{x\in\Lambda} f(x)\,. \tag{3.5}$$

The finite extent of the lattice requires that we impose boundary conditions. Periodic boundary conditions are often used, in which

$$f(x + r_\mu L_\mu) = f(x),\ r_\mu \in \mathbb{Z}\,. \tag{3.6}$$

The non-zero lattice spacing a restricts the accessible momentum modes p_μ to the Brillouin zone $-\frac{\pi}{a} \leq p_\mu < \frac{\pi}{a}$, and the finite extent L_μ quantises the momentum, so that the momenta are restricted to the set

$$\tilde{\Lambda} = \left\{ p_\mu = \frac{2\pi l_\mu}{aN_\mu},\ -\frac{N_\mu}{2} \leq l_\mu < \frac{N_\mu}{2},\ l_\mu \in \mathbb{Z} \right\}, \tag{3.7}$$

which defines a momentum lattice with extent $\frac{2\pi}{a}$ and lattice spacing $\frac{2\pi}{L_\mu}$. The space-time lattice therefore regulates the theory, with an ultraviolet cut-off provided by the inverse lattice spacing a^{-1} and an infrared cut-off provided by the finite size of the lattice L_μ^{-1}.

A discrete form of the Fourier transform $\mathcal{F}$ and its inverse $\mathcal{F}^{-1}$ can now be defined:

$$\left(\mathcal{F}f\right)(p) = a^4 \sum_{x\in\Lambda} f(x) e^{-ip\cdot x}\,, \tag{3.8}$$

$$\left(\mathcal{F}^{-1}\tilde{f}\right)(x) = \frac{1}{V}\sum_{p\in\tilde{\Lambda}} \tilde{f}(p)\, e^{ip\cdot x}\,, \tag{3.9}$$

where $V = \prod_\mu L_\mu$ is the volume of the lattice. We can derive a momentum representation of the finite second derivative $\delta^2 = \sum_\mu \delta_\mu \delta^*_\mu$:

$$\delta^2 = -\mathcal{F}^{-1}\hat{p}^2\mathcal{F}\,, \tag{3.10}$$

where we have introduced the lattice momentum

$$\hat{p}_\mu = \frac{2}{a} \sin\left(\frac{a p_\mu}{2}\right) , \tag{3.11}$$

and $\hat{p}^2 = \sum_\mu \hat{p}_\mu^2$.

On the lattice, with fields defined on the lattice sites $x \in \Lambda$, the integration measure in the path integral Eq. (3.1) becomes a product over all field configurations:

$$\mathcal{D}[\Phi] = \prod_{x \in \Lambda} \prod_a d\Phi_a(x) , \tag{3.12}$$

where the index a runs over all the fields which enter into the operator and action. The number of degrees of freedom has been rendered finite by the lattice formulation. In order to calculate expectation values from the discretised path integral, the action must be defined on the lattice Λ. The process of defining a discretised QCD action is addressed in Sec. 3.2.

3.2 Discretising the QCD action

The QCD action can be split into a fermion action $S_F[\psi, \bar{\psi}, A]$ and a gluon action $S_G[A]$. In Euclidean space, the QCD action takes the form

$$S_F[\psi, \bar{\psi}, A] = \int d^4x \sum_f \bar{\psi}_f \left(\gamma_\mu^E D_\mu + m\right) \psi_f , \tag{3.13}$$

$$S_G[A] = \frac{1}{2g^2} \int d^4x \, F^a_{\mu\nu}(x) F^a_{\mu\nu}(x) , \tag{3.14}$$

where the index f runs over quark flavours, g is the QCD coupling, and the Euclidean gamma matrices γ_μ^E are defined in terms of the Minkowski-space gamma matrices by

$$\gamma_i^E = -i\gamma_i, \; \gamma_4^E = \gamma_0, \; \gamma_5^E = \gamma_1^E \gamma_2^E \gamma_3^E \gamma_4^E . \tag{3.15}$$

In the remainder of this thesis we will drop the superscript E, and gamma matrices are assumed to take their Euclidean-space form.

Defining the fermion fields on the lattice sites, and replacing the derivative ∂_μ by the central difference $(\delta_\mu + \delta_\mu^*)/2$, the free fermion action for a single flavour can naïvely be written

$$S_F^{\text{free}}[\psi, \bar{\psi}] = \frac{a^4}{2} \sum_{x \in \Lambda} \sum_\mu \bar{\psi}(x) \left[\gamma_\mu \left(\delta_\mu + \delta_\mu^*\right) + m\right] \psi(x) . \tag{3.16}$$

This action is not invariant under an SU(3) gauge transformation

$$\begin{aligned} \psi(x) &\to \psi'(x) = \Omega(x)\psi(x) , \\ \bar{\psi}(x) &\to \bar{\psi}'(x) = \bar{\psi}(x)\Omega^\dagger(x) , \end{aligned} \tag{3.17}$$

since the discretised derivatives mix the fermion fields at neighbouring lattice sites, resulting in terms which transform as

$$\bar{\psi}(x)\psi(x+a\hat{\mu}) \to \bar{\psi}(x)\Omega^{\dagger}(x)\Omega(x+a\hat{\mu})\psi(x+a\hat{\mu})\,. \tag{3.18}$$

To define a gauge-invariant action, we can introduce a new variable $U_{\mu}(x)$ defined on the link between sites x and $x+a\hat{\mu}$, which transforms as

$$U_{\mu}(x) \to U_{\mu}^{'}(x) = \Omega(x)U_{\mu}(x)\Omega^{\dagger}(x+a\hat{\mu})\,. \tag{3.19}$$

These link variables are group elements of SU(3), and can be related to the gauge field $A_{\mu}(x)$ appearing in the continuum action by $U_{\mu}(x) = e^{iaA_{\mu}(x)}$. This definition of gauge links ensures that the quantity

$$\bar{\psi}(x)U_{\mu}(x)\psi(x+a\hat{\mu}) \tag{3.20}$$

is gauge invariant, and we can define a gauge-invariant fermion action

$$S_F\left[\psi,\bar{\psi},U\right] = \frac{a^4}{2}\sum_{x\in\Lambda}\sum_{f}\sum_{\mu}\bar{\psi}_f(x)\left[\gamma_{\mu}\left(\nabla_{\mu}+\nabla_{\mu}^{*}\right)+m\right]\psi_f(x)\,, \tag{3.21}$$

where we have introduced the lattice gauge-covariant derivatives [52]

$$\nabla_{\mu}\psi\left(x\right) = \frac{1}{a}\left(U_{\mu}\left(x\right)\psi\left(x+a\hat{\mu}\right)-\psi\left(x\right)\right)\,, \tag{3.22}$$

$$\nabla_{\mu}^{*}\psi\left(x\right) = \frac{1}{a}\left(\psi\left(x\right)-U_{\mu}^{\dagger}\left(x-a\hat{\mu}\right)\psi\left(x-a\hat{\mu}\right)\right)\,, \tag{3.23}$$

and $U_{\mu}^{\dagger}(x-a\hat{\mu}) = U_{-\mu}(x)$.

The next step is to define a discretised version of the gluon action in Eq. (3.14) in terms of the gauge links $U_{\mu}(x)$. The simplest gauge-invariant object which can be constructed on the lattice is the trace of the plaquette, which is the product of four gauge links around the smallest closed loop [52]:

$$U_{\mu\nu}\left(x\right) = U_{\mu}\left(x\right)U_{\nu}\left(x+a\hat{\mu}\right)U_{\mu}^{\dagger}\left(x+a\hat{\nu}\right)U_{\nu}^{\dagger}\left(x\right)\,. \tag{3.24}$$

The plaquette can be used to define the Wilson plaquette action [52]

$$S_G\left[U\right] = \frac{2}{g^2}\sum_{x\in\Lambda}\sum_{\mu<\nu}\mathrm{Re}\,\mathrm{tr}\left[\mathbb{1}-U_{\mu\nu}\left(x\right)\right]\,, \tag{3.25}$$

where g is the coupling strength of the fermion fields to the gauge field. Substituting $U_{\mu}(x) = e^{iaA_{\mu}(x)}$ and performing a Taylor expansion

$$A_{\nu}(x+a\hat{\mu}) = A_{\nu}(x)+a\partial_{\mu}A_{\nu}(x)+\mathcal{O}\left(a^2\right)\,, \tag{3.26}$$

it can be shown that

$$S_G\left[U\right] = \frac{a^4}{2g^2}\sum_{x\in\Lambda}\sum_{\mu,\nu}\mathrm{tr}\left[F_{\mu\nu}(x)F_{\mu\nu}(x)\right] + \mathcal{O}\left(a^2\right)\,, \tag{3.27}$$

and the Wilson plaquette action reduces to the continuum action in the limit $a \to 0$.

This gauge action can be modified by including additional terms to further suppress the $\mathcal{O}\left(a^2\right)$ discretisation errors. Improved gauge actions include the Lüscher-Weisz action [81–83] and the Iwasaki action [84–86].

3.3 Fermion doubling

There is a problem with the naïve fermion action in Eq. (3.21), which can be illustrated by considering the free theory, with $U_\mu(x) = \mathbb{1}$. Using a Fourier transform, the free fermion action in momentum space is

$$S_F\left[\psi,\bar{\psi}\right] = \sum_{p\in\tilde{\Lambda}}\bar{\psi}(p)\tilde{D}(p)\psi(p)\,, \tag{3.28}$$

with the momentum-space Dirac operator

$$\tilde{D}(p) = \frac{i}{a}\sum_\mu \gamma_\mu \sin(ap_\mu) + m\,. \tag{3.29}$$

Inverting the Dirac operator gives the free fermion propagator

$$\tilde{D}^{-1}(p) = \frac{-ia^{-1}\sum_\mu \gamma_\mu \sin(ap_\mu) + m}{a^{-2}\sum_\mu \sin^2(ap_\mu) + m^2}\,. \tag{3.30}$$

Physical particles correspond to the poles of this propagator. Considering the massless case as an example, the propagator has poles when $\sum_\mu \sin^2(ap_\mu) = 0$. In four dimensions there are 16 poles in the Brillouin zone, at momentum $p_\mu \in \{0, \frac{\pi}{a}\}$. The pole at $p = (0,0,0,0)$ is the physical quark and the other 15 poles are unphysical quarks which appear as a consequence of the discretisation. This phenomenon is known as fermion doubling.

The first solution to the fermion doubling problem was proposed by Wilson [52], by adding to the discretised Dirac operator a higher-dimensional term which disappears in the continuum limit. The modification proposed by Wilson is

$$\tilde{D}^{\text{Wilson}}(p) = \tilde{D}^{\text{naïve}}(p) + \frac{1}{a}\sum_\mu(1-\cos(ap_\mu))\,. \tag{3.31}$$

This additional term does not modify the physical pole at $p = 0$, but it contributes an additional mass term of $\frac{2}{a}$ for each momentum component $p_\mu = \frac{\pi}{a}$. The doublers therefore gain a mass at the order of the cut-off scale a^{-1}, and decouple from the theory in the limit $a \to 0$.

Transforming Eq. (3.31) back into position space, the Wilson fermion action is

$$S_F^{\text{Wilson}}\left[\psi,\bar{\psi}\right] = a^4 \sum_{x\in\Lambda} \bar{\psi}\left(x\right)\left(\gamma^\mu\left(\delta_\mu + \delta_\mu^*\right) + m\right)\psi(x) - \frac{a^5}{2}\sum_{x\in\Lambda}\bar{\psi}\left(x\right)\delta_\mu^*\delta_\mu\psi\left(x\right) . \tag{3.32}$$

As for the naïve fermion action, the Wilson action can be made gauge invariant by replacing the finite differences δ_μ and δ_μ^* by the lattice gauge-covariant derivatives defined in Eqs. (3.22) and (3.23).

3.4 Domain wall fermions

The condition for chiral symmetry, satisfied by the massless continuum Dirac operator, is

$$\{D,\gamma_5\} = D\gamma_5 + \gamma_5 D = 0\,. \tag{3.33}$$

The Wilson action in Eq. (3.32) does not satisfy this condition, even in the massless limit, so the Wilson term breaks chiral symmetry. One consequence of this is that the fermion mass gains an additive renormalisation proportional to a^{-1}. As a result, Wilson fermions with bare mass $m = 0$ are not massless, and the bare mass must be carefully tuned to reach the continuum limit [87].

It is desirable to find a lattice fermion action which is chirally symmetric and free from doublers. However, the Nielsen-Ninomiya theorem states that it is not possible to find a lattice Dirac operator in an even number of dimensions which is simultaneously local, doubler-free, satisfies Eq. (3.33) and has the correct continuum limit [88].

The Ginsparg-Wilson equation, derived using renormalisation group transformations, is an alternative condition for chiral symmetry on the lattice [89]:

$$\{D,\gamma_5\} = 2aD\gamma_5 D\,. \tag{3.34}$$

Domain wall fermions are a formulation of lattice fermions which approximately satisfies the Ginsparg-Wilson equation by introducing a fifth dimension, with left- and right-handed fermions separated in this extra dimension. This formulation was proposed in [90], and has been developed further in [91–96].

We first consider the continuum theory. Introducing a fifth dimension with coordinate s, and an s-dependent mass $M_5(s)$ with a discontinuity at $s = 0$

$$m\left(s\right) = \begin{cases} +M_5, & s > 0 \\ -M_5, & s < 0 \end{cases} , \tag{3.35}$$

we define a Dirac operator

$$D^{\text{DWF}} = \gamma_\mu\partial_\mu + \gamma_5\partial_s + m\left(s\right) , \tag{3.36}$$

which obeys the five-dimensional Dirac equation

$$\left[\gamma_\mu \partial_\mu + \gamma_5 \partial_s + m\left(s\right)\right] \Psi(x,\, s) = 0\,. \tag{3.37}$$

The chiral projection operators $P_\pm = (1 \pm \gamma_5)/2$ can be used to rewrite the five-dimensional spinor field $\Psi(x, s)$ in terms of the eigenstates $\psi_n(x)$ of the four dimensional Dirac equation

$$\left[\gamma_\mu \partial_\mu + m_n\right] \psi_n(x) = 0\,, \tag{3.38}$$

with eigenvalues m_n, as

$$\Psi(x, s) = \sum_n \left[a_n(s) P_+ + b_n(s) P_-\right] \psi_n(x)\,. \tag{3.39}$$

Substituting Eq. (3.39) into Eq. (3.37) gives

$$\left(\partial_s + M_5(s)\right) a_n(s) = m_n b_n(s)\,, \tag{3.40}$$

$$\left(-\partial_s + M_5(s)\right) b_n(s) = m_n a_n(s)\,. \tag{3.41}$$

For the ground state $m_0 = 0$, this has the solution

$$a_0(s) = N e^{-\int_0^s m(s')\, ds'} = N e^{-M_5 |s|}\,, \tag{3.42}$$

where N is a normalisation factor. The solution $b_0(s) = N e^{M_5 |s|}$ is not normalisable, and is therefore unphysical. The other solutions are an infinite tower of mass states $m_n \sim \mathcal{O}\left(M_5\right)$, which do not contribute significantly provided M_5 is sufficiently large. This action therefore produces a massless, right-handed chiral fermion which is exponentially localised at the discontinuity $s = 0$.

On the lattice, the fifth dimension cannot have an infinite extent. Restricting to a finite extent L_s, with periodic boundary conditions, requires that the mass term $m(s)$ must have two discontinuities, which can be fixed at $s = 0$ and $s = L_s/2$. In this case the left-handed solutions are also normalisable, resulting in a left-handed chiral mode localised at $s = L_s/2$. For finite L_s the left- and right-handed modes will mix, resulting in a small residual chiral symmetry breaking which disappears in the limit $L_s \to \infty$.

The domain wall fermion action can be coupled to four-dimensional gauge fields by replacing the partial derivatives in the four physical dimensions with covariant derivatives. The domain wall action used in Chapter 6 of this work is [94, 97]

$$S_F\left[\Psi,\bar{\Psi},U\right] = -\sum_{x,x'\in\Lambda}\sum_{s,s'=0}^{L_S-1}\bar{\Psi}(x,s)\left[\delta_{s,s'}D^{\parallel}(x,x') + \delta_{x,x'}D^{\perp}(s,s')\right]\Psi(x',s')\,, \tag{3.43}$$

$$D^{\parallel}(x,x') = \frac{1}{2}\sum_{\mu=1}^{4}\left[(1-\gamma_\mu)\,U_\mu(x)\delta_{x+a\hat{\mu},x'} + (1+\gamma_\mu)\,U_\mu^{\dagger}(x')\delta_{x-a\hat{\mu},x'} + (M_5-4)\,\delta_{x,x'}\right], \tag{3.44}$$

$$\begin{aligned} D^{\perp}(s,s') = {} & \frac{1}{2}\left[(1-\gamma_5)\,\delta_{s+1,s'} + (1+\gamma_5)\,\delta_{s-1,s'} - 2\delta_{s,s'}\right] \\ & - \frac{m_f}{2}\left[(1-\gamma_5)\,\delta_{s,L_s-1}\delta_{0,s'} + (1+\gamma_5)\,\delta_{s,0}\delta_{L_s-1,s'}\right]. \end{aligned} \tag{3.45}$$

As mentioned earlier for Wilson fermions, chiral symmetry breaking introduces an additive mass renormalisation. This residual mass m_{res} is a measure of the degree of chiral symmetry breaking, and domain wall fermions are approximately chiral provided m_{res} is small relative to the quark masses m_f. The residual mass is derived from the axial Ward identity [94]

$$\delta_\mu^* A_\mu(x) = 2m_f J_5(x) + 2J_{5q}(x)\,, \tag{3.46}$$

where $J_5(x) = P(x) = \bar{\psi}(x)\gamma_5\psi(x)$ is the pseudoscalar density, $A_\mu(x)$ is the conserved axial vector current and $J_{5q}(x)$ is a current defined at the midpoint of the fifth dimension,

$$J_{5q}(x) = \bar{\Psi}\left(x,\frac{L_s}{2}-1\right)P_+\Psi\left(x,\frac{L_s}{2}\right) - \bar{\Psi}\left(x,\frac{L_s}{2}\right)P_-\Psi\left(x,\frac{L_s}{2}-1\right), \tag{3.47}$$

which is sensitive to the residual chiral symmetry breaking. The final term in the expectation value

$$\left\langle\delta_\mu^* A_\mu(x)J_5(0)\right\rangle = 2\left\langle\left[m_f J_5(x) + J_{5q}(x)\right]J_5(0)\right\rangle \tag{3.48}$$

$$= 2\left\langle J_5(x)J_5(0)\right\rangle\left(m_f + \frac{\langle J_{5q}(x)J_5(0)\rangle}{\langle J_5(x)J_5(0)\rangle}\right) \tag{3.49}$$

is the residual mass, which can be calculated by fitting to the plateau region of the effective residual mass

$$m_{\text{res}}^{\text{eff}}(t) = \frac{\sum_{\mathbf{x}\in\mathbf{\Lambda}}\langle J_{5q}(\mathbf{x},t)J_5(0)\rangle}{\sum_{\mathbf{x}\in\mathbf{\Lambda}}\langle J_5(\mathbf{x},t)J_5(0)\rangle}\,. \tag{3.50}$$

3.5 Numerical lattice QCD simulations

3.5.1 Ensemble generation

The aim of lattice QCD calculations is to numerically compute expectation values from the discretised path integral

$$\langle O \rangle = \frac{1}{Z} \int \mathcal{D}\left[\psi, \bar{\psi}, U\right] O\left[\psi, \bar{\psi}, U\right] e^{-S_F\left[\psi,\bar{\psi},U\right]} e^{-S_G[U]}\,, \tag{3.51}$$

where the partition function is

$$Z = \int \mathcal{D}\left[\psi, \bar{\psi}, U\right] e^{-S_F\left[\psi,\bar{\psi},U\right]} e^{-S_G[U]}\,. \tag{3.52}$$

The fermion action has the bilinear form $S_F\left[\psi, \bar{\psi}, U\right] = \sum_f \int d^4x\, \bar{\psi}_f D_f\left[U\right] \psi_f$. The Grassman variables can be integrated out, so that the partition function becomes [98, 99]

$$Z = \int \mathcal{D}\left[U\right] \left(\prod_f \det D_f\left[U\right] \right) e^{-S_G[U]}\,. \tag{3.53}$$

On the lattice, the number of degrees of freedom in the path integral is finite, but still extremely large due to the large number of lattice sites. The computational cost of directly integrating over all degrees of freedom would be prohibitive, so an alternative approach is needed.

A Monte Carlo method can be used for this purpose: a random process can be used to sample field configurations from the probability distribution

$$P\left(U\right) \propto \left(\prod_f \det D_f\left[U\right] \right) e^{-S_G[U]}\,. \tag{3.54}$$

An ensemble of N_{conf} gauge field configurations is generated using a Markov chain process, which generates a configuration $U^{(i+1)}$ from a previous configuration $U^{(i)}$. In order for this process to sample gauge field configurations from the probability distribution $P\left(U\right)$, the probability $T(U^{(i+1)}|U^{(i)})$ of generating this new configuration must satisfy the detailed balance condition [100]

$$T\left(U^{(i+1)}|U^{(i)}\right) P\left(U^{(i)}\right) = T\left(U^{(i)}|U^{(i+1)}\right) P\left(U^{(i+1)}\right)\,. \tag{3.55}$$

One Markov chain Monte Carlo process which is often used to generate lattice gauge ensembles is the hybrid Monte Carlo (HMC) algorithm [101].

Since each configuration is generated from the preceding configuration, consecutive configurations will be correlated. It is therefore necessary to calculate expectation values on ensembles of configurations separated by a number of Monte Carlo steps, so that there is no correlation between configurations.

Once N_{conf} independent configurations have been sampled, the expectation value of an operator $O\left[U\right]$ can be estimated by evaluating $O^{(i)}\left[U^{(i)}\right]$ on each configuration, and taking the ensemble average:

$$\langle O\left[U\right] \rangle = \frac{1}{N_{\text{conf}}} \sum_{i=1}^{N_{\text{conf}}} O^{(i)}\left[U^{(i)}\right]\,. \tag{3.56}$$

By the central limit theorem, the statistical uncertainty in this estimate is $\mathcal{O}\left(1/\sqrt{N_{\text{conf}}}\right)$.

3.5.2 Quark propagators

When the operator O in Eq. (3.56) depends on the quark fields ψ and $\bar{\psi}$, this can be reformulated as a dependence on quark propagators through Wick contractions. Wick's theorem states that any n-point function of Grassman numbers $\eta_i, \bar{\eta}_j$ can be expressed as [102]:

$$\begin{aligned}\langle \eta_{i_1} \bar{\eta}_{j_1} \dots \eta_{i_n} \bar{\eta}_{j_n} \rangle &= \frac{1}{Z} \int \prod_{k=1}^{N} d\eta_k d\bar{\eta}_k \eta_{i_1} \bar{\eta}_{j_1} \dots \eta_{i_n} \bar{\eta}_{j_n} \exp\left(\sum_{m,n=1}^{N} \bar{\eta}_l M_{lm} \eta_m \right) \\ &= (-1)^n \sum_{P(1,\dots,n)} \operatorname{sign}(P) M^{-1}_{i_1 j_{P_1}} \dots M^{-1}_{i_n j_{P_n}} , \end{aligned} \tag{3.57}$$

where $P(1,\dots,n)$ are the permutations of the numbers $1,\dots,n$. For example, setting $M_{ij} = -D(i,j)$ in Eq. (3.57), the fermion 2-point correlator becomes

$$\left\langle \psi(x) \bar{\psi}(y) \right\rangle_{\psi,\bar{\psi}} = G(x,y) , \tag{3.58}$$

where the fermion propagator $G = D^{-1}$ is the inverse of the Dirac matrix

$$D(x,y)G(y,z) = \delta(x-z), \;\; x,y,z \in \Lambda , \tag{3.59}$$

and the angle brackets $\langle\rangle_{\psi,\bar{\psi}}$ denote the path integral over the fermion fields. The expectation value can then be rewritten

$$\left\langle O\left[\psi,\bar{\psi},U\right] \right\rangle_{\psi,\bar{\psi},U} = \left\langle O^{\text{Wick}}[U] \right\rangle_U , \tag{3.60}$$

where O^{Wick} is obtained from O by summing all possible pairwise contractions of quark fields $\psi_f, \bar{\psi}_f$.

Lattice calculations of correlation functions therefore require the computation of quark propagators. In principle, the propagator could be computed directly by inverting the Dirac matrix D. However, D is an extremely large matrix due to the large number of lattice sites, and a full inversion would therefore be too costly. Instead, one column of the propagator can be computed at a time, by solving

$$D(y,z)G(z,x_0) = \delta(y-x_0) \tag{3.61}$$

for a single source position x_0. This is a linear equation of the form

$$A\vec{x} = \vec{b} , \tag{3.62}$$

which must be solved for the vector $\vec{x}$. This is equivalent to finding $\vec{x}$ which minimises

$$\vec{x}A\vec{x} - \vec{x}\vec{b} . \tag{3.63}$$

This minimisation is typically done using variations of the conjugate gradient (CG) algorithm [103], an iterative process which approaches the minimum of this expression and stops when

$$\frac{\left\|A\vec{x}-\vec{b}\right\|}{\left\|\vec{b}\right\|} < \delta_{\text{res}} \tag{3.64}$$

for some small residual δ_{res}.

3.5.3 Stochastic $\mathbb{Z}_2$ noise sources

The condition in Eq. (3.61) assumes a point source, which is sensitive to spatial variations in the gauge fields. This inversion process is typically repeated for several source positions x_0 on each configuration, and the values of operators are averaged over these source positions. Since each propagator inversion is costly, it is interesting to consider sources which are distributed over the lattice volume, such as $\mathbb{Z}_2$ noise sources [104–106]. We can generate a set of stochastic sources $\eta(x)$, where each element is a $\mathbb{Z}_2 \times \mathbb{Z}_2$ complex number

$$\eta(x) \in \left\{ \frac{1}{\sqrt{2}} \left(\pm 1 \pm i\right) \right\} , \tag{3.65}$$

and invert the Dirac matrix using the condition

$$D(y,z)G(z,x) = \eta(x)\eta^{\dagger}(y) \, . \tag{3.66}$$

Averaging over N_{hit} noise sources $\eta_n(x)$,

$$\frac{1}{N_{\text{hit}}} \sum_{n=1}^{N_{\text{hit}}} \eta_n(x)\eta_n^{\dagger}(y) \xrightarrow{N_{\text{hit}}\to\infty} \delta(y-x) \, , \tag{3.67}$$

so the point source is reproduced in the large-N_{hit} limit.

These noise sources can be used to stochastically average over the entire lattice volume. Alternatively, $\mathbb{Z}_2$ wall sources can be used, in which $\eta(\mathbf{x}, t)$ are non-zero only for a single time-slice $t = t_0$, resulting in a stochastic average over the spatial sub-lattice. The use of $\mathbb{Z}_2$ wall sources has been seen to improve the statistical precision in calculations of quantities including meson masses, compared with calculations using point sources [106].

3.5.4 Physical limit

In order to compare the results of lattice calculations with experimental measurements, the lattice results must be extrapolated to the point where the lattice theory reduces to the physical continuum theory. This requires taking the infinite-volume limit $L_\mu \to \infty$, which removes the infrared cut-off, and the continuum limit $a \to 0$ which removes the ultraviolet cut-off. Additionally, if the lattice quark masses are larger than the physical masses of the quarks, the limit in which these masses take their physical values must be taken.

The effects of finite volume are expected to be proportional to e^{-mL} for a particle with mass m [107], and a lattice volume $m_\pi L \gtrsim 4$ is usually sufficient to ensure that finite volume effects are $\mathcal{O}(1\%)$ corrections [108]. This is not the case when electromagnetic effects are calculated on the lattice, and other methods are required to remove finite volume effects. This will be discussed further in Chapter 7.

The physical value of a on an ensemble is set by calculating a physical quantity, such as a meson mass, and fixing its value to be equal to that in the continuum. An additional physical input is required to fix each bare quark mass. The continuum limit $a \to 0$ is obtained by repeating this process on several gauge ensembles with different lattice spacings, and extrapolating lattice results by fitting an ansatz for the dependence on the lattice spacing a.

3.6 Calculating observables

3.6.1 Resampling

When the expectation value of an operator O is computed as the average over a set of field configurations, as in Eq. (3.56), the statistical error in this evaluation of the expectation value is straightforward to calculate via the standard deviation of the measurements $O^{(i)}$. However, the statistical error in the value of an observable computed as a combination of correlator expectation values is less straightforward to compute. A naïve propagation of errors, assuming all measurements are independent, is not valid and is liable to overestimate the error, because two values computed on the same configuration will typically be correlated.

A valid method for computing the statistical error in an observable is to evaluate the observable K times on different sets of N configurations, and calculate the standard deviation of these K values. This requires a method for generating K samples of N data from the existing sample of N_{conf} data. Two such methods are outlined below.

3.6.1.1 Jackknife

Given a dataset of size N_{conf}, the error in an observable θ computed on this dataset can be estimated as follows [109].

N_{conf} subsets of this dataset, each with size $N_{\text{conf}} - 1$, can be constructed by excluding the n^{th} entry of the dataset for each $n = 1, \ldots, N_{\text{conf}}$. The standard deviation of θ is defined as

$$\sigma_\theta \equiv \sqrt{\frac{N_{\text{conf}} - 1}{N_{\text{conf}}} \sum_{n=1}^{N_{\text{conf}}} \left(\theta_n - \hat{\theta}\right)^2}, \tag{3.68}$$

where $\hat{\theta}$ is the value of θ computed on the original dataset and θ_n is the value of θ computed on the subset with the n^{th} entry removed.

3.6.1.2 Bootstrap

New samples of size N_{conf} can be constructed from the original dataset by choosing N_{conf} entries at random, allowing for repetition. Using this process to generate K new samples, the standard deviation of an observable θ can be estimated as [110]

$$\sigma_\theta \equiv \sqrt{\frac{1}{K}\sum_{k=1}^{K}\left(\theta_k - \bar{\theta}\right)^2},\ \bar{\theta} \equiv \frac{1}{K}\sum_{k=1}^{K}\theta_k\,, \tag{3.69}$$

where θ_k is the value of θ computed on the k^{th} sample.

3.6.2 Extracting the ground-state energy

Often, the aim of a lattice calculation is to calculate the ground-state energy of the 2-point correlation function $\left\langle O\left(x\right)\bar{O}\left(0\right)\right\rangle$ of an operator O. For example, for a pseudoscalar meson O and $\bar{O}$ are the pseudoscalar annihilation and creation operators P and $\bar{P}$ respectively:

$$\begin{aligned} P\left(x\right) &= \bar{\psi}^{f_1}\left(x\right)\gamma_5\psi^{f_2}\left(x\right)\,, \\ \bar{P}\left(x\right) &= \bar{\psi}^{f_2}\left(x\right)\gamma_5\psi^{f_1}\left(x\right)\,, \end{aligned} \tag{3.70}$$

where f_1 and f_2 denote quark flavours. Projecting to a fixed spatial momentum defines a time-momentum correlator

$$C\left(t,\mathbf{p}\right) = a^3\sum_{\mathbf{x}\in\mathbf{\Lambda}}\left\langle O\left(\mathbf{x},t\right)\bar{O}\left(\mathbf{0},0\right)\right\rangle e^{-i\mathbf{p}\cdot\mathbf{x}}\,. \tag{3.71}$$

In the limit $T\to\infty$, a spectral decomposition of $C\left(t,\mathbf{p}\right)$ gives

$$\lim_{T\to\infty} C\left(t,\mathbf{p}\right) = \sum_k \left\langle 0\right| O\left|k\right\rangle\left\langle k\right|\bar{O}\left|0\right\rangle e^{-E_k(\mathbf{p})t}\,. \tag{3.72}$$

At sufficiently large times, ignoring the effects of periodic boundary conditions, the states with larger energy E_k will be exponentially suppressed and the correlator will be dominated by the ground state

$$C\left(t,\mathbf{p}\right) \sim A_0(\mathbf{p})e^{-E_0(\mathbf{p})t}\,, \tag{3.73}$$

where E_0 is the ground-state energy and A_0 is a constant. On a lattice with periodic boundary conditions, Eq. (3.73) gains an extra exponential term from propagation in the backward time direction:

$$\lim_{t\to\infty,t\ll T} C\left(t,\mathbf{p}\right) = A_0(\mathbf{p})\left(e^{-E_0(\mathbf{p})t} + e^{-E_0(\mathbf{p})(T-t)}\right) = A_0^{'}(\mathbf{p})\cosh\left(E_0(\mathbf{p})\left(t-\frac{T}{2}\right)\right)\,. \tag{3.74}$$

The ground-state energy can be extracted by minimising

$$\chi^2 = \sum_{t,t'=t_{\min}}^{t_{\max}} \left(C\left(t,\mathbf{p}\right) - f\left(t,\mathbf{p}\right)\right) \Sigma^{-1}\left(t,t'\right) \left(C\left(t',\mathbf{p}\right) - f\left(t',\mathbf{p}\right)\right), \tag{3.75}$$

$$f\left(t,\mathbf{p}\right) = A_0(\mathbf{p}) \cosh\left(E_0(\mathbf{p})\left(t - \frac{T}{2}\right)\right), \tag{3.76}$$

where $\Sigma\left(t,t'\right)$ is the covariance matrix of $C\left(t,\mathbf{p}\right)$, which can be estimated using the bootstrap resampling procedure:

$$\Sigma(t,t') = \frac{1}{K} \sum_{k=1}^{N_{\text{conf}}} \left(C^{(k)}\left(t,\mathbf{p}\right) - \left\langle C\left(t,\mathbf{p}\right)\right\rangle\right) \left(C^{(k)}\left(t',\mathbf{p}\right) - \left\langle C\left(t',\mathbf{p}\right)\right\rangle\right). \tag{3.77}$$

If there is strong correlation between the values of $C\left(t,\mathbf{p}\right)$ at different times t, the covariance matrix may be ill-conditioned, meaning that it cannot reliably be inverted. In this situation, the correlated fit in Eq. (3.75) can be reduced to an uncorrelated fit by setting off-diagonal elements of the covariance matrix to zero. The inverse covariance matrix becomes

$$\Sigma^{-1}(t,t') = \frac{\delta(t,t')}{\sigma^2(t)}, \tag{3.78}$$

where $\sigma(t)$ is the standard deviation of $C(t)$.

The sum in Eq. (3.75) runs over the interval $[t_{\min}, t_{\max}]$ where $C\left(t\right)$ is dominated by the ground state. To determine this region, we can define an effective mass function $m_{\text{eff}}(t)$ by solving

$$\frac{C\left(t,\mathbf{p}\right)}{C\left(t+1,\mathbf{p}\right)} = \frac{\cosh\left(\left(t - T/2\right) m_{\text{eff}}\right)}{\cosh\left(\left(t+1 - T/2\right) m_{\text{eff}}\right)} \tag{3.79}$$

at each t. The effective mass has a plateau at $m_{\text{eff}} = E_0$ in the region where $C\left(t,\mathbf{p}\right)$ is dominated by the ground state, and the interval $[t_{\min}, t_{\max}]$ is determined from this plateau region.

Chapter 4

The muon anomalous magnetic moment

The Landé g-factor g_ℓ of a charged lepton ℓ is defined by

$$\vec{M} = g_\ell \frac{q}{2m_\ell} \vec{S}, \tag{4.1}$$

where $\vec{M}$ is the lepton magnetic moment, $\vec{S}$ is the lepton spin, m_ℓ is the lepton mass and q is the lepton charge. At tree level, the Dirac equation (Eq. (2.22)) predicts the value of the dimensionless magnetic moment to be $g_\ell = 2$, but loop corrections will give an extra contribution to this value, characterised by the anomalous magnetic moment:

$$a_\ell \equiv \frac{g_\ell - 2}{2}. \tag{4.2}$$

The magnetic moment of a lepton appears in the vertex function describing the interaction of a lepton with a photon, as shown in Fig. 4.1. At tree level this vertex function is simply $-iq\gamma^\nu$ [41], but loop corrections will give extra contributions. The overall vertex function can be expressed as $-iq\Gamma^\nu(p_1, p_2)$, where Lorentz invariance and the Ward-Takahashi identity $k_\mu \Gamma^\mu = 0$ [61] constrain the form of this vertex to be [111]

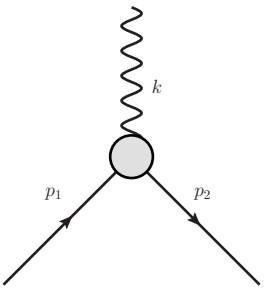

FIGURE 4.1: Muon interacting with a photon. The muon magnetic moment enters into the vertex function describing this diagram. The shaded circle represents all orders of loop corrections to this vertex.

$$\Gamma^{\nu}\left(p_1,p_2\right) = \gamma^{\nu} F_1\left(k^2\right) + \frac{i\sigma^{\nu\rho}k_{\rho}}{2m_{\ell}} F_2\left(k^2\right). \tag{4.3}$$

The two form factors F_1 and F_2 are functions of the square of the photon momentum $k = p_2 - p_1$, and $\sigma^{\nu\rho} = \frac{i}{2}\left[\gamma^{\nu},\gamma^{\rho}\right]$. In the $k^2 \to 0$ limit, the vertex renormalisation condition $\Gamma^{\mu}\left(k^2 = 0\right) = \gamma^{\mu}$ implies that $F_1\left(0\right) = 1$, and the combination $g_{\ell} = 2\left[F_1\left(0\right) + F_2\left(0\right)\right] = 2 + 2F_2\left(0\right)$ is equal to the dimensionless magnetic moment as defined in Eq. (4.1) [111]. From Eq. (4.2), the lepton anomalous magnetic moment can be expressed as $a_{\ell} = F_2\left(0\right)$, and is given by the loop corrections to the vertex in Fig. 4.1.

The electron anomalous magnetic moment has been calculated up to 5 loops in quantum electrodynamics (QED) using perturbation theory, and this result has been used to calculate the Standard Model prediction for the value of the fine structure constant, a value which agrees with experiment to a precision smaller than one part per billion [9, 10]. This offers an excellent test of the validity of QED.

All particles which couple to a lepton, either directly or indirectly, contribute to the value of its anomalous magnetic moment, giving this value a high sensitivity to any new physics beyond the Standard Model. The electron is too light to be particularly sensitive to new physics, so the muon anomalous magnetic moment a_{μ} offers a better candidate for observing the effects of new physics; the size of the contribution from new physics at energy scale M scales with m_{ℓ}^2/M^2, so the muon anomalous magnetic moment is more sensitive to the effects of new physics than that of the electron by a factor of $m_{\mu}^2/m_e^2 \approx 43000$. The tau is more sensitive still, but decays too quickly for the anomalous magnetic moment to be measured precisely [10]. Current experimental measurements of a_{μ} are sensitive to effects at mass scales up to $\mathcal{O}\left(\text{TeV}\right)$ [112].

Currently, the most precise measurement of a_{μ} is that from the E821 experiment at Brookhaven National Laboratory [113], and there is a discrepancy greater than three standard deviations between this result and the Standard Model prediction [10]. This long-standing theory-experiment discrepancy can be seen in Fig. 4.4. This discrepancy may be an indication of new physics, or there may be theoretical or experimental uncertainties which have not been fully taken into account.

A new experiment at Fermilab, which will improve the precision in the experimental measurement of the muon anomalous magnetic moment by a factor of four, has recently begun, and is expected to produce results in 2019 [14, 114]. An experiment at J-PARC, which will improve this precision still further, is currently under construction [15]. The proposed MUonE experiment will measure the leading hadronic contribution to a_{μ} through muon-electron scattering, and is aiming to start collecting data around 2022 [16]. It is therefore important that the precision of the Standard Model theoretical prediction of a_{μ} should also be improved, in order to investigate further the observed theory/experiment discrepancy. The leading source of uncertainty in the Standard Model prediction comes from hadronic contributions, which cannot be calculated analytically from first principles due to the non-perturbative nature of low-energy QCD, and the current best calculations of these hadronic contributions rely on model-based estimates or the use of dispersion relations along with experimental measurements of the cross-section $\sigma\left(e^+e^- \to \text{hadrons}\right)$ [115–117].

A first-principles calculation of these effects is desirable, and currently the only method for achieving this calculation is lattice QCD. Over the past years, several groups have begun to

compute the hadronic contribution to a_μ using lattice QCD [3, 118–135], and lattice calculations of the leading-order hadronic contribution are now approaching percent-level precision [123, 125, 131, 133, 134].

4.1 Experimental measurement of a_μ

The technique used to measure the muon anomalous magnetic moment experimentally involves measurement of muon spin precession in a magnetic field. As seen from Eq. (4.1), the muon has a magnetic moment which is aligned with its spin. Applying an external magnetic field exerts a torque on this magnetic moment, causing the muon spin to precess with frequency

$$\vec{\omega}_S = -g_\mu \frac{e\vec{B}}{2m_\mu} - \frac{e\vec{B}}{\gamma m_\mu}(1-\gamma), \tag{4.4}$$

where $\vec{B}$ is the external magnetic field and $\gamma = \left(1 - v^2/c^2\right)^{-\frac{1}{2}}$. The spin direction is measured by detecting electrons emitted when the muon decays; electrons are preferentially emitted in the direction opposite to the muon spin. This measurement allows the determination of $\vec{\omega}_S$, and hence g_μ [136].

The first measurement of g_μ began in 1957 at the Columbia-Nevis Cyclotron. This experiment was the first observation of muon spin precession in a magnetic field, and found the result $g_\mu = 2(1.00113^{+0.00016}_{-0.00012})$. This result was consistent with the value for the electron, showing that the muon behaves like a heavy electron [137].

In 1961, the first of three experiments at CERN measured the muon anomalous magnetic moment. At the CERN synchrocyclotron, polarised muons were injected into a 6-metre long magnet. The spin precession relative to the muon's momentum was measured, and a_μ computed through

$$\vec{\omega}_a = \vec{\omega}_S - \vec{\omega}_C = -a_\mu \frac{e\vec{B}}{m_\mu}, \tag{4.5}$$

where $\vec{\omega}_C$ is the cyclotron frequency. This experiment found the result $a_\mu = 0.001145(22)$, an error of 1.9%, allowing for the first observation of the effects of the α^2 term in the QED expansion of a_μ [138].

A second experiment at CERN measured the value of a_μ in 1968. This experiment used polarised muons which were produced via pion decay in a storage ring. The result was $a_\mu = 0.00116616(31)$, a precision of 265 parts per million, which probed the QED contribution at the three-loop level [139].

The final CERN experiment to measure a_μ began in 1975. The second CERN muon experiment was improved through the use of an injected pion beam, increasing the polarisation of the muon beam from 26% to 95%, and a more uniform magnetic field [136]. The result from this experiment was $a_\mu = 0.001165911(11)$, the precision of 7.3 ppm making this the first measurement of a_μ with sensitivity to hadronic effects [140].

The most recent measurement of a_μ comes from the E821 experiment at Brookhaven National Laboratory (BNL), which began in 1999. This experiment was modelled on the third CERN

muon experiment, but with precision improved to 0.54 ppm [141]. The final result announced from this experiment was

$$a_\mu = 116592091(54)(33) \times 10^{-11}, \tag{4.6}$$

where the first error is statistical and the second systematic [10, 113].

A new experiment, E989 at Fermilab, has recently begun collecting data for a new measurement of a_μ, and is expected to produce its first results in 2019. This experiment re-uses the 14 m muon storage ring from experiment E821, and a more intense muon beam will improve on the precision of experiment E821 by a factor of four, to 0.14 ppm [14, 114].

A further experiment, E34, is in development at J-PARC. This experiment will use an ultra-cold muon beam and a 66 cm storage ring. The smaller size of this storage ring compared to those used in previous experiments would allow for a more uniform magnetic field, offering a predicted precision of 0.1 ppm. The experiment is currently under construction, with the first muon beam expected in 2019 [15]

Another experiment, MUonE, has been proposed to measure the leading hadronic contribution to a_μ through muon-electron scattering. This experiment is aiming to achieve a precision of $\sim 0.3\%$ with two years of data, and data collection is predicted to begin around 2022 [16].

4.2 Standard Model prediction for a_μ

Currently, the most precise Standard Model prediction of the muon anomalous magnetic moment is

$$a_\mu = 116591823(1)(34)(26) \times 10^{-11}, \tag{4.7}$$

where the errors come from the electroweak, leading-order hadronic and higher-order hadronic contributions respectively [10]. The precision of this prediction is approximately equal to the precision of the most precise experimental measurement so far (see Eq. (4.6)).

The largest contribution to a_μ comes purely from QED. For the pure QED contribution, the 5-loop perturbative calculation of the electron anomalous magnetic moment can be used. This contribution is known with great precision: $a_\mu^{\text{QED}} = 116584718.95(0.08) \times 10^{-11}$ [9].

At one-loop level, the electroweak diagrams which contribute to a_μ are shown in Fig. 4.2. The electroweak contribution has been calculated up to two loops in perturbation theory, finding the result $a_\mu^{EW} = 153.6(1.0) \times 10^{-11}$ [142, 143].

The largest source of uncertainty in the Standard Model prediction of a_μ stems from hadronic contributions. The leading-order (LO) hadronic effects enter at $\mathcal{O}(\alpha^2)$ through the hadronic vacuum polarisation (HVP), and next-to-leading-order (NLO) contributions include hadronic light-by-light (HLbL) scattering. These contributions are shown in Fig. 4.3. Unlike the QED and electroweak contributions, these hadronic effects cannot be calculated using perturbation theory because at low energies the QCD coupling is too large to permit a perturbative expansion.

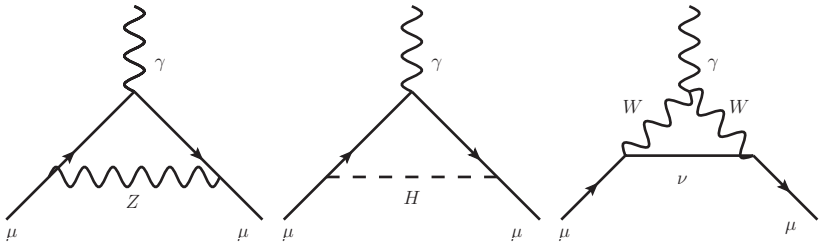

FIGURE 4.2: Feynman diagrams for the one-loop electroweak contributions to a_μ.

Contribution	$a_\mu \times 10^{11}$	Uncertainty
QED [9]	116 584 718.95	0.08
Electroweak [142, 143]	153.6	1.0
HVP,LO [115]	6931	34
HVP,NLO [145]	−98.7	0.9
HVP,NNLO [145]	12.4	0.1
HLbL [150]	105	26
Total [10]	116 591 823	43

TABLE 4.1: Contributions to the Standard Model prediction of a_μ.

The LO HVP contribution to a_μ is typically calculated using dispersion relations. This contribution is given by [1]

$$a_\mu^{\mathrm{HVP,LO}} = \frac{1}{3}\left(\frac{\alpha}{\pi}\right)^2 \int_{4m_\pi^2}^{\infty} ds \frac{R(s)K(s)}{s}\,, \tag{4.8}$$

where α is the fine structure constant, $R(s)$ is the ratio of the cross-section for the process $e^+e^- \to$ hadrons to the tree-level $e^+e^- \to \mu^+\mu^-$ cross-section in the limit $s \gg m_\mu^2$:

$$R(s) = \frac{\sigma\left(e^+e^- \to \text{hadrons}\right)}{\sigma_0\left(e^+e^- \to \mu^+\mu^-\right)} = \frac{\sigma\left(e^+e^- \to \text{hadrons}\right)}{\left(\frac{4\pi\alpha^2}{3s}\right)}\,, \tag{4.9}$$

and $K(s)$ is a QED kernel

$$K(s) = \frac{x^2}{2}(2-x^2) + \frac{(1+x^2)(1+x)^2}{x^2}\left(\ln(1+x) - x + \frac{x^2}{2}\right) + \frac{(1+x)}{(1-x)}x^2\ln(x)\,. \tag{4.10}$$

At high energy, the ratio $R(s)$ can be calculated from perturbative QCD, but at lower energies where QCD is non-perturbative the calculation relies on experimental data for $R(s)$. Higher-order HVP contributions to a_μ can also be calculated using the same experimental cross-section data, with different kernels $K(s)$ [144]. For the LO HVP contribution, this calculation gives $a_\mu^{\mathrm{HVP,LO}} = 6931(33)(7)\times10^{-11}$, where the first error is a predominantly systematic experimental uncertainty, and the second error originates from the use of perturbative QCD at high energy [115]. The NLO and NNLO HVP contributions from dispersion relations are $a_\mu^{\mathrm{HVP,NLO}} = -98.7(0.9)\times10^{-11}$ and $a_\mu^{\mathrm{HVP,NNLO}} = 12.4(0.1)\times10^{-11}$ [145]. The HLbL contribution, which is also a NLO hadronic contribution, is typically estimated from models derived from QCD at large N_c [146–151]. One such estimate of the HLbL contribution is $a_\mu^{\mathrm{HLbL}} = 105(26)\times10^{-11}$ [150].

The contributions to the Standard Model prediction of a_μ, along with their respective errors, are summarised in Table 4.1. It can be seen that the error is dominated by hadronic effects.

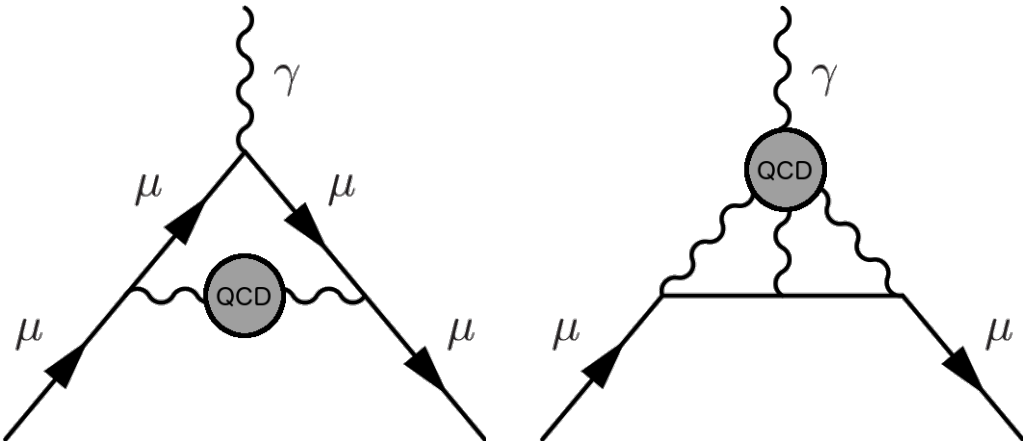

FIGURE 4.3: Hadronic vacuum polarisation (HVP, left) and hadronic light-by-light scattering (HLbL, right) contributions to the muon anomalous magnetic moment.

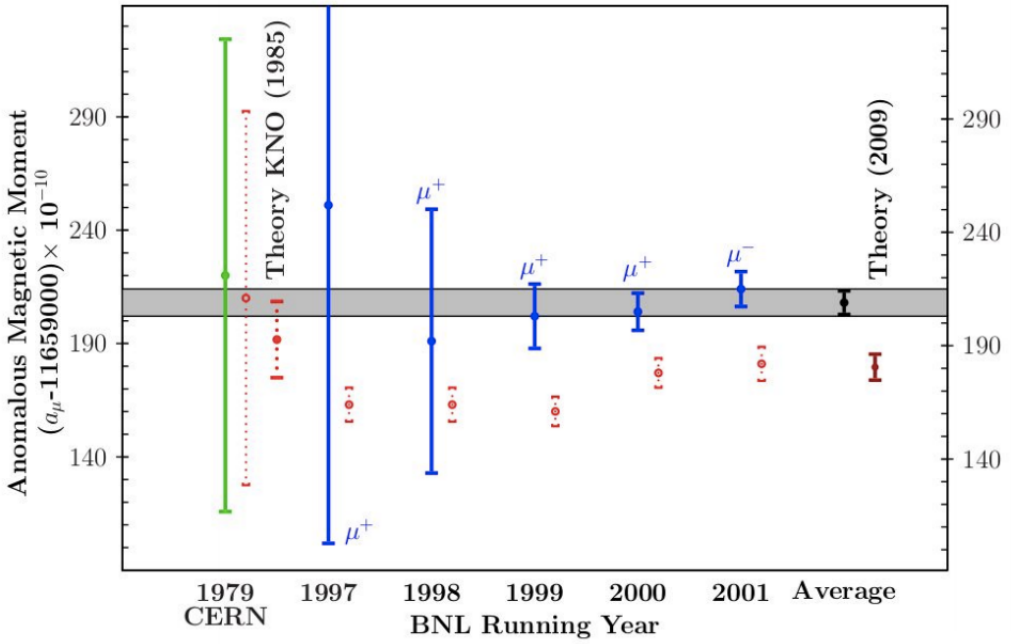

FIGURE 4.4: Comparison of experimental measurements of a_μ with Standard Model predictions over the period 1979-2009 [1].

The difference between the experimental measurement of a_μ in Eq. (4.6) and the Standard Model prediction in Eq. (4.7) is

$$\Delta a_\mu = a_\mu^{\text{exp}} - a_\mu^{\text{SM}} = 268(63)(43) \times 10^{-11}, \tag{4.11}$$

This is a discrepancy of 3.5 standard deviations. Fig. 4.4 compares experimental measurements of a_μ with Standard Model predictions over the period 1979-2009, showing that the theory/experiment discrepancy in a_μ has persisted over many years.

This discrepancy may be an indication of new physics beyond the Standard Model. One possible candidate for an explanation of this discrepancy comes from supersymmetry. Supersymmetric models predict a contribution to a_μ [112]

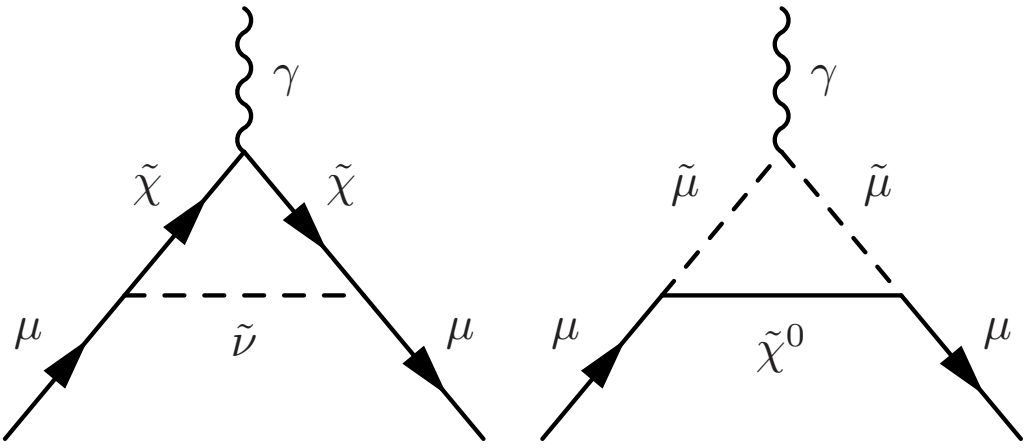

FIGURE 4.5: Two supersymmetric contributions to the muon anomalous magnetic moment. Left: chargino-sneutrino loop. Right: smuon-neutralino loop.

$$\left|a_\mu^{\mathrm{SUSY}}\right| \approx 130 \times 10^{-11} \left(\frac{100\,\mathrm{GeV}}{m_{\mathrm{SUSY}}}\right)^2 \tan\beta\,, \tag{4.12}$$

where $\tan\beta \sim 3 - 40$. The observed discrepancy Δa_μ could be explained by supersymmetric particles with mass $m_{\mathrm{SUSY}} \sim 100 - 500\,\mathrm{GeV}$. However, there have been no direct observations of such particles so far [10]. Fig. 4.5 shows two diagrams with supersymmetric contributions to the muon anomalous magnetic moment: a chargino-sneutrino loop and a smuon-neutralino loop.

However, this discrepancy could also be an indication that the theoretical or experimental errors are not fully under control. In particular, the experimental data used in the calculation of the HVP contribution may contain the effects of new physics beyond the Standard Model, and the model dependence of calculations of the HLbL contribution may introduce systematic errors which are not fully understood. To investigate this discrepancy further, it is important that the precision of the Standard Model prediction for a_μ^{had} should be improved, and a first-principles calculation is desirable so that systematic errors arising from the use of experimental and model-based input are avoided. The only method for computing these hadronic effects from first principles is lattice QCD.

4.3 Lattice calculation of the muon anomalous magnetic moment

4.3.1 Theory

The first step in a calculation of $a_\mu^{\mathrm{HVP.LO}}$ on the lattice is the calculation of the HVP tensor

$$\Pi_{\mu\nu}(Q) = \mathcal{F} C_{\mu\nu}(x)\,, \tag{4.13}$$

where $\mathcal{F}$ is the Fourier transform defined in Eq. (3.8), and $C_{\mu\nu}(x)$ is the electromagnetic current 2-point function

$$C_{\mu\nu}(x) = \langle J_\mu(x) J_\nu(0) \rangle \ . \tag{4.14}$$

In the continuum (in Euclidean space), the electromagnetic current is

$$J_\mu(x) = \sum_f q_f^2 \bar{\psi}_f(x) \gamma_\mu \psi_f(x) \,, \tag{4.15}$$

where the sum runs over quark flavours f and q_f is the electromagnetic charge of quark flavour f. The vector Ward identity $\langle J_\mu \delta S \rangle = \langle \delta J_\mu \rangle$ imposes the condition

$$\sum_\mu \partial_\mu C_{\mu\nu}(x) = 0 \,. \tag{4.16}$$

In momentum space this condition is $\sum_\mu Q_\mu \Pi_{\mu\nu}(Q) = 0$, which implies that the HVP tensor has a transverse structure

$$\Pi_{\mu\nu}(Q) = \left(\delta_{\mu\nu} Q^2 - Q_\mu Q_\nu\right) \Pi(Q^2) \,, \tag{4.17}$$

which defines the HVP form factor $\Pi(Q^2)$.

On the lattice, one can define a local vector current in analogy with the continuum electromagnetic vector current:

$$V^\ell_{\mu,f}(x) = \bar{\psi}_f(x) \gamma_\mu \psi_f(x) \,. \tag{4.18}$$

However, this vector current is not conserved and consequently a renormalisation constant Z_V is required to renormalise the local vector current. This local vector current reduces to the conserved vector current in the continuum, and therefore the renormalisation constant must have the behaviour $Z_V \to 0$ in the continuum limit. As in the continuum, a conserved vector current on the lattice can be derived from the Ward identity $\langle \delta S \rangle = 0$ under a U(1) vector transformation of the quark field ψ. This allows us to define a conserved vector current $V^c_\mu(x)$ which satisfies

$$\sum_\mu \delta^*_\mu V^c_\mu(x) = 0 \,, \tag{4.19}$$

and requires no renormalisation (i.e. $Z_{V^c} \equiv 0$). For the domain wall fermion action used for the study described in Chapter 6, the conserved vector current is [3]

$$V^c_\mu(x) = \sum_{s=0}^{N_s-1} \frac{1}{2} \left[\bar{\Psi}(x + a\hat{\mu}, s)(1 + \gamma_\mu) U^\dagger_\mu(x) \Psi(x, s) - \bar{\Psi}(x, s)(1 - \gamma_\mu) U_\mu(x) \Psi(x + a\hat{\mu}, s) \right] \ . \tag{4.20}$$

The vector Ward identity $\left\langle V^c_\mu \delta S \right\rangle = \left\langle \delta V^c_\mu \right\rangle$ imposes the condition

$$\sum_{\mu} \delta_{\mu}^{*} \left[\left\langle V_{\mu}^{c}(x) V_{\nu}^{c}(0) \right\rangle + \delta(x) \delta_{\mu\nu} \left\langle T_{\mu}(x) \right\rangle \right] = 0 \,. \tag{4.21}$$

This is similar to the continuum condition Eq. (4.16) if we define the correlation function $C_{\mu\nu}(x) = \sum_f q_f^2 \left[\left\langle V_{\mu,f}^{c}(x) V_{\nu,f}^{c}(0) \right\rangle + \delta(x) \delta_{\mu\nu} \left\langle T_{\mu,f}(x) \right\rangle \right]$. The second term here is a contact term which arises when the gauge links in the two non-local vector currents coincide. For the domain wall action used in this work, the tadpole operator T_μ is [3]

$$T_{\mu}(x) = \sum_{s=0}^{N_s-1} \frac{1}{2} \left[\bar{\Psi}(x + a\hat{\mu}, s)(1 + \gamma_{\mu}) U_{\mu}^{\dagger}(x) \Psi(x, s) + \bar{\Psi}(x, s)(1 - \gamma_{\mu}) U_{\mu}(x) \Psi(x + a\hat{\mu}, s) \right] . \tag{4.22}$$

This operator will become relevant when we consider QED corrections in Chapter 5.

Alternatively, following the methodology used in [128], the electromagnetic vector current 2-point function can be defined as

$$C_{\mu\nu}(x) = Z_V \sum_f q_f^2 \left\langle V_{\mu,f}^{c}(x) V_{\nu,f}^{\ell}(0) \right\rangle , \tag{4.23}$$

which again satisfies the Ward identity

$$\sum_{\mu} \delta_{\mu}^{*} C_{\mu\nu}(x) = 0 \,. \tag{4.24}$$

The HVP tensor is defined through a modification of Eq. (4.13):

$$\Pi_{\mu\nu}(Q) = \mathcal{F} C_{\mu\nu}(x) - a^4 \sum_{x \in \Lambda} C_{\mu\nu}(x) \,. \tag{4.25}$$

The second term on the right-hand side is the subtraction of the zero mode $\Pi_{\mu\nu}(0)$, which vanishes in the infinite-volume limit but is non-zero in finite volume [152, 153]. This zero-mode subtraction has been shown to improve the signal-to-noise ratio for $\Pi_{\mu\nu}(Q)$ at low Q^2 [128].

On the lattice, discretisation breaks rotational symmetry to hypercubic symmetry, and as a result the tensor decomposition of $\Pi_{\mu\nu}$ takes the form

$$\Pi_{\mu\nu}(Q) = \left(\delta_{\mu\nu} \hat{Q}^2 - \hat{Q}_{\mu} \hat{Q}_{\nu} \right) \Pi\left(Q^2\right) + \cdots , \tag{4.26}$$

where the ellipsis represents terms of the form $\sum_\mu Q_\mu^n$ for even n and $Q_\mu^m Q_\nu^n$ for odd m and n [152, 154], which are invariant under hypercubic symmetry transformations. These contributions can be removed exactly by only considering momenta with $Q_\mu = 0$ or $Q_\nu = 0$. Considering only momenta with vanishing spatial part, and taking $\mu = \nu = j$ with j running over spatial directions only, the HVP form factor can be calculated from the 2-point function $C_{\mu\nu}$ as

$$\Pi\left(Q^2\right) = \frac{1}{3} \sum_j \frac{\Pi_{jj}(Q)}{\hat{Q}^2} = \frac{1}{3} a^4 \sum_j \sum_{x \in \Lambda} C_{jj}(x) \left(\frac{e^{-iQt} - 1}{\hat{Q}^2} \right) . \tag{4.27}$$

The HVP form factor $\Pi(Q^2)$ is UV divergent, and can be renormalised through the subtraction

$$\hat{\Pi}\left(Q^2\right) = \Pi\left(Q^2\right) - \Pi\left(0\right) . \tag{4.28}$$

The zero mode $\Pi\left(0\right)$ cannot be evaluated directly by substituting $Q = 0$ into Eq. (4.27). Instead, the subtracted HVP can be determined using a modified kernel [153]:

$$\hat{\Pi}\left(Q^2\right) = \Pi\left(Q^2\right) - \Pi\left(0\right) = \frac{1}{3}a^4 \sum_j \sum_{x\in\Lambda} C_{jj}\left(x\right)\left(\frac{e^{-iQt}-1}{\hat{Q}^2} + \frac{t^2}{2}\right) . \tag{4.29}$$

Once the subtracted form factor $\hat{\Pi}(Q^2)$ has been calculated on the lattice, the leading-order hadronic contribution to the muon anomalous magnetic moment a_μ can be obtained through the integral [111]

$$a_\mu^{\mathrm{HVP,LO}} = 4\alpha^2 \int_0^\infty dQ^2 f\left(Q^2\right)\hat{\Pi}\left(Q^2\right) , \tag{4.30}$$

where the QED kernel $f\left(Q^2\right)$ is

$$f\left(Q^2\right) = \frac{m_\mu^2 Q^2 Z^3\left(1 - Q^2 Z\right)}{1 + m_\mu^2 Q^2 Z^2} , \; Z = -\frac{Q^2 - \sqrt{Q^4 + 4m_\mu^2 Q^2}}{2m_\mu^2 Q^2} . \tag{4.31}$$

The integral in Eq. (4.30) can be evaluated numerically using, for example, the trapezium rule. However, the kernel Eq. (4.31) has a peak close to $Q^2 \sim m_\mu^2/4$, and as a result the low-Q^2 region of $\hat{\Pi}(Q^2)$ gives a large contribution to $a_\mu^{\mathrm{HVP,LO}}$. This causes a problem for lattice calculations, as $a_\mu^{\mathrm{HVP,LO}}$ gains a large contribution from energies below the lattice infrared cut-off T^{-1} [128]. One solution is to use the process of "sine cardinal interpolation": instead of only computing the Fourier transform in Eq. (4.29) at discrete momenta $Q_t = 2\pi t/T$ where $at \in \mathbb{Z}, -\frac{T}{2} \leq t < \frac{T}{2}$, the Fourier transform can instead be computed for any $t \in \left[-\frac{T}{2}, \frac{T}{2}\right)$ [155]. This method allows access to the low-Q^2 region which gives a large contribution to $a_\mu^{\mathrm{HVP,LO}}$, and thereby reduces the size of cut-off effects. This interpolation of $\hat{\Pi}(Q^2)$ introduces finite-time effects, which are believed to decay exponentially with $m_\pi T$ [128, 156].

An alternative method for constructing $\Pi(Q^2)$ in the low-Q^2 region is the method of time moments [124]. Using the time moments

$$G_{2n} \equiv \int_{-\infty}^{\infty} dx_0\, x_0^{2n} G\left(x_0\right) , \tag{4.32}$$

the HVP form factor can be expanded as

$$\Pi\left(Q^2\right) = \Pi_0 + \sum_{j=1}^{\infty} \Pi_j Q^{2j} , \tag{4.33}$$

where

$$\Pi_j = (-1)^{j+1}\frac{G_{2j+2}}{(2j+2)!} . \tag{4.34}$$

Collaboration	Year	$a_\mu^{\mathrm{HVP,LO}} \times 10^{10}$
ETMC [123]	2014	674(21)(18)
HPQCD [125]	2017	667(6)(12)
CLS/Mainz [131]	2017	$654(32)(^{+21}_{-23})$
BMW [134]	2018	711.1(7.5)(17.4)
RBC/UKQCD [133]	2018	715.4(16.3)(9.2)

TABLE 4.2: Summary of lattice QCD calculations of $a_\mu^{\mathrm{HVP,LO}}$. In each case, the first error is statistical and the second is systematic.

The time moments method is not used in this work, but has been used in several other studies [157].

4.3.2 Summary of lattice QCD calculations of a_μ

Over the past few years, much work has been done in computing the HVP contribution to a_μ on the lattice [3, 118–135]. A summary of recent lattice QCD results is given in Table 4.2. In addition, a calculation by the RBC/UKQCD collaboration combines lattice data with experimental R-ratio data to find the result $a_\mu^{\mathrm{HVP,LO}} = 692.5(2.7) \times 10^{-10}$, which is currently the most precise determination of $a_\mu^{\mathrm{HVP,LO}}$ [133].

From Table 4.2 it can be seen that lattice calculations of $a_\mu^{\mathrm{HVP,LO}}$ are able to achieve precision of a few percent. In order for lattice calculations to compete with predictions from $e^+e^- \to$ hadrons, a precision better than 1% is required. At this level of precision, isospin-breaking effects are expected to be significant, so it is important that these effects are also computed. We have made the first calculation these isospin-breaking effects [3], in an exploratory study which laid the groundwork for the inclusion of isospin-breaking effects at the physical point in the RBC/UKQCD HVP calculation [133]. Several other lattice calculations of isospin-breaking corrections to $a_\mu^{\mathrm{HVP,LO}}$ have also been made [132, 134, 135, 158]. These effects are discussed in Chapter 5, and our exploratory calculation [3] is described in Chapter 6.

In addition to the HVP contribution to a_μ, it can be seen from Table 4.1 that an improved prediction is needed for the NLO hadronic contribution from HLbL scattering. Computing this contribution on the lattice is much more complex than the HVP calculation, due to the presence of a four-point correlation function of electromagnetic currents [159]. Nevertheless, lattice calculation of the HLbL contribution to a_μ is an active area of research [160–170].

Chapter 5

Isospin breaking

In nature, isospin symmetry is broken due to the different masses and electromagnetic charges of the up and down quarks: the masses of the quarks are $m_u = 2.2^{+0.5}_{-0.4}\,\text{MeV}$, $m_d = 4.7^{+0.5}_{-0.3}\text{MeV}$ in the $\overline{\text{MS}}$ scheme at 2 GeV [10] and their electromagnetic charges are $q_u = \frac{2}{3}e$, $q_d = -\frac{1}{3}e$. In the majority of lattice QCD simulations, however, the masses of the up and down quarks are set equal to each other; $m_u = m_d = m_l$. This choice reduces the computational cost of simulations, since the number of distinct flavours is reduced. In addition, electromagnetic effects are not included, with the quarks treated as charge-neutral particles. These simulations therefore respect isospin symmetry, since the up and down quarks are treated as identical particles.

This decision is justified by consideration of the scale of corrections introduced by breaking isospin symmetry. Electromagnetic corrections enter at $\mathcal{O}(\alpha)$, where $\alpha \approx 1/137$ is the fine structure constant. Corrections arising from the light quark mass difference enter at $\mathcal{O}\left((m_d - m_u)/\Lambda_{\text{QCD}}\right)$, where $m_d - m_u \approx 2.5\,\text{MeV}$ is the light quark mass difference and the QCD scale $\Lambda_{\text{QCD}} \approx 200\,\text{MeV}$. Both of these effects are therefore expected to be approximately two orders of magnitude smaller than the QCD effects. Until recently, the scale of isospin-breaking effects has been smaller than the resolution of lattice QCD calculations, so these effects could be safely neglected.

However, lattice QCD calculations of several quantities, including hadron masses and the ratio of kaon and pion decay constants, have now achieved precision of 1% or better [17], and others (including the HVP contribution to the muon anomalous magnetic moment, as discussed in Sec. 4.3.2) are now approaching percent-level precision. At this level it is expected that isospin-breaking effects become significant, so it is important to include these effects in lattice calculations.

In principle, isospin-breaking effects can be included in the quark sea by including QED terms in the action, along with non-degenerate light quark masses, when an ensemble of configurations is generated. However, the process of generating a new lattice ensemble is very computationally expensive, and it is therefore preferable to re-use existing ensembles where possible. A few recent studies have carried out fully dynamical simulations of lattice QCD+QED with non-degenerate light quark masses in the sea [20, 21, 171, 172], but the majority of studies of isospin-breaking effects make use of various techniques which allow the use of isospin-symmetric QCD ensembles.

A common method for including QED effects in lattice QCD simulations is to generate U(1) gauge configurations stochastically, and superimpose these onto isospin-symmetric QCD configurations before computing correlation functions [18]. Using this method, the fermion determinant

in the path integral is not modified, and therefore only valence quarks interact electromagnetically, while sea quarks remain charge-neutral. The theory is said to be "electro-quenched". At $\mathcal{O}(\alpha)$, the systematic uncertainty arising from this electro-quenching is suppressed by approximate flavour SU(3) symmetry, and is estimated to be $\sim 10\%$ of the QED correction [173]. At the present precision levels of lattice calculations, electro-quenching effects can generally be neglected. Generation of U(1) gauge configurations is computationally cheap, as will be discussed in Sec. 5.2, making this an efficient method for computing QED effects. This method has been used to compute meson and baryon mass splittings, displaying good agreement with experiment [2, 18, 173–175]. For the remainder of this report, this method will be referred to as the "stochastic method", and a more detailed description of the method is given in Sec. 5.2.

An alternative method for including isospin-breaking effects for valence quarks with an isospin-symmetric background is based on a perturbative expansion of the path integral in terms of the fine structure constant α, with the photon propagator inserted analytically [19]. This method has been demonstrated for the calculation of QED corrections to leptonic decay rates [176], meson masses [177] and HVP contribution to the muon $g-2$ [132, 178]. We refer to this method as the "perturbative method", and more details are given in Sec. 5.3.

It is possible to perform a lattice calculation in which sea quarks gain an electromagnetic charge, using an ensemble of isospin-symmetric configurations, by reweighting the configurations. This technique has been demonstrated in a few studies [22, 179, 180].

A further technical difficulty when including QED on the lattice is that, since electromagnetism is a long-range interaction due to the massless photon, the effects of finite volume are typically much larger for QED than for QCD. It is therefore important to correct for these finite-volume effects, and these corrections are the focus of Chapter 7 of this report. An alternative approach is to couple lattice QCD in a finite volume to photons in infinite volume, to suppress QED finite-volume effects. This approach has been applied to a lattice QCD calculation of the hadronic light-by-light contribution to the muon anomalous magnetic moment [164].

In [3], we made the first exploratory calculation of isospin-breaking corrections to the HVP. This calculation is described in Chapter 6. More recently, lattice calculations have been made of HVP isospin-breaking corrections in [132, 133, 135], corrections due to the light quark mass difference have been calculated in [158], and electromagnetic corrections to the HVP have been calculated from phenomenology [134].

In this project, I have applied the stochastic method to the calculation of QED corrections to meson masses and the HVP, and this has been compared with the same results obtained using the perturbative method. Our comparative study of these methods has been published in [3], and Chapter 6 is an account of this comparison. A discretised QED action is defined in Sec. 5.1, which is followed by a description of the stochastic method in Sec. 5.2, and of the perturbative method in Sec. 5.3. This chapter ends with a note on the calculation of isospin-breaking corrections arising from the different masses of the up and down quarks in Sec. 5.4.

5.1 Discretising the QED action

In the infinite-volume, continuum theory, the Feynman-gauge electromagnetic gauge action is

$$S_\gamma [A] = \frac{1}{4} \int d^4x \sum_{\mu,\nu} F_{\mu\nu}(x) F_{\mu\nu}(x) \,, \tag{5.1}$$

$$F_{\mu\nu}(x) = \partial_\mu A_\nu(x) - \partial_\nu A_\mu(x) \,. \tag{5.2}$$

where $A_\mu(x)$ is the electromagnetic vector potential. As discussed in Sec. 2.3.2, it is necessary to fix the gauge. Feynman gauge can be imposed by adding an extra term to the Lagrangian:

$$\begin{aligned} S_{\gamma,\text{Feyn.}}[A] &= \int d^4x \left\{ \frac{1}{4} \sum_{\mu,\nu} F_{\mu\nu}(x) F_{\mu\nu}(x) + \frac{1}{2} \left(\sum_\mu \partial_\mu A_\mu(x) \right)^2 \right\} \\ &= -\frac{1}{2} \int d^4x \sum_\mu A_\mu(x) \partial^2 A_\mu(x) \,. \end{aligned} \tag{5.3}$$

The photon propagator $D_{\mu\nu}(x-y) = \langle A_\mu(x) A_\nu(y) \rangle$ is related to the inverse of the Laplacian operator ∂^2:

$$D_{\mu\nu}(x-y) = -\delta_{\mu\nu} \left(\partial^2\right)^{-1} \delta(x-y) = \delta_{\mu\nu} \int \frac{d^4k}{(2\pi)^4} \frac{e^{ik\cdot(x-y)}}{k^2} \,. \tag{5.4}$$

On a finite lattice Λ, the Feynman-gauge electromagnetic gauge action could naively be defined as

$$\begin{aligned} S_{\gamma,\text{Feyn.}}[A] &= a^4 \sum_{x\in\Lambda} \left\{ \frac{1}{4} \sum_{\mu,\nu} F_{\mu\nu}(x) F_{\mu\nu}(x) + \frac{1}{2} \left(\sum_\mu \delta_\mu A_\mu(x) \right)^2 \right\} \\ &= -\frac{a^4}{2} \sum_{x\in\Lambda} \sum_\mu A_\mu(x) \delta^2 A_\mu(x) \,, \end{aligned} \tag{5.5}$$

where the electromagnetic vector potential $A_\mu(x)$ is defined on the link between lattice sites x and $x + a\hat{\mu}$, and δ_μ is the forward difference defined in Eq. (3.3). This gauge action is defined as a function of the non-compact gauge potential A_μ, in contrast to the Wilson plaquette action introduced in Eq. (3.25) which is defined in terms of the compact group-valued gauge field U_μ, which can be constructed here as $U_\mu(x) \equiv e^{iqaA_\mu(x)}$ for electromagnetic charge q. While the Wilson action could be used here, this would introduce unphysical photon self-interactions as cut-off effects.

As a function of the gauge potential in momentum space,

$$\tilde{A}_\mu(k) = [\mathcal{F} A_\mu(x)](k) = a^4 \sum_{x\in\Lambda} A_\mu(x) e^{-ik\cdot x}, \tag{5.6}$$

the action Eq. (5.5) is

$$S_{\gamma,\text{Feyn.}}\left[\tilde{A}\right] = \frac{1}{2V} \sum_{k\in\tilde{\Lambda}} \hat{k}^2 \sum_\mu \left| \tilde{A}_\mu(k) \right|^2 \,. \tag{5.7}$$

where $\hat{k}_\mu = \frac{2}{a}\sin\left(\frac{ak_\mu}{2}\right)$, $V \equiv \prod_\mu L_\mu$ is the volume of the lattice, and the momentum domain is

$$\tilde{\Lambda} = \left\{ \frac{2n_\mu \pi}{L_\mu},\ \mu = 0,1,2,3,\ n_\mu = -\frac{L_\mu}{2a}, \cdots, \frac{L_\mu}{2a} - 1 \right\}. \tag{5.8}$$

The photon propagator defined by this action is

$$D_{\mu\nu}(x-y) = \frac{\delta_{\mu\nu}}{V} \sum_{k \in \tilde{\Lambda}} \frac{e^{ik\cdot(x-y)}}{\hat{k}^2}\,, \tag{5.9}$$

which is not well-defined due to the divergent $k = 0$ term in the sum. This zero-momentum mode of the photon field is associated with a constant shift symmetry of the electromagnetic action Eq. (5.5),

$$A_\mu(x) \to A_\mu(x) + c_\mu\,, \tag{5.10}$$

which must be broken to avoid the unphysical divergence seen in Eq. (5.9).

The minimal scheme for breaking this shift symmetry is to subtract the zero-momentum mode of the photon field, by setting $\tilde{A}_\mu(k=0) = 0$. This scheme is typically named QED$_{TL}$, and has been used in several lattice calculations [18, 19, 173, 174]. However, the removal of the photon zero-mode results in a non-local theory, in which the photon field at position x couples to charged matter fields at all points in spacetime. As a result, charged particle propagators are divergent if the $T \to \infty$ limit is taken before the $L \to \infty$ limit [21].

QED$_{TL}$ is not the only choice to solve the zero-mode problem. One could subtract a larger subset of the modes of A_μ containing $\tilde{A}_\mu(k=0)$ without affecting the continuum limit, provided the subset reduces to one with measure zero in the continuum limit. An alternative choice, proposed in [23], is to remove the spatial zero-mode on every time slice:

$$\tilde{A}_\mu(k_0, \mathbf{0}) = 0\ \forall k_0\,. \tag{5.11}$$

This choice, usually known as QED$_L$, results in a theory which is still non-local in space, but is local in time, and as a result does not suffer from the problem stated above for QED$_{TL}$ [21]. This scheme has been used in a number of lattice QCD+QED studies [2, 21, 132, 133, 177, 181–183].

In the QED$_L$ scheme, the action Eq. (5.7) becomes

$$S_{\gamma,\text{Feyn.}}[A] = \frac{1}{2V} \sum_{k_0} {\sum_{\mathbf{k}}}' \hat{k}^2 \sum_\mu \left|\tilde{A}_\mu(k)\right|^2\,, \tag{5.12}$$

where the primed sum indicates that the zero-momentum mode is excluded from the sum.

Other approaches have been proposed to solve the zero-mode problem without violating locality. One such scheme is QED$_M$, in which the photon is given a small mass, and the physical limit is reached by extrapolating to zero photon mass [24]. Another alternative is QED$_C$, in which boundary conditions on the lattice are periodic up to charge conjugation [25, 184–188]. This approach allows the construction of charged states without requiring gauge fixing, although there

are additional effects which must be controlled as a result of the boundary conditions breaking charge conservation.

In this thesis, the QED_L scheme is chosen to solve the photon zero-mode problem. Chapter 7 is an investigation of finite-volume dependence in the QED_L theory.

5.2 Stochastic method

One method for calculating QED corrections is to generate $U(1)$ gauge configurations independently of $SU(3)$ gauge configurations, and calculate expectation values using the combined $U(1) \times SU(3)$ gauge fields, as proposed in [18]. A method for stochastically generating lattice $U(1)$ gauge configurations according to the action Eq. (5.12) is described in this section.

5.2.1 Generation of gauge configurations in momentum space

In order for the expectation value of a correlator to be equal to the average value of the correlator evaluated on a set of field configurations, as explained in Sec. 3.5, field configurations must be sampled from the probability distribution given by the Boltzmann weight:

$$p[A] \propto e^{-S_\gamma[A]} . \tag{5.13}$$

This sampling process is easiest in momentum space. As the action Eq. (5.12) is diagonal in both the momentum k and space-time index μ, all gauge field values $\tilde{A}_\mu(k)$ are independent Gaussian random variables. When generating a random set of gauge configurations according to the probability distribution in Eq. (5.13), each value of $\tilde{A}_\mu(k)$ must therefore be randomly chosen such that $\left|\tilde{A}_\mu(k)\right|$ is drawn from a Gaussian distribution with variance $2V/\hat{k}^2$, except for the zero-modes $\tilde{A}_\mu(k_0, \mathbf{0})$ which are set equal to 0 in the QED_L scheme. In addition, since the variance matrix is real, the real and imaginary parts of $\tilde{A}_\mu(k)$ do not mix and so each of $\text{Re}\left(\tilde{A}_\mu(k)\right)$ and $\text{Im}\left(\tilde{A}_\mu(k)\right)$ can be drawn directly from a Gaussian distribution with variance $V/\hat{k}^2$.

The Box-Muller procedure can be used to generate these Gaussian random numbers. This procedure generates pairs of numbers Z_1, Z_2, with a standard normal distribution (mean 0, variance 1), from pairs of random numbers U_1, U_2 which are uniformly distributed in the interval $(0, 1)$ [189]:

$$\begin{aligned} Z_1 &= \sqrt{-2\ln U_1}\cos(2\pi U_2) , \\ Z_2 &= \sqrt{-2\ln U_1}\sin(2\pi U_2) . \end{aligned} \tag{5.14}$$

In this study, the ranlux random number generator is used to generate the uniform random numbers. This generator is well-suited for lattice Monte Carlo simulations which require the generation of many random numbers, as it has an extremely long period [190].

In position space, $A_\mu(x)$ is a real-valued field. Therefore, only half of the modes $\tilde{A}_\mu(k)$ can be independent. Imposing this constraint when generating values of $\tilde{A}_\mu(k)$ involves communication

between lattice sites, which requires communication between compute nodes when computing on a distributed architecture. Instead, since the real and imaginary parts of $\tilde{A}_\mu(k)$ do not mix, it is equivalent to generate all modes independently in momentum space and set $\mathrm{Im}(A_\mu(x)) = 0$ after Fourier transforming into position space.

5.2.2 Transformation to Coulomb gauge

It is convenient to generate gauge configurations in Feynman gauge because the U(1) gauge action is trivially diagonal with respect to the space-time index. However, it is useful to make calculations also in a different gauge in order to check gauge invariance. It is possible to transform these Feynman-gauge configurations into Coulomb gauge using the transformation [21]

$$A_\mu \to A'_\mu = (P_C)_{\mu\nu} A_\nu \,, \tag{5.15}$$

where

$$(P_C)_{\mu\nu} = \delta_{\mu\nu} - e^{ia(k_\mu - k_\nu)/2} \frac{\hat{k}_\mu \left(0, \hat{\mathbf{k}}^*\right)_\nu}{\left|\hat{\mathbf{k}}\right|^2} \,. \tag{5.16}$$

5.2.3 Combining with SU(3) gauge fields

In order to compute observables in the QCD + quenched QED framework, it is necessary to combine the U(1) gauge field configurations generated according to this process with SU(3) gauge field configurations, to form U(3) gauge fields. This is achieved by multiplying each SU(3) gauge link with the corresponding U(1) gauge link:

$$U_\mu^{U(3)}(x) = U_\mu^{U(1)}(x) \cdot U_\mu^{SU(3)}(x) \,, \tag{5.17}$$

where $U_\mu^{\mathrm{U}(1)}(x)$ are U(1) group elements defined as

$$U_\mu^{U(1)}(x) = e^{iqaA_\mu(x)} \tag{5.18}$$

for electromagnetic charge q, and $U_\mu^{\mathrm{SU}(3)}(x)$ are SU(3) group elements. The position-space photon field $A_\mu(x)$ can be efficiently obtained from the photon field $\tilde{A}_\mu(k)$ generated in momentum space, using a Fast Fourier Transform (FFT).

5.2.4 Reducing statistical noise

Due to charge-conjugation symmetry, expectation values are invariant under the transformation $q \to -q$. However, charge conjugation invariance on the lattice is recovered only in the limit of infinitely many $U(1)$ gauge configurations, and the statistical noise therefore gains an $\mathcal{O}(q)$ contribution. In order to remove this $\mathcal{O}(q)$ noise, results can be computed twice on each configuration: first with $q = +q'$ and then with $q = -q'$. These two measurements are then averaged, so that the $\mathcal{O}(q)$ effects cancel exactly on each configuration.

5.3 Perturbative method

An alternative method for calculating QED effects was developed in [19], in which QED corrections are treated perturbatively. The QCD+QED path integral

$$\langle O \rangle = \frac{1}{Z} \int \mathcal{D}\left[\psi, \bar{\psi}, U, A\right] O\left[\psi, \bar{\psi}, U, A\right] e^{-S_F\left[\psi,\bar{\psi},U,A\right]} e^{-S_G[U]} e^{-S_\gamma[A]} \tag{5.19}$$

is expanded in powers of the electromagnetic charge q:

$$\langle O \rangle = \langle O \rangle_0 + \frac{q^2}{2} \frac{\partial^2}{\partial q^2} \langle O \rangle \Big|_{q=0} + \mathcal{O}\left(\alpha^2\right) , \tag{5.20}$$

where $\langle O \rangle_0$ is the expectation value without QED. The $\mathcal{O}(\alpha)$ contributions contain one photon propagator, with both ends coupled to quarks through the conserved vector current V_μ^c. Because the operator V_μ^c is non-local, as discussed in Sec. 4.3.1, a contact term arises when the gauge links in these two vector currents coincide. Consequently, the $\mathcal{O}(\alpha)$ term receives contributions with two insertions of the conserved vector current V_μ^c and contributions with one insertion of the tadpole operator T_μ [19]:

$$\langle O \rangle = \langle O \rangle_0 - \frac{q^2}{2} \sum_x \sum_\mu \langle O T_\mu(x) \rangle_0 D_{\mu\mu}(0) - \frac{q^2}{2} \sum_{x,y} \sum_{\mu,\nu} \left\langle O V_\mu^c(x) V_\nu^c(y) \right\rangle_0 D_{\mu\nu}(x-y) + \mathcal{O}\left(\alpha^2\right) . \tag{5.21}$$

For the domain wall action used in our study in Chapter 6, the operators V_μ^c and T_μ are defined in Eq. (4.20) and Eq. (4.21), respectively.

Using the QED$_L$ scheme, the photon propagator in Feynman gauge is

$$D_{\mu\nu}(x-y) = \frac{\delta_{\mu\nu}}{V} \sum_{k_0} {\sum_{\mathbf{k}}}' \frac{e^{ik\cdot(x-y)}}{\hat{k}^2} . \tag{5.22}$$

The sum over positions x and y of the photon vertices can be converted into a stochastic average by factorising the photon propagator into two parts, one which depends only on x and the other which depends only on y. In our study, two such factorisations are used.

For the "single-μ" insertion, the photon propagator is factorised as

$$D_{\mu\nu}(x-y) = \left\langle \sum_u D_{\mu\nu}(x-u)\, \eta(u)\, \eta^\dagger(y) \right\rangle_\eta \equiv \left\langle \tilde{D}_{\mu\nu}(x)\, \eta^\dagger(y) \right\rangle_\eta , \tag{5.23}$$

where the stochastic noise sources η are chosen such that

$$\left\langle \eta(x)\, \eta^\dagger(y) \right\rangle_\eta = \delta_{xy} . \tag{5.24}$$

Correlation functions are then constructed from sequential propagators with insertions of the operators $\sum_x V_\mu^c(x)\, \tilde{D}_{\mu\nu}(x)$, $\sum_x V_\mu^c(x)\, \eta^\dagger(x)$ and $\sum_x T_\mu(x)\, D_{\mu\mu}(0)$, where $D_{\mu\mu}(0)$ can be calculated exactly. The stochastic average is taken over QCD gauge configurations and stochastic sources η, and is then summed over the Lorentz indices μ, ν.

For the "summed-μ" insertion, different stochastic sources are used for each of the four Lorentz indices. The photon propagator factorisation is

$$D_{\mu\nu}(x-y) = \left\langle \sum_u \sum_\sigma D_{\mu\sigma}(x-u)\,\xi_\sigma(u)\,\xi_\nu^\dagger(y) \right\rangle_\xi \equiv \left\langle \hat{D}_\mu(x)\,\xi_\nu^\dagger(y) \right\rangle_\xi , \tag{5.25}$$

with stochastic sources which satisfy

$$\left\langle \xi_\mu(x)\,\xi_\nu^\dagger(y) \right\rangle_\xi = \delta_{xy}\delta_{\mu\nu} , \tag{5.26}$$

such as $\mathbb{Z}_2$ noise sources.

Using this method, the operators used for sequential insertions are $\sum_x \sum_\mu V_\mu^c(x)\,\hat{D}_\mu(x)$, $\sum_x \sum_\mu V_\mu^c(x)\,\xi_\mu^\dagger(x)$ and $\sum_x \sum_\mu T_\mu(x)\,D_{\mu\mu}(0)$. The sum over Lorentz indices is carried out within the insertion, so the number of sequential propagator inversions is reduced by a factor of 4 compared with the single-μ insertion method.

5.4 Strong isospin-breaking on the lattice

In addition to isospin-breaking effects from the electromagnetic interactions of quarks, isospin symmetry is also broken by the different masses of the up and down quarks. We refer to effects arising from this difference in masses as strong isospin-breaking effects. Such effects can be calculated on the lattice by choosing different input bare masses for the up and down quarks. As for the calculation of QED corrections, this can be done in a quenched setup by assigning different masses to the valence up and down quarks while keeping the masses of the sea quarks equal. This allows for the re-use of existing isospin-symmetric gauge ensembles.

When both strong and electromagnetic isospin-breaking corrections are included, the separation of these two effects will depend on the choice of renormalisation scheme. This is because the different charges of the up and down quark will result in different corrections to their masses. For a physical calculation of electromagnetic isospin-breaking corrections, the bare quark masses should be tuned so that the renormalised masses of the light quarks are equal. The strong isospin-breaking corrections can be calculated by changing the mass of either the up or down quark, while keeping the other mass fixed, to reproduce the physical mass difference $m_d - m_u$.

Chapter 6

Comparison of isospin-breaking methods

This chapter is an account of a comparative study of the stochastic and perturbative methods introduced in Chapter 5. This study has been published in [3].

As isospin-breaking effects become more important in lattice calculations, it is important to investigate efficient methods for calculating these effects. The aim of this study is to implement both the stochastic and the perturbative method, and make a comparison of results obtained from exploratory calculations using the two methods. In doing so, in addition to providing a valuable cross-check of the implementation of each method, the statistical precision achieved by both approaches can be compared. This comparison provides useful input when choosing a method for calculating QED corrections in more expensive calculations at the physical point.

QED and strong isospin-breaking corrections are calculated for meson masses, and for the HVP and its contribution to a_μ. This constitutes the first lattice calculation of isospin-breaking corrections to the HVP, although it must be noted that this is an exploratory calculation at larger-than-physical light quark masses, and no attempt is made to extrapolate the results to the physical point.

Sec. 6.1 contains a summary of the parameters used in our study. The calculation of isospin-breaking corrections to meson masses is described in Sec. 6.2, and for the HVP in Sec. 6.3. In Sec. 6.4, the precision of the two methods is compared at equal computational cost.

This work was a collaborative effort. I implemented the stochastic method and carried out the analysis of data obtained using this method, while the perturbative method was implemented and analysed by Vera Gülpers. I present results from both methods in this chapter, since the primary purpose of the study is the comparison of the two methods.

6.1 Parameters

For the comparison of isospin-breaking methods, we use a $24^3 \times 64$ domain wall fermion ensemble, with 2+1 sea quark flavours (mass-degenerate up/down, and strange), generated by the

RBC/UKQCD collaboration [191]. This isospin-symmetric ensemble has the following parameters [192]:

$$\begin{aligned} a^{-1} &= 1.78\,\text{GeV}, \\ am_{u,d} &= 0.005, \\ am_s &= 0.04, \\ m_\pi &= 341\,\text{MeV}. \end{aligned} \tag{6.1}$$

The masses $m_{u,d,s}$ are input parameters whose values are determined, along with the scale a^{-1}, by fixing a set of hadron masses in the isospin-symmetric situation. The isospin-symmetric pion mass on this ensemble is larger than the physical pion mass, so we do not calculate at physical light quark masses. For this exploratory study we are primarily interested in the relative performance of the two QED methods, and we therefore make no effort to extrapolate results to the physical point.

The mass of the valence up quark is chosen to be equal to that of the light sea quark: $am_u = 0.005$. The valence down quark is given a mass different from that of the up quark, to break strong isospin symmetry. The down quark mass is chosen to be $am_d = 0.005915$, so that converting the bare mass difference $am_d - am_u$ to $\overline{\text{MS}}$ using results from [193] reproduces the physical value of the light quark mass difference $m_d - m_u$ as calculated in [175]. The mass of the valence strange quark is set equal to the physical strange quark mass which, in these lattice units, is $am_s = 0.03224$.

To calculate with physical masses, the quark masses would need to be re-tuned in the presence of QED such that a selection of meson masses are fixed to their experimental values. In this study, the quark masses have not been retuned in the presence of QED. We therefore choose to define the QED correction to an observable as the difference between its value with QED effects and its value without QED, keeping the bare quark masses constant.

The quark electromagnetic charges are chosen to be equal to their physical values: $q_u = \frac{2}{3}e$, $q_d = q_s = -\frac{1}{3}e$, where $e = \sqrt{4\pi\alpha} = 0.302822$ is the positron charge.

Quark propagators are calculated for 87 QCD gauge configurations, with 16 complex $\mathbb{Z}_2$ wall sources per configuration [106]. One $U(1)$ gauge configuration is used per QCD gauge configuration for the stochastic method. For the perturbative method, one $\mathbb{Z}_2$ noise source is used per configuration and source position when the single-μ insertion is used, and four $\mathbb{Z}_2$ noise sources (one for each Lorentz index) per configuration and source position for the summed-μ insertion.

6.2 Meson masses

We begin the comparison of the stochastic and perturbative methods by calculating isospin-breaking corrections to meson masses. These effects have been calculated in several previous studies [2, 18, 19, 21, 171–175, 177]. However, our study is the first direct comparison of the stochastic and perturbative methods.

6.2.1 QED correction

The pion and kaon masses are extracted from the pseudoscalar two-point correlation function, following the procedure described in Sec. 3.6.2. For correlation functions obtained using the stochastic method, the QED correction to the effective mass can be determined by calculating the effective mass in Eq. (3.79) for the correlation function including QED, and also for the correlation function without QED, and taking the difference. We refer to this as the "cosh-mass" method:

$$\delta m_{\text{eff}}^{\cosh} = m_{\text{eff}}(t) - m_{\text{eff}}^{0}(t). \tag{6.2}$$

However, when correlation functions are obtained using the perturbative method, a different technique for extracting the QED mass correction is required because QED corrections are only included up to $\mathcal{O}(\alpha)$. Neglecting the effects of periodic boundary conditions, the correlation function including all orders of QED is

$$\lim_{t\to\infty, t\ll T} C(t) = Ae^{-mt} = (A_0 + \delta A)\, e^{-(m_0+\delta m)t}, \tag{6.3}$$

where subscript 0 denotes quantities in the case without QED. Expanding Eq. (6.3) up to $\mathcal{O}(\alpha)$ gives

$$\lim_{t\to\infty, t\ll T} C(t) = A_0 e^{-m_0 t}\left(1 + \frac{\delta A}{A_0} - \delta m\, t\right) = C_0(t)\left(1 + \frac{\delta A}{A_0} - \delta m\, t\right). \tag{6.4}$$

The QED mass correction can then be determined from the linear time dependence of the ratio $C(t)/C_0(t)$. We can define the QED correction to the effective mass from this ratio:

$$\delta m_{\text{eff}}^{\text{ratio}}(t) = \frac{C(t)}{C_0(t)} - \frac{C(t+1)}{C_0(t+1)}. \tag{6.5}$$

We refer to this as the "ratio" method, and it can be extended to account for the effect of periodic boundary conditions:

$$\delta m_{\text{eff}}^{\text{ratio}}(t) = \frac{\frac{C(t)}{C_0(t)} - \frac{C(t+1)}{C_0(t+1)}}{\left(\frac{T}{2} - t\right)\tanh\left(m_0\left(\frac{T}{2} - t\right)\right) - \left(\frac{T}{2} - (t+1)\right)\tanh\left(m_0\left(\frac{T}{2} - (t+1)\right)\right)}. \tag{6.6}$$

The left-hand plot in Fig. 6.1 shows the QED correction to the effective mass of the charged kaon, calculated using the cosh-mass method for the stochastic data and the ratio method for the perturbative data. The single-μ insertion was used for the perturbative data. The QED mass correction δm^{γ} can be extracted by fitting a constant to the region in which the effective mass forms a plateau.

The right-hand plot in Fig. 6.1 shows the correlated difference between the charged kaon effective mass from the stochastic and perturbative methods, from which we can see that there is a small systematic difference between the two datasets. The relative size of the discrepancy is approximately 1%, suggesting it is due to $\mathcal{O}(\alpha^2)$ effects, which are present in the stochastic data but not in the perturbative data. To check whether this is the case, we generated data

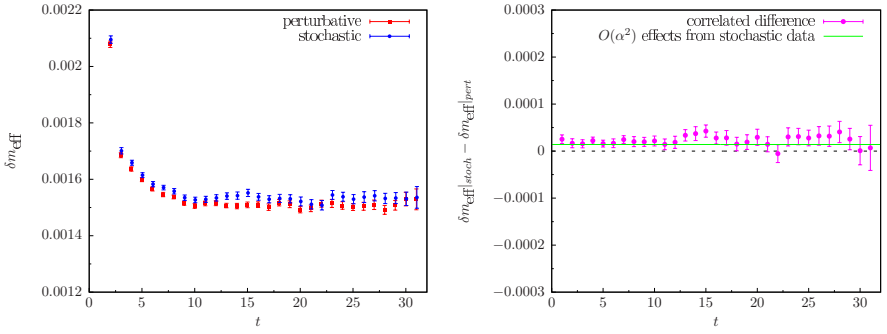

FIGURE 6.1: Left: QED effective mass correction for a charged kaon, from the stochastic method (blue circles) and perturbative method (red squares). Right: correlated difference of the results from the two methods. The green line shows the $\mathcal{O}\left(\alpha^2\right)$ effect in the stochastic data.

using the stochastic method with a larger electromagnetic coupling ($\alpha = 1/4\pi$). Calculating the QED mass correction from this data gives us three data points, at $\alpha = 0$, $\alpha = 1/137$ and $\alpha = 1/4\pi$, to which we fit the ansatz $\delta m = a\alpha + b\alpha^2$. The linear term, $a\alpha$, should then give the $\mathcal{O}\left(\alpha\right)$ correction which is calculated in the perturbative method, and the term $b\alpha^2$ should be the $\mathcal{O}\left(\alpha^2\right)$ contribution to the stochastic data, which is the difference between results from the two methods. This $\mathcal{O}\left(\alpha^2\right)$ contribution for the charged kaon mass is plotted as a green line on the right-hand plot of Fig. 6.1, and it can be seen that this contribution indeed accounts for the observed discrepancy between the two methods.

As explained in Sec. 5.2.4, the $\mathcal{O}\left(q\right)$ noise can be exactly cancelled in the stochastic method by averaging over results with charges $\pm q$. The effect of this averaging procedure on the charged kaon effective mass correction can be seen in Fig. 6.2, which shows the ratio of the statistical uncertainties after averaging over $\pm q$ to the statistical uncertainties before averaging. This ratio of errors is approximately equal to the charge $e = 0.302822$, indicating that the errors have been reduced from $\mathcal{O}\left(q\right)$ to $\mathcal{O}\left(q^2\right)$.

Our results for QED corrections to the masses of charged and neutral pions and kaons are quoted in Table 6.1, with statistical errors calculated using the bootstrap method. These values are converted to physical units using the lattice spacing quoted in Eq. (6.1), which has not been corrected to account for isospin-breaking effects. A full calculation of the neutral pion mass difference should also include the quark-disconnected contribution, which we do not calculate. The results from the two methods differ at the level of $\sim 1.5\sigma$, a discrepancy which can be attributed to the higher-order effects in α which are present in the stochastic data but not the perturbative data.

In a theory with chiral symmetry, the QED correction to the neutral pion mass would vanish in the chiral limit. This is not the case in our study using domain wall fermions due to the small residual mass for finite L_s [2], and we find that the size of QED correction to the neutral pion mass is approximately half that of the charged pion. To make a physical prediction, QED effects would need to be taken into account in the renormalisation of the quark mass to remove this chiral symmetry breaking effect. This effect would be much more severe for actions such as Wilson fermions which break chiral symmetry to a much larger extent [194].

An independent previous calculation of meson mass QED corrections has been made, using the stochastic method, on the same QCD gauge ensemble that we use here [2]. In Table 6.2 we

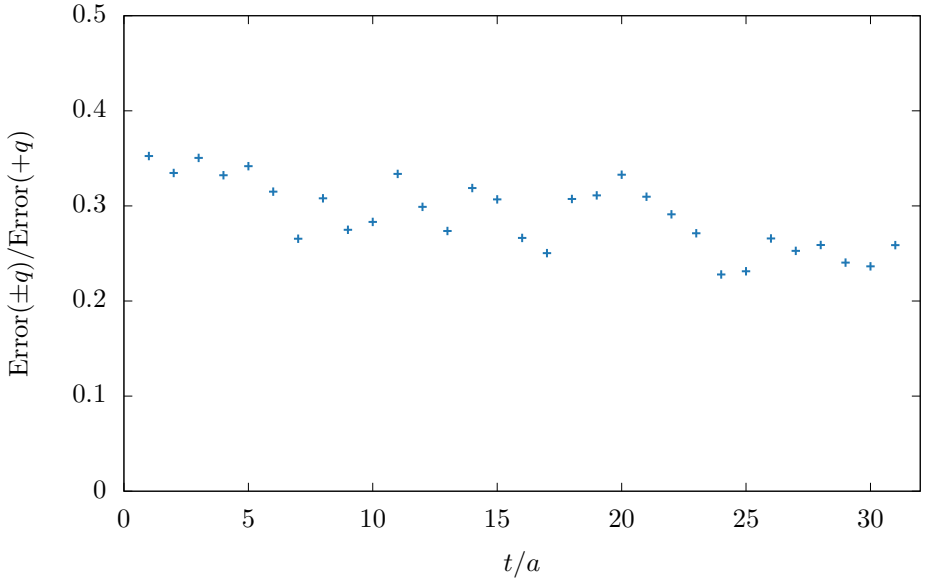

FIGURE 6.2: Ratio of statistical uncertainties in the charged kaon effective mass correction after averaging over results with opposite charges to statistical uncertainties before averaging, from the stochastic method.

	Stochastic /MeV	Perturbative /MeV
$\delta m^{\gamma}_{\pi^+}$ $(= \delta m^{\gamma}_{ud})$	3.504 ± 0.025	3.459 ± 0.016
$\delta m^{\gamma}_{\pi^0}$ $\left(= \frac{1}{2}\left[\delta m^{\gamma}_{uu} + \delta m^{\gamma}_{dd}\right]\right)$	1.555 ± 0.015	1.538 ± 0.016
$\delta m^{\gamma}_{K^+}$ $(= \delta m^{\gamma}_{us})$	2.722 ± 0.022	2.677 ± 0.013
$\delta m^{\gamma}_{K^0}$ $(= \delta m^{\gamma}_{ds})$	0.547 ± 0.005	0.548 ± 0.005

TABLE 6.1: QED corrections to pion and kaon masses, from the stochastic and perturbative methods. The values are obtained in physical units using the lattice spacing determined in the isospin-symmetric case.

q_1	q_2	$a^2\Delta m^2_\pi$ (this study)	$a^2\Delta m^2_\pi$ from [2]
$2/3\,e$	$2/3\,e$	$(5.465 \pm 0.035) \times 10^{-4}$	$(5.406 \pm 0.064) \times 10^{-4}$
$2/3\,e$	$-1/3\,e$	$(7.677 \pm 0.052) \times 10^{-4}$	$(7.654 \pm 0.056) \times 10^{-4}$
$-1/3\,e$	$-1/3\,e$	$(1.341 \pm 0.009) \times 10^{-4}$	$(1.326 \pm 0.016) \times 10^{-4}$

TABLE 6.2: Comparison of our pion squared mass differences using the stochastic method with results from [2]. q_1 and q_2 are the quark electromagnetic charges. Quantities are given in dimensionless lattice units.

compare our stochastic results for the pion squared mass difference $\Delta m^2_\pi = (m_0 + \delta m^\gamma)^2 - m_0^2$ with those from the previous study, as a cross-check. We find that our results agree with those from the previous study.

As a further check, we calculate mass corrections in both Feynman gauge and Coulomb gauge, using the Coulomb projector defined in Sec. 5.2.2. As shown in Fig. 6.3 we find agreement between the gauges, except for effective masses at small times, for which the effective mass receives contributions from the creation amplitudes of the states, which are not necessarily gauge invariant.

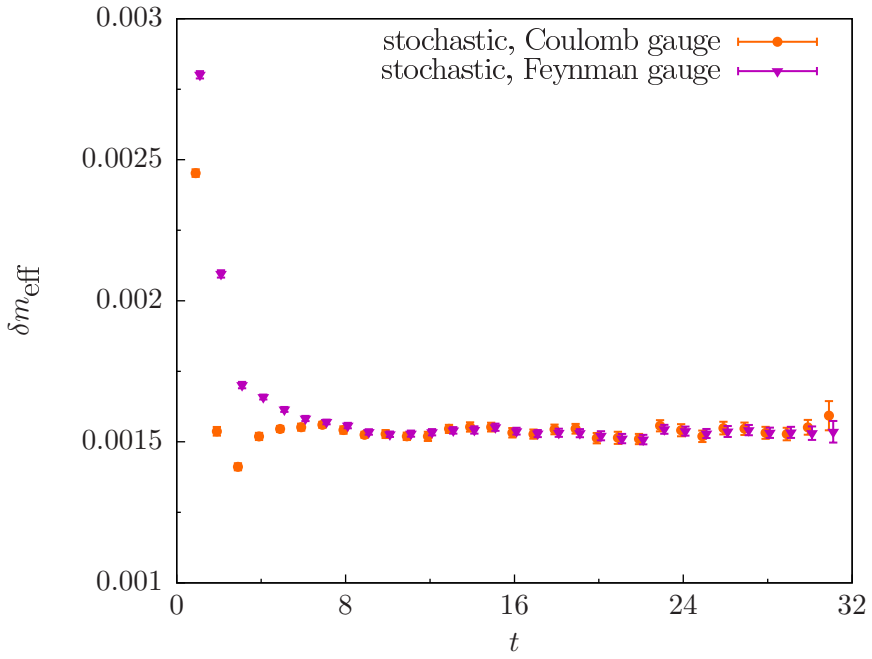

FIGURE 6.3: QED effective mass correction for a charged kaon, in Feynman gauge (purple triangles) and Coulomb gauge (orange circles), from the stochastic method.

6.2.2 Strong isospin-breaking correction

We also calculate strong isospin-breaking corrections to meson masses, by using different masses for the valence up and down quarks. As discussed in Sec. 6.1, we keep the up quark mass equal to the mass of the light sea quarks, and choose the down quark mass to reproduce approximately the physical light quark mass difference as calculated in [175]. Denoting meson masses calculated with non-degenerate light quark masses but without QED as $\tilde{m}$, we find strong isospin-breaking differences for the pion and kaon masses to be

$$\tilde{m}_{K^0} - \tilde{m}_{K^+} = 5.551 \pm 0.031\,\text{MeV}, \tag{6.7}$$

$$\tilde{m}_{\pi^+} - \tilde{m}_{\pi^0} = 0.1160 \pm 0.0012\,\text{MeV}. \tag{6.8}$$

Comparing with the results for QED corrections in Table 6.1, we find that the strong isospin-breaking correction to the kaon mass is approximately a factor of 1.8 larger than the QED correction, with the opposite sign. The strong isospin-breaking correction to the pion mass is significantly smaller. It has been shown [19, 195] that the pion mass strong isospin-breaking correction vanishes at leading order in $m_d - m_u$, and the effect we observe here is therefore an $\mathcal{O}\left((m_d - m_u)^2\right)$ correction.

6.3 HVP and a_μ

In addition to meson masses, we calculate isospin-breaking corrections to the HVP and the corresponding contribution to a_μ. This exploratory calculation serves as a further comparison of

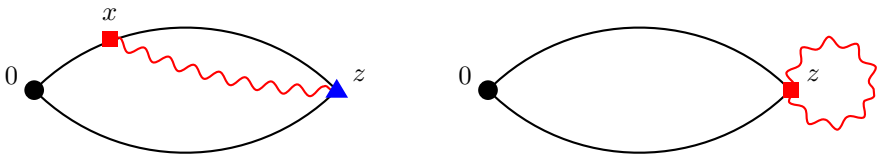

FIGURE 6.4: The QED corrections to $\left\langle V_\mu^c(z)\, V_\nu^\ell(0)\right\rangle$ which arise from the expansion of the conserved current at the sink. Insertions of the conserved current operator are denoted by a red square, and tadpole insertions by a blue triangle.

the stochastic and perturbative methods, and also as preparation for a full calculation of these effects at the physical point, which has subsequently been carried out by the RBC/UKQCD collaboration [133]. Aside from our own calculations of these effects, an independent calculation of QED corrections for strange and charm contributions to a_μ has recently emerged, using the perturbative method [132].

6.3.1 QED corrections

Our calculation of the HVP and a_μ^{HVP} follows the method described in Sec. 4.3.1. The vector two-point function in Eq. (4.23) receives two QED corrections - a correction to the two-point function itself and a correction to the multiplicative renormalisation Z_V of the local vector current:

$$\delta C_{\mu\nu}(x) = \delta Z_V q^2 \left\langle V_\mu^c(x)\, V_\nu^\ell(0)\right\rangle_0 + Z_V^0 q^2 \delta \left\langle V_\mu^c(x)\, V_\nu^\ell(0)\right\rangle, \tag{6.9}$$

where V_μ^ℓ and V_μ^c are the local and conserved vector currents defined in Eqs. (4.18) and (4.20) respectively, $\left\langle V_\mu^c(x)\, V_\nu^\ell(0)\right\rangle_0$ and Z_V^0 are the vector two-point function and multiplicative renormalisation without QED, respectively, and $\delta\left\langle V_\mu^c(x)\, V_\nu^\ell(0)\right\rangle$ and δZ_V are their QED corrections. The HVP and a_μ therefore also receive two QED corrections each:

$$\delta\Pi\left(\hat{Q}^2\right) = \delta^{Z_V}\Pi\left(\hat{Q}^2\right) + \delta^V\Pi\left(\hat{Q}^2\right), \tag{6.10}$$

$$\delta a_\mu = \delta^{Z_V} a_\mu + \delta^V a_\mu. \tag{6.11}$$

The QED correction $\delta^V\Pi$ is calculated in the stochastic method by taking the difference of the HVP with and without QED: $\delta^V\Pi\left(\hat{Q}^2\right) = \Pi\left(\hat{Q}^2\right) - \Pi_0\left(\hat{Q}^2\right)$. For the perturbative method, two extra terms are required in addition to those involving insertions of the conserved current and tadpole operators into the quark propagators. These terms arise because the conserved vector current used at the sink contains a gauge link $U_\mu(x)$. When QED corrections are included, this gauge link is multiplied by the $U(1)$ gauge link, $U_\mu(x) \to e^{iq_\alpha A_\mu(x)} U_\mu(x)$, and this dependence on the electromagnetic coupling must be taken into account in the expansion of the path integral. The two additional terms are depicted in Fig. 6.4, with conserved current insertions indicated by a red square and tadpole insertions by a blue triangle.

In the electro-quenched approximation, there is one disconnected diagram which contributes to the $\mathcal{O}(\alpha)$ correction to the HVP, shown in Fig. 6.5. We do not include this diagram in our calculation, but it would need to be included in a physically realistic calculation.

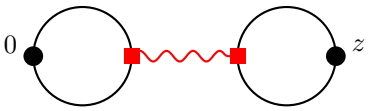

FIGURE 6.5: Disconnected diagram which contributes to the QED correction to the HVP.

	Z_V^0	δZ_V (stochastic)	δZ_V (perturbative)
u	0.70209 ± 0.00083	$(-2.674 \pm 0.043) \times 10^{-3}$	$(-2.756 \pm 0.044) \times 10^{-3}$
s	0.69737 ± 0.00017	$(-0.7102 \pm 0.0016) \times 10^{-3}$	$(-0.7139 \pm 0.0016) \times 10^{-3}$

TABLE 6.3: Values of the local vector current renormalisation Z_V^0 without QED, and its QED correction δZ_V.

The renormalisation of the local vector current can be determined by calculating both the local-conserved and local-local vector two-point functions, and taking the ratio:

$$Z_V = \frac{\sum_{\mu=1}^{3} \sum_{\vec{x}} \left\langle V_\mu^c(x)\, V_\mu^\ell(0) \right\rangle}{\sum_{\mu=1}^{3} \sum_{\vec{x}} \left\langle V_\mu^\ell(x)\, V_\mu^\ell(0) \right\rangle} \equiv \frac{C^{\ell c}(t)}{C^{\ell\ell}(t)}. \tag{6.12}$$

The QED correction to Z_V is given by

$$\begin{aligned} \delta Z_v = Z_V - Z_V^0 &= \frac{C_0^{\ell c}(t) + \delta C^{\ell c}(t)}{C_0^{\ell\ell}(t) + \delta C^{\ell\ell}(t)} - \frac{C_0^{\ell c}(t)}{C_0^{\ell\ell}(t)} \\ &= \frac{\delta C^{\ell c}(t)}{C_0^{\ell\ell}(t)} - \frac{C_0^{\ell c}(t)}{C_0^{\ell\ell}(t)} \frac{\delta C^{\ell\ell}(t)}{C_0^{\ell\ell}(t)} + \mathcal{O}\left(\alpha^2\right). \end{aligned} \tag{6.13}$$

The values of Z_V^0 and δZ_V are extracted from constant fits to the large-time region of these ratios. The results of these fits are presented in Table 6.3. The QED correction to Z_V is found to be negative, and is approximately 0.5% of Z_V^0 for the up quark, and even smaller for the strange quark.

The QED correction $\delta^V \Pi\left(\hat{Q}^2\right)$ is plotted for the up quark in Fig. 6.6 and for the strange quark in Fig. 6.7. Note that, neglecting effects of $\mathcal{O}\left(\alpha\left(m_d - m_u\right)\right)$, the down quark contribution can be obtained from the up quark results by multiplying by the charge factor $1/16$. The correlated difference of results from the two methods is also shown. We find that this correlated difference is non-zero at the 1σ level. We estimate the $\mathcal{O}\left(\alpha^2\right)$ corrections for the stochastic method, as discussed previously for the meson masses, and find that these can account for the discrepancy between the methods at large $\hat{Q}^2$.

Our results for the QED corrections to a_μ are summarised in Table 6.4. For the up quark, the QED correction $\delta^V a_\mu$ is found to be $\lesssim 1\%$ of a_μ^0. This effect is much smaller for the strange quark, and has the opposite sign. The QED correction from the vector current renormalisation, $\delta^{Z_V} a_\mu$, is negative for both quark flavours. For the up quark, this correction is the same order of magnitude as the correction $\delta^V a_\mu$, and for the strange quark it is an order of magnitude larger than $\delta^V a_\mu$. The statistical error in the QED correction to a_μ is dominated by the error from the correction $\delta^V a_\mu$ due to the vector two-point function.

The full HVP contribution to a_μ in the isospin-symmetric case is found to be

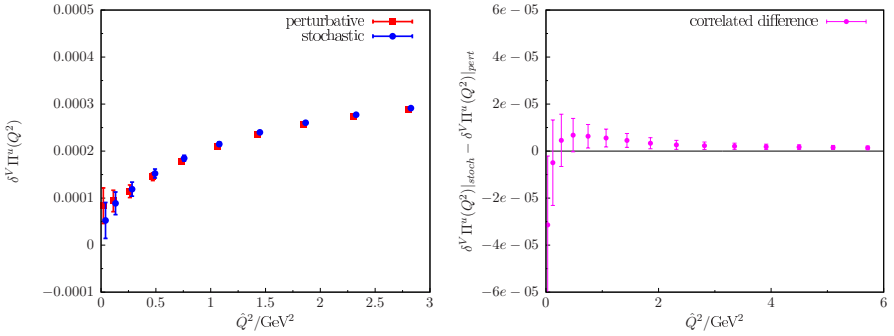

FIGURE 6.6: Left: QED correction $\delta^V \Pi\left(\hat{Q}^2\right)$ to the HVP form factor for the up quark, from the stochastic and perturbative methods. Right: Correlated difference between the two datasets on the left.

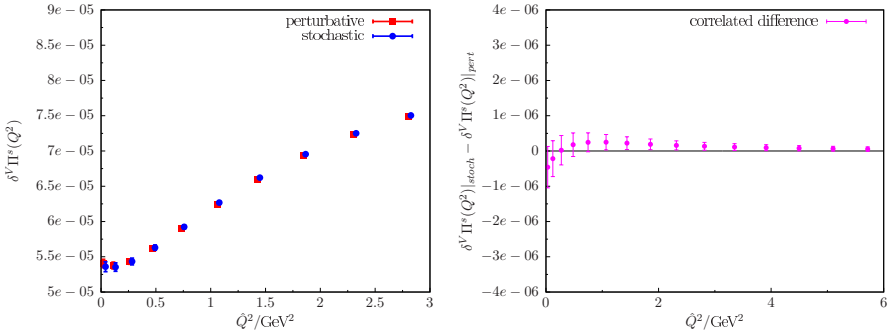

FIGURE 6.7: Left: QED correction $\delta^V \Pi\left(\hat{Q}^2\right)$ to the HVP form factor for the strange quark, from the stochastic and perturbative methods. Right: Correlated difference between the two datasets on the left.

	$a_\mu^0 \times 10^{10}$	$\delta^V a_\mu^{\text{stoch}} \times 10^{10}$	$\delta^V a_\mu^{\text{pert}} \times 10^{10}$	$\delta^{Z_V} a_\mu^{\text{stoch}} \times 10^{10}$	$\delta^{Z_V} a_\mu^{\text{pert}} \times 10^{10}$
u	310 ± 18	2.6 ± 1.2	0.7 ± 1.2	-1.212 ± 0.052	-1.249 ± 0.047
s	48.49 ± 0.23	$-0.0030 \pm .0014$	-0.0057 ± 0.0014	-0.04886 ± 0.00028	-0.04911 ± 0.00027

TABLE 6.4: QED corrections to a_μ^{HVP}, from the QED correction to the vector two-point function ($\delta^V a_\mu$) and from the vector current renormalisation ($\delta^{Z_V} a_\mu$).

$$a_\mu^0 = \frac{5}{4} a_\mu^{u,0} + a_\mu^{s,0} = 436\,(23) \times 10^{-10}, \tag{6.14}$$

in agreement with a previous result calculated on this ensemble: $a_\mu = 436\,(50) \times 10^{-10}$ [126]. The smaller statistical error achieved in our study is due to the use of stochastic $\mathbb{Z}_2$ wall sources.

The correlated difference between results for $\delta^V a_\mu$ from the two methods is $(1.95 \pm 0.94) \times 10^{-10}$ for the up quark and $(0.0027 \pm 0.0011) \times 10^{-10}$ for the strange quark, a discrepancy of more than 2σ in both cases. This is due to a smaller discrepancy between the results for the HVP form factor at small $\hat{Q}^2$, which is transferred across the entire $\hat{Q}^2$ range when the zero-mode $\Pi\,(0)$ is subtracted. The same occurs for the statistical error, which is largest at small $\hat{Q}^2$ (as seen in Fig. 6.6), which accounts for the large statistical error in $\delta^V a_\mu$ for the up quark. Better resolution for $\Pi\left(\hat{Q}^2\right)$ at small $\hat{Q}^2$ would improve the prediction of δa_μ.

	$a_\mu^0 \times 10^{10}$	$\delta^V a_\mu^{\text{stoch}} \times 10^{10}$	$\delta^V a_\mu^{\text{pert}} \times 10^{10}$
u	318 ± 11	0.65 ± 0.31	0.37 ± 0.33
s	47.98 ± 0.25	-0.0030 ± 0.0012	-0.0049 ± 0.0011

TABLE 6.5: QED corrections to a_μ^{HVP} from the QED correction to the vector two-point function, obtained using Padé R_{11} fits.

An alternative method to obtain $\Pi(0)$, which suffers less from the larger statistical errors at small $\hat{Q}^2$, is to extrapolate $\Pi\left(\hat{Q}^2\right)$ to $\hat{Q}^2 = 0$ using a fit to a suitable function. One choice for this parametrisation which has been shown to be suitable is the Padé R_{11} approximant [196]

$$R_{11}\left(\hat{Q}^2\right) = \Pi_0 + \hat{Q}^2\left(\frac{a}{b+\hat{Q}^2} + c\right). \tag{6.15}$$

Results for a_μ^0 and $\delta^V a_\mu$ obtained using this fit are given in Table 6.5. The error in $\delta^V a_\mu$ for the up quark is significantly reduced compared to the values in Table 6.4, and the central value has also decreased. The results for the strange quark are consistent with those in Table 6.4. The correlated difference between the QED corrections in Table 6.5 is $(0.27 \pm 0.26) \times 10^{-10}$ for the up quark and $(0.0019 \pm 0.0010) \times 10^{-10}$ for the strange quark, so the use of the Padé R_{11} fit reduces the discrepancy between the methods.

None of the results presented in this section have been corrected for finite-volume effects. When QED is included on the lattice, it is important to correct for finite-volume effects as they can be very large. The calculation of QED finite-volume effects is discussed in Chapter 7.

6.3.2 Strong isospin-breaking correction

As for the meson masses, we calculate strong isospin-breaking corrections to the HVP for the down quark by calculating $\Pi\left(\hat{Q}^2\right)$ without QED, once with the down quark mass and once with the up quark mass. We define the strong isospin-breaking correction to be the difference between the HVP contribution from a down quark with mass $am_d = 0.005915$ and the contribution from a quark with the isospin-symmetric light-quark mass $am_d = 0.005$. The strong isospin-breaking correction to a_μ is calculated from this form factor, with the subtracted HVP obtained using either Eq. (4.29) or Padé R_{11} fits. We find

$$\delta^s a_\mu / q_f^2 = (-6.1 \pm 8.8) \times 10^{-10} \qquad \text{using Eq. (4.29)}, \tag{6.16}$$

$$\delta^s a_\mu / q_f^2 = (-6.7 \pm 1.6) \times 10^{-10} \qquad \text{using Padé } R_{11}. \tag{6.17}$$

Using the subtracted HVP defined in Eq. (4.29), we cannot resolve the strong isospin-breaking correction at the current precision. We are able to resolve this correction using Padé R_{11} fits, and we find it to be approximately 0.9% of the isospin-symmetric value in Table 6.5.

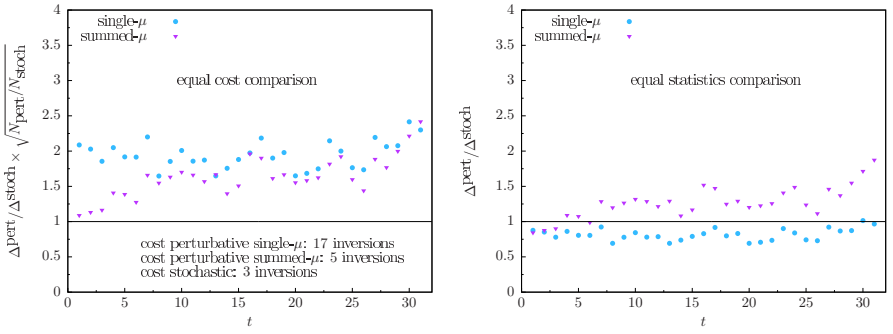

FIGURE 6.8: Ratio of statistical errors from the perturbative method to the stochastic method, for the charged kaon QED mass correction. Results using both the single-μ (blue circles) and summed-μ (purple triangles) insertions are shown. Left: equal cost. Right: equal statistics.

6.4 Comparison of statistical errors

It is interesting to compare the statistical errors of results calculated with the stochastic and perturbative methods, to investigate which method offers superior precision for the same computational cost. In order to make this comparison, adjustments must be made for the fact that the cost per QCD configuration is not equal for the different methods.

The cost is dominated by the cost of inverting quark propagators. For the stochastic method, 3 inversions are required per source position per quark flavour, since one inversion is required for the case without QED and two are required with QED (for $q = +q'$ and $q = -q'$, as discussed in Sec. 5.2.4). For the perturbative method with single-μ insertions in Feynman gauge, in which off-diagonal elements of the photon propagator do not contribute, 17 inversions are required (one propagator from the source, four sequential propagators with photon propagator insertions, four sequential propagators with noise source insertions, a further four for double sequential insertions, and four with tadpole insertions). When summed-μ insertions are used, the number of inversions required is reduced to 5 per source position and flavour.

In Fig. 6.8, the ratio of perturbative to stochastic errors for the charged kaon QED mass correction is plotted, for both single-μ and summed-μ insertions. On the left, the results are scaled to give a comparison of errors at equal computational cost. On the right, the ratio of errors is plotted for equal statistics (i.e. for data from an equal number of QCD gauge configurations and source positions). We find that, at equal cost, the stochastic method gives the smallest errors, followed by the perturbative method with summed-μ insertions. The single-μ perturbative method gives the largest errors. At equal statistics, the single-μ perturbative method is the most precise, followed by the stochastic method, with the summed-μ perturbative method giving the largest errors.

In Fig. 6.9, the same ratio of errors is plotted for the QED correction to the HVP form factor. The order of methods by size of statistical errors is the same as for the kaon mass. It should be noted, however, that this ordering may be mass-dependent, so these conclusions may not apply at physical quark masses.

From this comparison we conclude that for fixed computational cost, the stochastic method allows electro-quenched QED corrections to be calculated with smaller statistical uncertainty than the perturbative method.

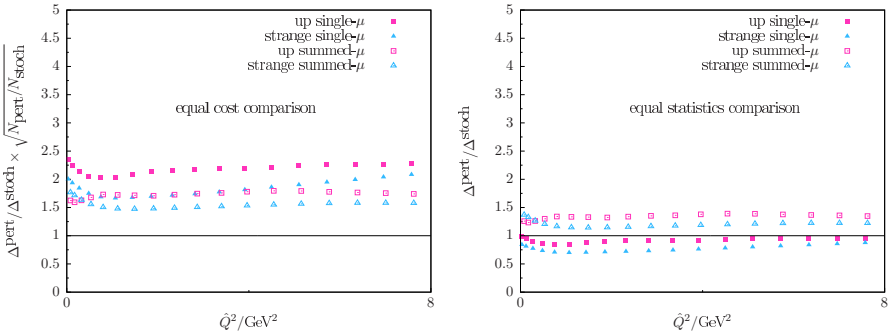

FIGURE 6.9: Comparison of statistical errors, as in Fig. 6.8, but for the QED correction to the HVP form factor for up and strange quarks.

For a calculation using unquenched QED, the comparison is less straightforward. In the perturbative setup, an unquenched calculation at $\mathcal{O}(\alpha)$ can be achieved by including contributions from quark-disconnected diagrams, while an unquenched calculation using the non-perturbative stochastic method would require generation of new QCD+QED gauge ensembles.

It has been pointed out in [177] that the stochastic and perturbative methods can be combined, by replacing the analytic photon propagator and noise sources in the perturbative approach by the photon propagator calculated from stochastic photon fields: $D_{\mu\nu}(x-y) \equiv \langle A_\mu(x) A_\nu(y) \rangle_\gamma$. This combined method requires 4 inversions per source position and flavour, and is identical to the stochastic method up to $\mathcal{O}(\alpha^2)$ effects, and can therefore be used to achieve the smaller statistical errors of the stochastic approach in an exact $\mathcal{O}(\alpha)$ calculation. It is this combination of the stochastic and perturbative methods that is used in the scalar QED calculations I will describe in Chapter 7.

6.5 Summary

We have implemented the stochastic and perturbative methods for calculating QED corrections on the lattice, introduced in Chapter 5, and used both methods to calculate electro-quenched QED$_L$ corrections to meson masses, and the HVP and its contribution to a_μ, on the same ensemble of QCD gauge configurations. We have shown that the techniques required to extract mass corrections from correlation functions depend on which method is used, since the perturbative method is exactly an $\mathcal{O}(\alpha)$ calculation while results from the stochastic method include contributions at all orders in α. The results from the two methods are in agreement, up to $\mathcal{O}(\alpha^2)$ effects which can be resolved at the precision achieved here. These results are also consistent with previous calculations on the same QCD gauge ensemble [2, 126].

The computational cost per configuration differs between the two methods, since the required number of quark propagator inversions is larger for the perturbative method than for the stochastic method. We find that, for the same computational cost, the stochastic method can produce results with statistical errors approximately half the size of those achieved from the perturbative method. This objective comparison of the two methods provides a useful input for decisions about methodology in future lattice calculations including isospin-breaking corrections.

Our study was the first to calculate isospin-breaking corrections to the HVP and a_μ^{HVP}. We found that corrections arising from QED effects on the vector two-point function and those from QED

corrections to the local vector current renormalisation Z_V are similar in magnitude. The relative QED correction to a_μ^{HVP} is approximately 0.1% for the strange-quark contribution, and statistical uncertainties place an upper bound on the size of the up-quark QED correction at approximately 1%. The strong isospin-breaking correction to a_μ^{HVP} is calculated by assigning different bare masses to the valence up- and down-quarks, and is approximately 0.9% of the isospin-symmetric value. These results were obtained at unphysical quark masses and no attempt was made to extrapolate to the physical point, so they cannot be interpreted as physical predictions. However, the magnitude of these effects suggests that both QED and strong isospin-breaking effects must be included in a full calculation of a_μ^{HVP} when aiming for 1% precision. This study served as a starting point for the inclusion of isospin-breaking effects in a physical-point lattice calculation of a_μ^{HVP} by the RBC/UKQCD collaboration, which has since been published in [133].

Chapter 7

QED Finite Volume Effects

In this chapter, I introduce a method for numerical calculations of the effects of simulating QED in a finite volume, using lattice simulations of scalar QED. The mass gap in QCD ensures that effects due to the finite volume of the lattice fall off exponentially with the spatial extent L of the lattice, provided L is significantly larger than the inverse pion mass [107]. In QED, however, there is no mass gap and the massless photon ensures that electromagnetism is a long-range interaction. Finite volume (FV) effects for QED are therefore much larger than those for QCD, typically scaling with inverse powers of L rather than exponentially [21], and they must be taken into account in any physical calculation of QED effects on the lattice.

As an example of the size of QED FV effects, Table 7.1 contains our results for the QED corrections to charged pion and kaon masses from the stochastic method (as quoted in Table 6.1), along with the same quantities corrected for FV effects (calculated using a result from [21]). The estimated FV correction is greater than 30% of the uncorrected QED effect.

FV effects arise from long-distance properties, and do not therefore depend strongly on UV properties of the system. As a result, leading FV corrections are often "universal", meaning that they are independent of hadron structure and cutoff effects. Leading FV effects can therefore be studied analytically using low-energy effective field theories in which hadrons are treated as point particles. Universal FV corrections for mesons can be calculated in scalar QED, and for baryons in spinor QED. In momentum space, infinite-volume integrals over momentum become discrete sums in finite volume, so the task of calculating FV corrections consists of the derivation of sum-integral differences for a set of master integrals in an appropriate effective field theory.

Much work has been done to determine QED FV corrections for hadron masses. These corrections were first calculated, within the QED$_L$ scheme, in [182]. The universal FV corrections, and the leading non-universal corrections for composite particles, were calculated using non-relativistic QED (NRQED) as an effective field theory. The same FV corrections have also been

	δm^{FV} /MeV	$\delta m^{\mathrm{inf\,V}}$ /MeV
$\delta m^{\gamma}_{\pi^+}$	3.504 ± 0.025	4.597 ± 0.025
$\delta m^{\gamma}_{K^+}$	2.722 ± 0.022	3.699 ± 0.022

TABLE 7.1: Results for the QED correction to pion and kaon masses on a $24^3 \times 64$ lattice, obtained using the stochastic method, and the same results after correcting for finite volume effects.

calculated using relativistic QED [21]. A discrepancy between the results from these two methods has since been explained through the observation that either additional contributions from antiparticles, or a residual mass term, must be included in the NRQED approach [7, 183, 197].

Calculations of hadron mass FV corrections have also been made for other QED schemes. For QED_M, in which IR regularisation is achieved by introducing a non-zero photon mass, hadron mass FV effects are calculated in [24]. For QED_C, in which boundary conditions are periodic up to charge conjugation, mass FV corrections are calculated in [25].

Recently, motivated by lattice QCD+QED calculations at larger-than-physical electric charges, FV corrections to next-to-leading-order QED effects on hadron masses have been calculated [198].

The universal QED FV corrections for leptonic decay rates have been calculated in [181], using an extension of the method used in [21] for hadron masses.

An alternative proposal for calculating QED effects in the hadronic light-by-light contribution to a_μ was recently made. Instead of calculating and correcting for large FV effects, two groups have demonstrated methods for treating the photon in infinite-volume QED while still simulating QCD on a finite-volume lattice [164, 166]. The authors of [164] present numerical results which show that the QED FV effects approach the infinite-volume limit exponentially, although they acknowledge that the reduction of FV effects seen for the HLbL may not be achieved in other contexts.

As presented in Sec. 6.3 and in [3], we have calculated QED corrections to the HVP for the first time, using the QED_L scheme. Several other calculations of these corrections have been carried out more recently [132–135]. With QED corrections now becoming important in lattice calculations of the muon $g-2$, it is important to correct for QED FV effects. An analytical calculation of finite volume effects for the HVP is a two-loop calculation, and as such is not trivial. An alternative calculation is therefore desirable as a cross-check. Numerical simulations of lattice scalar QED offer such an alternative. Such a calculation can make use of the computationally cheap generation of QED gauge ensembles introduced in Sec. 5.2, and the absence of fermions removes complications resulting from the problem of fermion doubling. Lattice scalar QED simulations are therefore computationally cheap, and can offer an efficient numerical calculation of QED finite volume effects.

A strategy for making numerical calculations of QED FV effects is introduced and applied in this chapter. The strategy can be summarised as follows: leading-order QED corrections to physical quantities of interest are calculated from the path integral using lattice simulations of scalar QED, and this is repeated for several lattice volumes. The volume dependence of the QED corrections can then be compared with analytical calculations. In the absence of an analytical FV calculation, an ansatz could be assumed for the volume dependence of the QED corrections, and coefficients could be extracted through a fit to the data points.

An efficient method for simulating scalar QED on the lattice is described in Sec. 7.1. This method is used to calculate FV effects for the self-energy of a charged scalar particle, and validated against an analytical calculation of the same effects, in Sec. 7.2. Finally, FV effects for the HVP are calculated numerically, and compared with analytical calculations, in Sec. 7.3. The numerical and analytical calculations of scalar self-energy FV effects have been submitted for publication in [7], and the HVP FV calculations are in preparation for publication in [8]. This method could be applied to study the leading QED FV behaviour of any hadronic quantity for

which scalar QED is a valid effective field theory, making this a valuable tool for investigating QED FV effects on quantities which would be difficult to calculate analytically.

7.1 Numerical simulations of lattice scalar QED

The method used here for lattice scalar QED simulations is the combination of the stochastic and perturbative methods introduced in [177] and discussed briefly in Sec. 6.4. In addition, the absence of non-perturbative interactions in the theory enables an efficient method for calculating charged scalar propagators, which is described in this section.

7.1.1 Lattice scalar QED action

We define the discretised scalar QED action as

$$S\left[\phi, A\right] = S_{\phi}\left[\phi, A\right] + S_{\gamma}\left[A\right] , \tag{7.1}$$

where $S_{\gamma}\left[A\right]$ is the Feynman-gauge QED_L action defined in Eq. (5.12) and

$$S_{\phi}\left[\phi, A\right] = \frac{a^4}{2} \sum_{x} \left(\sum_{\mu} \left[D_{\mu}\phi\left(x\right)\right]^* D_{\mu}\phi\left(x\right) + m^2 \left|\phi\left(x\right)\right|^2 \right) , \tag{7.2}$$

where $\phi\left(x\right)$ is a complex scalar field. The covariant forward derivative is defined as

$$D_{\mu} f\left(x\right) = a^{-1}\left[U_{\mu}\left(x\right) f\left(x + a\hat{\mu}\right) - f\left(x\right)\right] , \tag{7.3}$$

with $U\left(1\right)$ gauge link $U_{\mu}\left(x\right) \equiv e^{iqaA_{\mu}(x)}$ for a scalar with electromagnetic charge q.

Defining also a covariant backward derivative

$$D^*_{\mu} f\left(x\right) = a^{-1}\left[f\left(x\right) - U^{\dagger}_{\mu}\left(x - a\hat{\mu}\right) f\left(x - a\hat{\mu}\right)\right] , \tag{7.4}$$

we can rewrite Eq. (7.2) as

$$S_{\phi}\left[\phi, A\right] = \frac{a^4}{2} \sum_{x} \phi^*\left(x\right) \Delta\phi\left(x\right) , \tag{7.5}$$

$$\Delta = -\sum_{\mu} D^*_{\mu} D_{\mu} + m^2 . \tag{7.6}$$

Expectation values of observables are defined through the path integral

$$\left\langle O \right\rangle = \frac{1}{\mathcal{Z}} \int \mathcal{D}A \int \mathcal{D}\phi\, O\left[\phi, A\right] e^{-S_{\phi}[\phi, A]} e^{-S_{\gamma}[A]} . \tag{7.7}$$

Performing Gaussian integration over the scalar field, the path integral becomes

$$\langle O \rangle = \frac{1}{\mathcal{Z}} \int \mathcal{D}A \, O_{\text{Wick}} \left[\Delta^{-1}, A\right] \sqrt{\det\left(\Delta^{-1}\right)} e^{-S_\gamma[A]} \,, \tag{7.8}$$

where O_{Wick} is obtained by summing all Wick contractions of O.

Generation of the gauge fields follows the method laid out in Sec. 5.2. We work in the quenched theory, in which we set $\sqrt{\det\left(\Delta^{-1}\right)} = 1$ in the path integral, so that gauge field configurations can be generated independently of the scalar field. As explained in Sec. 6.4, an unquenched calculation of QCD+QED at fixed order in α can be achieved by including contributions from diagrams in which photons couple to disconnected quark loops. In scalar QED the additional contributions required for an unquenched calculation are those from diagrams involving disconnected scalar loops. At $\mathcal{O}(\alpha)$ there are no such disconnected diagrams, and there are therefore no electro-quenching effects at leading order in this theory.

7.1.2 Inverting the scalar propagator

The Wick-contracted operator which enters into the path integral in Eq. (7.8) is constructed from scalar propagators and gauge fields. Therefore, after generating $U(1)$ gauge configurations, the next step is to calculate the scalar propagator Δ^{-1}. This could be done using a conjugate gradient algorithm, as described in Sec. 3.5.2, but we instead use an alternative method to calculate a perturbative expansion of the scalar propagator, making use of the fast Fourier transform (FFT) algorithm [199].

The motivation for using this method instead of the commonly-used CG method is twofold. Firstly, this method allows a perturbative treatment of the QED effects up to fixed order, which facilitates comparison with analytical calculations. Secondly, the computational cost of the CG algorithm scales with the condition number of the matrix to be inverted, which diverges as the mass decreases to zero [200]. The cost of this FFT-based method, on the other hand, is independent of the input mass, so we expect this method to be more efficient than CG for small masses.

Using the translation operator

$$\tau_\mu f(x) = f(x + a\hat{\mu}) \tag{7.9}$$

and Eqs. (7.3), (7.4) and (7.6), the operator Δ can be written as

$$\Delta = a^{-2}\left[2 - e^{iqaA_\mu}\tau_\mu - \tau_{-\mu}e^{-iqaA_\mu}\right] + m^2 \,. \tag{7.10}$$

Expanding in powers of the electromagnetic charge q gives

FIGURE 7.1: The four diagrams which correspond to the expansion to $\mathcal{O}(\alpha)$ of the charged scalar propagator Eq. (7.15). We refer to these diagrams as "free", "photon-vertex", "sunset" and "tadpole" respectively.

$$\Delta = \Delta_0 + q\Delta_1 + q^2\Delta_2 + \mathcal{O}\left(q^3\right) , \tag{7.11}$$

$$\Delta_0 = -\sum_\mu \partial^*_\mu \partial_\mu + m^2 , \tag{7.12}$$

$$\Delta_1 = -ia^{-1}\sum_\mu \left(A_\mu \tau_\mu - \tau_{-\mu} A_\mu\right) , \tag{7.13}$$

$$\Delta_2 = \frac{1}{2}\sum_\mu \left(A^2_\mu \tau_\mu + \tau_{-\mu} A^2_\mu\right) . \tag{7.14}$$

We can then expand the scalar propagator:

$$\Delta^{-1} = \Delta_0^{-1} - q\Delta_0^{-1}\Delta_1\Delta_0^{-1} + q^2\Delta_0^{-1}\Delta_1\Delta_0^{-1}\Delta_1\Delta_0^{-1} - q^2\Delta_0^{-1}\Delta_2\Delta_0^{-1} + \mathcal{O}\left(q^3\right) . \tag{7.15}$$

The four terms in this expansion to $\mathcal{O}(\alpha)$ correspond to the four diagrams in Fig. 7.1. The first term is the free scalar propagator, the second is a scalar propagator with a single photon vertex, and the final two terms are $\mathcal{O}(\alpha)$ corrections which we refer to as the "sunset" and "tadpole" diagrams respectively. It is worth noting that the operators Δ_1 and Δ_2 correspond to the conserved current and tadpole operators discussed in Sec. 5.3 in the context of the perturbative method.

We can use a Fourier representation of the translation operator:

$$\tau_\mu = \mathcal{F}^{-1}\psi_\mu\mathcal{F}, \tag{7.16}$$

where $\psi_\mu(p) \equiv e^{iap_\mu}$, and of the free scalar propagator:

$$\Delta_0^{-1} = \mathcal{F}^{-1}G_0\mathcal{F}, \tag{7.17}$$

where

$$G_0(p) \equiv \frac{1}{(\hat{p}^2 + m^2)} \tag{7.18}$$

is the momentum-space free scalar propagator, and $\hat{p}_\mu \equiv \frac{2}{a}\sin\left(\frac{ap_\mu}{2}\right)$ is the lattice momentum. The operators Δ_1 and Δ_2 can then be expressed as

$$\Delta_1 = -ia^{-1} \sum_\mu \left[A_\mu \mathcal{F}^{-1} \psi_\mu \mathcal{F} - \mathcal{F}^{-1} \psi_\mu^* \mathcal{F} A_\mu \right], \tag{7.19}$$

$$\Delta_2 = \frac{1}{2} \sum_\mu \left[A_\mu^2 \mathcal{F}^{-1} \psi_\mu \mathcal{F} + \mathcal{F}^{-1} \psi_\mu^* \mathcal{F} A_\mu^2 \right]. \tag{7.20}$$

Using Eqs. (7.15), (7.17), (7.19) and (7.20), along with stochastic $U(1)$ gauge fields $A_\mu(x)$, the charged scalar propagator can be calculated to $\mathcal{O}(\alpha)$ using 32 Fourier transforms, which can be computed using the FFT algorithm.

In order to calculate expectation values, scalar propagators must be computed for a large number of $U(1)$ gauge configurations. The propagator calculation can be optimised by calculating quantities which do not depend on the photon field $A_\mu(x)$ only once, caching these in memory and re-using them for the inversion on each gauge configuration. We choose to cache the phase factors $\psi_\mu(p)$ for $\mu = 1, 2, 3, 4$ and the momentum-space free propagator $G_0(p)$, to avoid unnecessary repetitive calculation of trigonometric quantities. We also cache the position-space free scalar propagator $\mathcal{F}^{-1} G_0 \mathcal{F} \phi$ and the quantity $G_0 \mathcal{F} \phi$ for our chosen source field ϕ, which reduces the number of FFTs required per configuration from 32 to 30. We find that this process reduces the inversion time per configuration by a factor greater than 2 for all lattice volumes investigated.

Greater speedup could be achieved by also caching the quantities $\mathcal{F}^{-1} \psi_\mu G_0 \mathcal{F} \phi$ for $\mu = 1, 2, 3, 4$, which would remove a further 8 FFTs per configuration. However, it is important to remember the memory requirements of caching these quantities, which can be large. For example, for a $64^3 \times 128$ lattice, storing a single complex scalar field in double precision requires 537 MB in memory, so storing large numbers of such fields can quickly use up memory resources.

This propagator inversion method has been implemented in Grid, a data-parallel C++ library developed by members of the RBC/UKQCD collaboration [201]. Grid is designed to provide a simple high-level interface for implementing physics calculations, while being optimised at a low level to provide good performance across a range of computational architectures. It is hoped that by implementing our scalar QED simulations in Grid, it will be straightforward to extend this framework in the future to calculate FV effects for new quantities, while still achieving good and portable performance.

7.2 Scalar self energy finite-volume effects

In order to validate this numerical approach to the calculation of FV corrections, it is useful to compare with results from analytical calculations of FV effects. Perhaps the simplest quantity to calculate in our numerical scalar QED setup is the scalar self energy, which can be calculated from a single charged scalar propagator. In Euclidean space, on a continuous space-time, the self energy $\Sigma(p)$, for a scalar particle with momentum $p = (p_0, \mathbf{p})$, is defined through the first-order electromagnetic corrections to the scalar propagator $G(p)$:

$$G(p) = \frac{1}{p^2+m^2} + \frac{\Sigma(p)}{(p^2+m^2)^2} + \mathcal{O}\left(\alpha^2\right)$$
$$= G_0(p) + \Sigma(p)G_0^2(p) + \mathcal{O}\left(\alpha^2\right) . \tag{7.21}$$

That is, the self energy is the sum of the sunset and tadpole diagrams in Fig. 7.1 with external scalar propagators amputated. In infinite volume, $\Sigma(p)$ is given by the integral of a kernel $K(k,p)$ over continuous photon momentum $k = (k_0, \mathbf{k})$:

$$\Sigma(p) = \int \frac{d^4k}{(2\pi)^4} K(k,p) . \tag{7.22}$$

In a periodic hypercubic spacetime, with infinite time extent and finite spatial extent L, the self-energy in the QED_L scheme is

$$\Sigma^{(L)}(p) = \frac{1}{L^3} {\sum_{\mathbf{n}\in\mathbb{Z}^3}}' \int \frac{dk_0}{2\pi} K\left(\left(k_0, \frac{2\pi}{L}\mathbf{n}\right), p\right) . \tag{7.23}$$

where the photon spatial momentum has been rescaled so that $\mathbf{k} = \frac{2\pi}{L}\mathbf{n}$ where the components of $\mathbf{n}$ are integers. The self energy FV effect is defined as the difference between the finite-volume and infinite-volume self energy. Defining the sum-integral difference

$$\Delta'_{\mathbf{n}} = {\sum_{\mathbf{n}\in\mathbb{Z}^3}}' - \int d^3\mathbf{n} , \tag{7.24}$$

the self energy FV effect can be written

$$\Delta\Sigma(p) = \Sigma^{(L)}(p) - \Sigma(p) = \frac{1}{L^3}\Delta'_{\mathbf{n}} \int \frac{dk_0}{2\pi} K\left(\left(k_0, \frac{2\pi}{L}\mathbf{n}\right), p\right) , \tag{7.25}$$

7.2.1 Analytical scalar self energy FV effect

Analytical expressions for the FV effect on the QED_L scalar self-energy are summarised here. In the rest frame of the scalar particle, with $p_0^2 = -m^2$ and $\mathbf{p} = \mathbf{0}$, the self energy reduces to the lowest-order electromagnetic correction to the squared mass. In this case, the FV effect is [21, 182]:

$$\Delta m^2(L) = -\frac{q^2}{4\pi}\frac{\kappa}{L}\left(m + \frac{2}{L}\right) + \mathcal{O}\left(e^{-mL}\right) , \tag{7.26}$$
$$\kappa = 2.837297\,(1) , \tag{7.27}$$

where q is the electromagnetic charge of the scalar and m is the bare scalar mass. This relation gives the universal FV corrections to the squared mass of all spin-0 particles, including composite particles such as the pseudoscalar mesons, up to structure-dependent terms which have been shown to be no larger than $\mathcal{O}\left(\alpha/L^3\right)$ [21, 181, 182].

This calculation has been extended to the case of the self energy of a moving charged scalar particle, in both on-shell ($p^2 = -m_0^2$) and off-shell ($p^2 \neq -m_0^2$) frames [7]. Defining the on-shell energy

$$\omega(\mathbf{p}) = \sqrt{\mathbf{p}^2 + m^2} \tag{7.28}$$

and the velocity

$$\mathbf{v} = \frac{\mathbf{p}}{\omega(\mathbf{p})}\,, \tag{7.29}$$

the FV effect on the self energy of a scalar particle with on-shell momentum $p_{\text{o.s.}} = (i\omega(\mathbf{p}), \mathbf{p})$ is

$$\Delta\Sigma(p_{\text{o.s.}}) = m^2 q^2 \left\{ \frac{1}{\gamma(|\mathbf{v}|)} \frac{c_{2,1}(\mathbf{v})}{4\pi^2 mL} + \frac{c_1}{2\pi(mL)^2} + \left[\frac{1}{\gamma(|\mathbf{v}|)^3} - \frac{1}{\gamma(|\mathbf{v}|)} \right] \frac{1}{2(mL)^3} + \mathcal{O}\left(e^{-mL}\right) \right\}, \tag{7.30}$$

where $\gamma(|\mathbf{v}|) = \left(1 - |\mathbf{v}|^2\right)^{-1/2}$ and the c coefficients are

$$c_{j,k}(\mathbf{v}) = \Delta'_{\mathbf{n}} \left[\frac{1}{|\mathbf{n}|^j \left(1 - \mathbf{v}\cdot\hat{\mathbf{n}}\right)^k} \right], \quad c_j = c_{j,k}(\mathbf{0})\,. \tag{7.31}$$

An efficient method for calculating $c_{j,k}(\mathbf{v})$ is given in [7], and the rest-frame coefficients have the values

$$c_0 = -1, \quad c_1 = -2.83729748\ldots, \quad c_2 = \pi c_1\,, \tag{7.32}$$

from which it can be seen that Eq. (7.30) reduces to Eq. (7.26) when $\mathbf{p} = \mathbf{0}$.

Introducing the σ-ratio

$$\sigma = \frac{p^2 + m^2}{\omega(\mathbf{p})^2} = \frac{p_0^2}{\omega(\mathbf{p})^2} + 1\,, \tag{7.33}$$

which is positive and vanishes at the on-shell point, the self energy FV effect in the off-shell case is

$$\begin{aligned}\Delta\Sigma(p) = m^2 q^2 \Bigg\{ & \frac{1}{\gamma(|\mathbf{v}|)^2} \frac{c_1}{\pi\sigma(mL)^2} \\ & + \left[\left(\frac{4}{\sigma^2} - \frac{2}{\sigma} \right) \frac{1}{\gamma(|\mathbf{v}|)^3} + \left(\frac{1}{2} - \frac{2}{\sigma} \right) \frac{1}{\gamma(|\mathbf{v}|)} \right] \frac{1}{(mL)^3} + \mathcal{O}\left(\frac{1}{(mL)^4} \right) \Bigg\}\,. \end{aligned} \tag{7.34}$$

7.2.2 Extracting the self energy from lattice simulation data

The lattice scalar self energy is defined through the electromagnetic corrections to the momentum-space scalar propagator as in Eq. (7.21), with the free momentum-space lattice scalar propagator

defined in Eq. (7.18). The momentum-space propagator $G(p)$ is the Fourier transform of the charged scalar 2-point function $C(x) = \langle\phi(x)\phi^*(0)\rangle$:

$$G(p) = \mathcal{F}C(x) = a^4 \sum_{x\in\Lambda} C(x)e^{-ip\cdot x}\,. \tag{7.35}$$

On the lattice, the $C(x)$ can be calculated as

$$C(x) = \left\langle \Delta^{-1}\delta(x)\right\rangle_\gamma\,, \tag{7.36}$$

where the subscript γ denotes the expectation value over the $U(1)$ gauge fields. This can be computed to $\mathcal{O}(\alpha)$ following the method in Sec. 7.1.

The expectation value of the photon-vertex diagram in Fig. 7.1, corresponding to the $\mathcal{O}(q)$ term in Eq. (7.15), must vanish due to charge-conjugation symmetry. The 2-point function $C(x)$ can therefore be decomposed into the tree-level function $C_0(x)$ and $\mathcal{O}(\alpha)$ QED corrections $C_1(x)$, where

$$C_0(x) = \Delta_0^{-1}\delta(x)\,, \tag{7.37}$$

$$C_1(x) = q^2\left\langle\left[\Delta_0^{-1}\Delta_1\Delta_0^{-1}\Delta_1\Delta_0^{-1} - \Delta_0^{-1}\Delta_2\Delta_0^{-1}\right]\delta(x)\right\rangle_\gamma\,. \tag{7.38}$$

The momentum modes directly accessible on the lattice are those of the form $p = \left(\frac{2\pi}{T}n_0, \frac{2\pi}{L}\mathbf{n}\right)$, where n_0 and the components of $\mathbf{n}$ are integers. These modes do not include on-shell momentum, since the on-shell condition requires p_0 to be imaginary. Different methods to extract the self-energy from lattice simulation data are therefore required in the on-shell and off-shell cases.

7.2.2.1 Off-shell

For momentum $p \in \tilde{\Lambda}$, the self energy is given by

$$\Sigma(p) = \frac{G(p) - G_0(p)}{G_0(p)^2} \tag{7.39}$$

$$= a^4\left(\hat{p}^2 + m^2\right)^2 \sum_{x\in\Lambda} C_1(x)e^{-ip\cdot x}\,. \tag{7.40}$$

7.2.2.2 On-shell

On the lattice, the on-shell condition is $\hat{p}^2_{\text{o.s.}} = -m^2$. Defining a lattice energy

$$\hat{\omega}(\mathbf{p}) = \frac{2}{a}\sinh^{-1}\left(\frac{a\omega(\hat{\mathbf{p}})}{2}\right) = \frac{2}{a}\sinh^{-1}\left(\frac{a}{2}\sqrt{\hat{\mathbf{p}}^2 + m^2}\right)\,, \tag{7.41}$$

the on-shell momentum is $p_{\text{o.s.}} = (i\hat{\omega}(\mathbf{p}), \mathbf{p})$. Since this momentum is not directly accessible on the lattice, the on-shell self energy must be extracted from the large-time behaviour of the 2-point function, as explained in Sec. 3.6.2.

For a chosen spatial momentum $\mathbf{p}$, the time-momentum representation of the scalar 2-point function is

$$C(t,\mathbf{p}) = \sum_{\mathbf{x}\in\mathbf{\Lambda}} C\left((t,\mathbf{x})\right) e^{-i\mathbf{p}\cdot\mathbf{x}}\,, \tag{7.42}$$

where $\mathbf{\Lambda}$ is the three-dimensional sub-lattice of the full lattice Λ. This can again be decomposed into the tree-level and first-order electromagnetic contributions $C_0(t,\mathbf{p})$ and $C_1(t,\mathbf{p})$, respectively.

As this is an exact $\mathcal{O}(\alpha)$ calculation, the self energy is extracted using the ratio method used for calculating meson masses from perturbative data in Sec. 6.2.1. Due to the high precision achievable from scalar QED calculations, however, we find that lattice cut-off effects can be resolved, and so a careful derivation of this method in lattice perturbation theory is required.

On a lattice with infinite time extent T, the tree-level and first-order time-momentum correlators are

$$C_0(t,\mathbf{p}) = \int_{-\frac{\pi}{a}}^{\frac{\pi}{a}} \frac{dp_0}{2\pi} \frac{e^{ip_0 t}}{\hat{p}^2 + m^2}\,, \tag{7.43}$$

$$C_1(t,\mathbf{p}) = \int_{-\frac{\pi}{a}}^{\frac{\pi}{a}} \frac{dp_0}{2\pi} \frac{\Sigma(p)}{\left(\hat{p}^2 + m^2\right)^2} e^{ip_0 t}\,. \tag{7.44}$$

The integrands in Eqs. (7.43) and (7.44) have poles at the on-shell momentum $p_{\text{o.s.}}$. By integrating over the rectangular contour in Fig. 7.2, the p_0 integral can be evaluated using the residue theorem, giving

$$C_0(t,\mathbf{p}) = \frac{e^{-\hat{\omega}(\mathbf{p})|t|}}{2\bar{\omega}(\mathbf{p})}\,, \tag{7.45}$$

$$C_1(t,\mathbf{p}) = \frac{e^{-\hat{\omega}(\mathbf{p})|t|}}{4\bar{\omega}(\mathbf{p})^3}\left[\left(1 + \frac{a^2}{2}\omega(\hat{\mathbf{p}})^2 + \bar{\omega}(\mathbf{p})\,|t|\right)\Sigma(p_{\text{o.s.}}) - i\bar{\omega}(\mathbf{p})\,\frac{\partial\Sigma(p)}{\partial p_0}\bigg|_{p_{\text{o.s.}}}\right] + \ldots\,, \tag{7.46}$$

where

$$\bar{\omega}(\mathbf{p}) = \frac{1}{a}\sinh\left[a\hat{\omega}(\mathbf{p})\right] = \omega(\hat{\mathbf{p}})\sqrt{1 + \left(\frac{a\omega(\hat{\mathbf{p}})}{2}\right)^2}\,. \tag{7.47}$$

The ellipsis in Eq. (7.46) represents contributions from poles of $\Sigma(p)$ corresponding to intermediate scalar+photon states.

An effective self energy can be constructed from the correlators C_0 and C_1:

$$\Sigma_{\text{eff.}}(t,\mathbf{p}) = 2\bar{\omega}(\mathbf{p})\frac{\text{sign}(t)}{a}\left[\frac{C_1(t+a,\mathbf{p})}{C_1(t+a,\mathbf{p})} - \frac{C_1(t,\mathbf{p})}{C_1(t,\mathbf{p})}\right] \tag{7.48}$$

$$= \Sigma(p_{\text{o.s.}}) + \ldots\,. \tag{7.49}$$

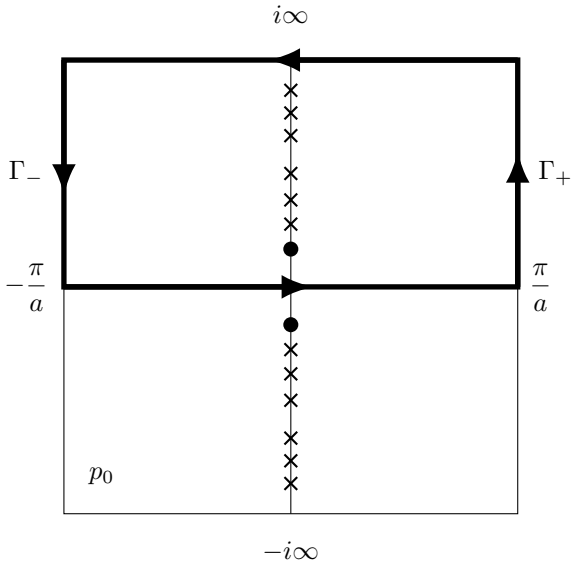

FIGURE 7.2: Rectangular contour used to evaluate the integrals in Eqs. (7.43), (7.44) and (7.53). The integrals on the intervals Γ_+ and Γ_- cancel by periodicity. The dots represent the poles contributing to the scalar two-point function contribution Eq. (7.56) and the crosses the scalar-photon scattering states contributing to Eq. (7.57).

Again, the ellipsis represents contributions from excited states, which vanish in the limit $|t| \to \infty$. At sufficiently large times the effective self energy will reach a plateau, and the on-shell self energy can be extracted by fitting a constant to the plateau region. As in Sec. 6.2.1, the effective self energy can be corrected for the effect of periodic boundary conditions on a lattice with finite time extent T:

$$\Sigma_{\text{eff.}}(t,\mathbf{p}) = 2\bar{\omega}(\mathbf{p}) \frac{\frac{\text{sign}(t)}{a}\left[\frac{C_1(t+a,\mathbf{p})}{C_1(t+a,\mathbf{p})} - \frac{C_1(t,\mathbf{p})}{C_1(t,\mathbf{p})}\right]}{\left(\frac{T}{2}-t\right)\tanh\left(\hat{\omega}(\mathbf{p})\left(\frac{T}{2}-t\right)\right) - \left(\frac{T}{2}-(t+a)\right)\tanh\left(\hat{\omega}(\mathbf{p})\left(\frac{T}{2}-(t+a)\right)\right)} \,. \tag{7.50}$$

7.2.2.3 Excited-state contributions

The excited-state contributions to $\Sigma_{\text{eff.}}(t,\mathbf{p})$ come from states with a scalar and a photon, with combined energy

$$\hat{\omega}_{\phi\gamma}(\mathbf{p},\mathbf{k}) = \hat{\omega}(\mathbf{p}) + \hat{\omega}_\gamma(\mathbf{k}) \,, \tag{7.51}$$

where $\mathbf{k}$ is the spatial momentum of the photon and $\hat{\omega}_\gamma(\mathbf{k})$ is its energy

$$\hat{\omega}_\gamma(\mathbf{k}) = \frac{2}{a}\sinh^{-1}\left(\frac{a\left|\hat{\mathbf{k}}\right|}{2}\right) \,. \tag{7.52}$$

These contributions are suppressed at large times by a decaying exponential of the form $e^{-(\hat{\omega}_{\phi\gamma}(\mathbf{p},\mathbf{k})-\hat{\omega}(\mathbf{p}))|t|}$, and the ground-state dominance at large times relies entirely on the exponential suppression from the energy gap $\hat{\omega}_{\phi\gamma}(\mathbf{p},\mathbf{k}) - \hat{\omega}(\mathbf{p})$. This gap vanishes in the infinite

volume limit, creating a branch cut at the particle pole. This means that large-volume lattice calculations of the effective self energy are expected to be severely contaminated by the excited spectrum.

Since scalar QED is a perturbative theory, the excited-state contributions to $C_1(t,\mathbf{p})$ can be calculated analytically and subtracted from the lattice data. It is important to keep in mind, however, that in a full QCD+QED calculation this would not be possible, and excited-state contamination may result in significant systematic errors in large-volume lattice QCD+QED calculations of spectral quantities.

The self energy is the sum of the amputated $\mathcal{O}(\alpha)$ diagrams in Fig. 7.1:

$$\Sigma(p) = \frac{q^2}{L^3}\sum_{\mathbf{k}\in\tilde{\mathbf{\Lambda}}}{}' \int_{-\frac{\pi}{a}}^{\frac{\pi}{a}} \frac{dk_0}{2\pi} \left\{ \frac{4-\frac{a^2}{2}\hat{p}^2}{\hat{k}^2} - \frac{\left(\widehat{2p-k}\right)^2}{\hat{k}^2\left[\left(\widehat{p-k}\right)^2+m^2\right]} \right\}, \tag{7.53}$$

where the two terms in the integrand are from the tadpole and sunset diagrams, respectively. The integrand has poles in the upper complex plane at $k_0 = i\hat{\omega}_\gamma(\mathbf{k})$ and $k_0 = p_0 + i\hat{\omega}(\mathbf{p}-\mathbf{k})$. Taking the k_0 integral over the contour in Fig. 7.2 gives

$$\begin{aligned}\Sigma(p) = \frac{q^2}{L^3}\sum_{\mathbf{k}\in\tilde{\mathbf{\Lambda}}}{}' \Bigg\{ &\frac{2-\frac{a^2}{4}\hat{p}^2}{\bar{\omega}_\gamma(\mathbf{k})} - \frac{\frac{4}{a^2}\sin[ap_0 - \frac{ia}{2}\hat{\omega}_\gamma(\mathbf{k})]^2 + (\widehat{2\mathbf{p}-\mathbf{k}})^2}{2\bar{\omega}_\gamma(\mathbf{k})[\frac{4}{a^2}\sin(\frac{a}{2}p_0 - \frac{ia}{2}\hat{\omega}_\gamma(\mathbf{k}))^2 + \omega(\widehat{\mathbf{p}-\mathbf{k}})^2]} \\ &- \frac{\frac{4}{a^2}\sin[\frac{a}{2}p_0 - \frac{ia}{2}\hat{\omega}(\mathbf{p}-\mathbf{k})]^2 + (\widehat{2\mathbf{p}-\mathbf{k}})^2}{2\bar{\omega}(\mathbf{p}-\mathbf{k})[\frac{4}{a^2}\sin(\frac{a}{2}p_0 + \frac{ia}{2}\hat{\omega}(\mathbf{p}-\mathbf{k}))^2 + |\hat{\mathbf{k}}|^2]} \Bigg\},\end{aligned} \tag{7.54}$$

where, similar to Eq. (7.47), we have defined $\bar{\omega}_\gamma(\mathbf{k}) = a^{-1}\sinh[a\hat{\omega}_\gamma(\mathbf{k})]$. The last two terms in this expression have poles at $p_0 = \pm i\hat{\omega}_{\phi\gamma}(\mathbf{p},\mathbf{k})$, which are the source of the excited-state contributions to the scalar 2-point function in Eq. (7.46). The second term also has a pole at $p_0 = i[\hat{\omega}_\gamma(\mathbf{k}) - \hat{\omega}(\mathbf{p}-\mathbf{k})]$, and the third term has a pole at $p_0 = -i[\hat{\omega}_\gamma(\mathbf{k}) - \hat{\omega}(\mathbf{p}-\mathbf{k})]$, but taking the residues of these poles we find that they cancel each other, so the poles at $p_0 = \pm i\hat{\omega}_{\phi\gamma}(\mathbf{p},\mathbf{k})$ are the only singularities of the total expression.

Substituting Eq. (7.54) into Eq. (7.44), $C_1(t,\mathbf{p})$ can be separated into a contribution $C_{1,\Sigma}(t,\mathbf{p})$ from the double pole at $p_0 = i\hat{\omega}(\mathbf{p})$ and a contribution $C_{1,\gamma}(t,\mathbf{p})$ from the single poles at $p_0 = i\hat{\omega}_{\phi\gamma}(\mathbf{p},\mathbf{k})$:

$$C_1(t,\mathbf{p}) = C_{1,\Sigma}(t,\mathbf{p}) + C_{1,\gamma}(t,\mathbf{p}), \tag{7.55}$$

$$C_{1,\Sigma}(t,\mathbf{p}) = \frac{e^{-\hat{\omega}(\mathbf{p})|t|}}{4\bar{\omega}(\mathbf{p})^3}\left[\left(1+\frac{a^2}{2}\omega(\hat{\mathbf{p}})^2 + \bar{\omega}(\mathbf{p})\,|t|\right)\Sigma(p_{\text{o.s.}}) - i\bar{\omega}(\mathbf{p})\left.\frac{\partial\Sigma(p)}{\partial p_0}\right|_{p_{\text{o.s.}}}\right], \tag{7.56}$$

$$C_{1,\gamma}(t,\mathbf{p}) = \frac{q^2}{L^3}\sum_{\mathbf{k}\in\tilde{\mathbf{\Lambda}}}{}' A(\mathbf{p},\mathbf{k})e^{-\hat{\omega}_{\phi\gamma}(\mathbf{p},\mathbf{k})|t|}, \tag{7.57}$$

$$A(\mathbf{p},\mathbf{k}) = \frac{\frac{4}{a^2}\sinh\left[a\hat{\omega}(\mathbf{p}-\mathbf{k}) + \frac{a}{2}\hat{\omega}_\gamma(\mathbf{k})\right]^2 - \left(\widehat{2\mathbf{p}-\mathbf{k}}\right)^2}{4\bar{\omega}(\mathbf{p}-\mathbf{k})\bar{\omega}_\gamma(\mathbf{k})\left\{\frac{4}{a^2}\sinh\left[\frac{a}{2}\omega_\gamma(\mathbf{p},\mathbf{k})\right]^2 - \omega(\hat{\mathbf{p}})^2\right\}^2}. \tag{7.58}$$

Subtracting $C_{1,\gamma}(t,\mathbf{p})$ from $C_1(t,\mathbf{p})$ calculated from lattice simulations, before constructing $\Sigma_{\text{eff.}}(t,\mathbf{p})$, results in an effective self energy with a plateau at the on-shell self energy and no excited-state contamination.

7.2.3 Infinite-volume self energy

The methods in Sec. 7.2.2 can be used to numerically calculate the scalar self energy in a finite volume, using lattice scalar QED simulation data. The results in Sec. 7.2.1 give the difference between the finite-volume and infinite-volume self energy. In order to compare the analytical expressions with numerical data, the infinite-volume lattice scalar self energy is also required.

In infinite volume, the sum $\frac{1}{L^3}\sum'_{\mathbf{k}\in\tilde{\mathbf{\Lambda}}}$ in Eq. (7.54) becomes $\int_{-\pi/a}^{\pi/a}\frac{d^3\mathbf{k}}{(2\pi)^3}$. At the on-shell point $p_0 = i\hat{\omega}(\mathbf{p})$, this integral can be evaluated numerically using a package such as Mathematica [202].

It may seem sensible to calculate the infinite-volume self energy by putting p on-shell in Eq. (7.53) and numerically evaluating the four-dimensional integral, since the integrand of Eq. (7.53) is a little simpler than that of Eq. (7.54). However, there is a subtle reason that this approach would be incorrect. The on-shell condition is imposed by taking the integral over p_0 in Eq. (7.44), and before taking this integral p_0 is real in the integrand. The poles of the integrand in Eq. (7.53) at $k_0 = p_0 \pm i\hat{\omega}(\mathbf{p}-\mathbf{k})$ lie on opposite sides of the real axis when p_0 is real, but at the on-shell point $p_0 = i\hat{\omega}(\mathbf{p})$ both poles will lie in the upper half-plane when $|\mathbf{p}-\mathbf{k}| < |\mathbf{p}|$, and will both contribute to the contour integral over k_0. The correct procedure is therefore to take the k_0 integral assuming real p_0, before imposing the on-shell condition and evaluating the spatial integral in Eq. (7.54).

7.2.4 Comparison with analytical expressions

The strategy presented in the previous sections was implemented using the Grid library [201] to compute the time-momentum representation of the charged scalar 2-point function. The scalar self energy has been calculated numerically from the 2-point function, and its volume dependence has been compared with the analytical expressions in Eqs. (7.30) and (7.34). This comparison offers a valuable cross-check of the analytical calculation, and also of the lattice implementation.

7.2.4.1 Simulation setup

We calculated the 2-point function for a scalar field with bare mass $am = 0.2$ on 12 ensembles of 10000 QED_L gauge configurations with 12 different spatial volumes $12 \leq L/a \leq 128$ and temporal extent $T/a = 128$ or $T/a = 256$, and one ensemble of 3006 QED_L gauge configurations with volume $192^3 \times 256$.

7.2.4.2 Numerical extraction of the on-shell self-energy

It was found to be essential to subtract excited-state contributions from the $C_1(t,\mathbf{p})$ correlator in order to extract the on shell self-energy from a fit to the plateau region of the effective self energy defined in Eq. (7.48). For volumes $L/a \leq 64$, all $(L/a)^3 - 1$ excited states were calculated analytically and subtracted. For larger volumes, to avoid calculation of large numbers of excited

$\frac{L}{a}$	$\frac{L}{2\pi}\mathbf{p}$	$\mathbf{n}^2_{\max}$	$N_{\text{sub.}}$
≤ 64			$\left(\frac{L}{a}\right)^3 - 1$
80	(0,0,0)	128	6042
96	(0,0,0)	256	17076
96	(3,0,0)	256	17076
96	(3,3,0)	256	17076
96	(3,3,3)	512	48500
128	(0,0,0)	256	17076
128	(2,0,0)	512	48500
128	(2,2,0)	512	48500
128	(2,2,2)	512	48500
128	(4,0,0)	512	48500
128	(4,4,0)	512	48500
128	(4,4,4)	512	48500
192	(0,0,0)	512	48500
192	(3,0,0)	512	48500
192	(3,3,0)	1024	137064
192	(3,3,3)	1024	137064
192	(6,0,0)	1024	137064
192	(6,6,0)	1024	137064
192	(6,6,6)	1024	137064

TABLE 7.2: Number of excited states $N_{\text{sub.}}$ subtracted from each scalar 2-point function. When applied, the cutoff imposed on the photon modes $\mathbf{n}^2_{\max} = \frac{L}{2\pi}\mathbf{k}^2_{\max}$ is given.

states, excited states from all poles with $|\mathbf{k}|^2 \leq \mathbf{k}^2_{\max}$ were subtracted. The threshold $\mathbf{k}^2_{\max}$ was chosen so that halving $\mathbf{k}^2_{\max}$ would change $\Sigma_{\text{eff.}}(t_{\min})$ by less than one tenth of the statistical uncertainty, where $t_{\min}$ is the lower limit of the fit interval. Table 7.2 lists the number of excited states subtracted from each scalar 2-point function.

As an illustration, Fig. 7.3 represents results for the effective self energy with various excited state subtractions. The importance of subtracting excited-state contributions is evident: the effective self energy still shows significant contamination from excited states at times $t/a > 20$ where it may appear that a plateau has been reached. As seen in Table 7.2, the number of excited states which must be subtracted is several orders of magnitude larger than could be achieved through a multi-exponential fit in cases where an analytical calculation is not possible.

The statistical uncertainty in the effective self energy grows exponentially at large times, as can be seen in Fig. 7.3. This exponential degradation of the signal-to-noise (StN) ratio is worse at larger spatial momentum, and for sufficiently large momentum this problem prevents reliable plateau fits.

After subtracting the excited-state contributions, the values of the on-shell self energy were extracted through a correlated fit to the plateau region of the effective self energy. Fit intervals are given for each volume and spatial momentum in Table 7.3. In addition to the statistical uncertainty from the ensemble average, there is a systematic uncertainty arising from the choice of fit interval. This systematic uncertainty was estimated by fitting to all sub-intervals $\left[t'_{\min}, t'_{\max}\right]$ within the full fit interval $[t_{\min}, t_{\max}]$ with $t'_{\max} - t'_{\min} \geq 3$, and taking the standard deviation of central values from all sub-interval fits with p-value ≥ 0.05. This systematic uncertainty has been combined in quadrature with the statistical uncertainty in the results presented later in this section.

$\frac{L}{a}$	$\frac{L}{2\pi}\mathbf{p}$	$t_{\min}$	$t_{\max}$
12	(0,0,0)	3	57
16	(0,0,0)	3	57
20	(0,0,0)	3	60
24	(0,0,0)	3	62
32	(0,0,0)	3	61
32	(1,0,0)	3	29
32	(1,1,0)	3	17
32	(1,1,1)	3	10
40	(0,0,0)	3	58
48	(0,0,0)	3	58
56	(0,0,0)	3	61
64	(0,0,0)	3	48
64	(1,0,0)	3	48
64	(1,1,0)	3	48
64	(1,1,1)	3	40
64	(2,0,0)	3	26
64	(2,2,0)	3	26
64	(2,2,2)	3	14
80	(0,0,0)	3	53

$\frac{L}{a}$	$\frac{L}{2\pi}\mathbf{p}$	$t_{\min}$	$t_{\max}$
96	(0,0,0)	3	59
96	(3,0,0)	3	34
96	(3,3,0)	3	19
96	(3,3,3)	3	9
128	(0,0,0)	3	107
128	(2,0,0)	3	102
128	(2,2,0)	3	29
128	(2,2,2)	3	28
128	(4,0,0)	3	31
128	(4,4,0)	3	19
128	(4,4,4)	3	13
192	(0,0,0)	3	110
192	(3,0,0)	3	94
192	(3,3,0)	3	57
192	(3,3,3)	3	31
192	(6,0,0)	3	11
192	(6,6,0)	3	11
192	(6,6,6)	3	10

TABLE 7.3: Time intervals used for fits to effective on-shell self energies.

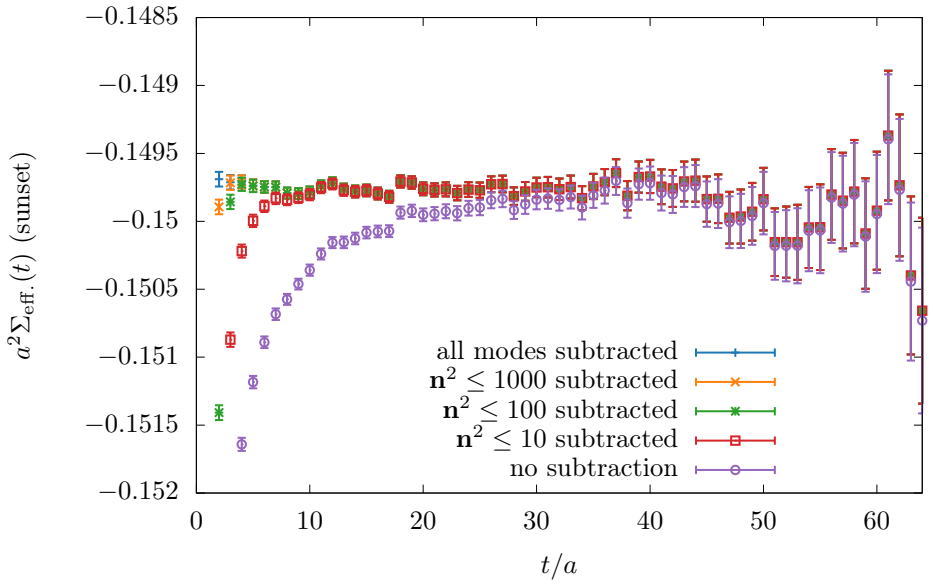

FIGURE 7.3: Sunset diagram (third diagram in Fig. 7.1) contribution to the effective scalar self energy Eq. (7.48) with various excited-state subtractions. The chosen volume here is $64^3 \times 128$ and the momentum is $\mathbf{p} = \frac{2\pi}{32a}(1,0,0)$. The various subtractions are done using the spectral representation in Eq. (7.57) and a cutoff on the integer modes $\mathbf{n} = \frac{L}{2\pi}\mathbf{k}$.

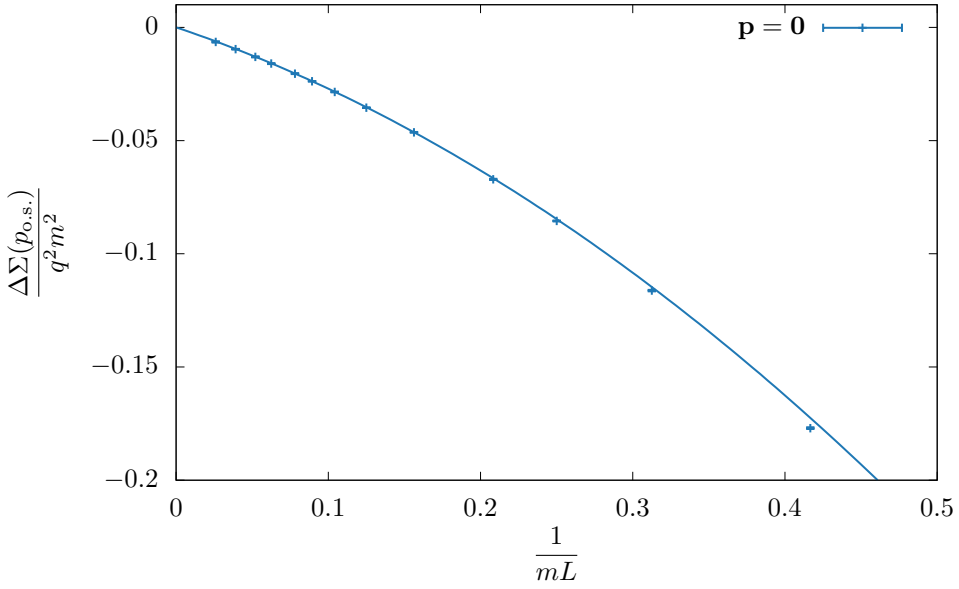

FIGURE 7.4: Volume scaling of the scalar on-shell self energy in the rest frame. The points come from the lattice scalar QED$_L$ simulations described in Sec. 7.1 and the line is the analytical prediction Eq. (7.30).

7.2.4.3 Finite-volume scaling

In this section, the results of our scalar QED simulations are compared against the analytical finite-volume effects in Sec. 7.2.1. Specifically, the scalar self energy on the lattice was computed for several different spatial volumes at fixed physical momenta. The infinite volume self energy, calculated in lattice perturbation theory, was subtracted from the lattice results and compared with the analytical effects given in Eqs. (7.30) and (7.34).

For on-shell momenta, the volume scaling is shown for the rest frame in Fig. 7.4, and for a selection of moving frames in Fig. 7.5. The agreement between the lattice results and analytical effects is good, except for small discrepancies at smaller volumes, which are of $\mathcal{O}\left(e^{-mL}\right)$ and can therefore be attributed to exponential effects neglected in the analytical calculation. For $\mathbf{p} = \frac{2\pi}{16a}(1,0,0)$ or larger, the poor StN ratio does not allow a reliable extraction of the on-shell self energy. The volume scaling for a selection of off-shell momenta is shown in Fig. 7.6. Again, good agreement is found between numerical and analytical calculations up to exponential corrections.

7.2.5 Infrared improvement

QED$_L$ is a minimal choice to implement QED in a finite volume in which photon zero-mode singularities are regulated by introducing a particular form of non-locality in space while preserving locality in time. One could make a non-minimal choice by modifying a subset of non-zero spatial momentum modes in addition to the zero mode, leading to a different approach to the infinite-volume limit. A method of "infrared improvement" is introduced in [7], to remove or suppress FV effects by tuning such extra non-localities. In this section, lattice scalar QED is used as a testbed to implement this infrared improvement method. FV effects on the rest-frame scalar

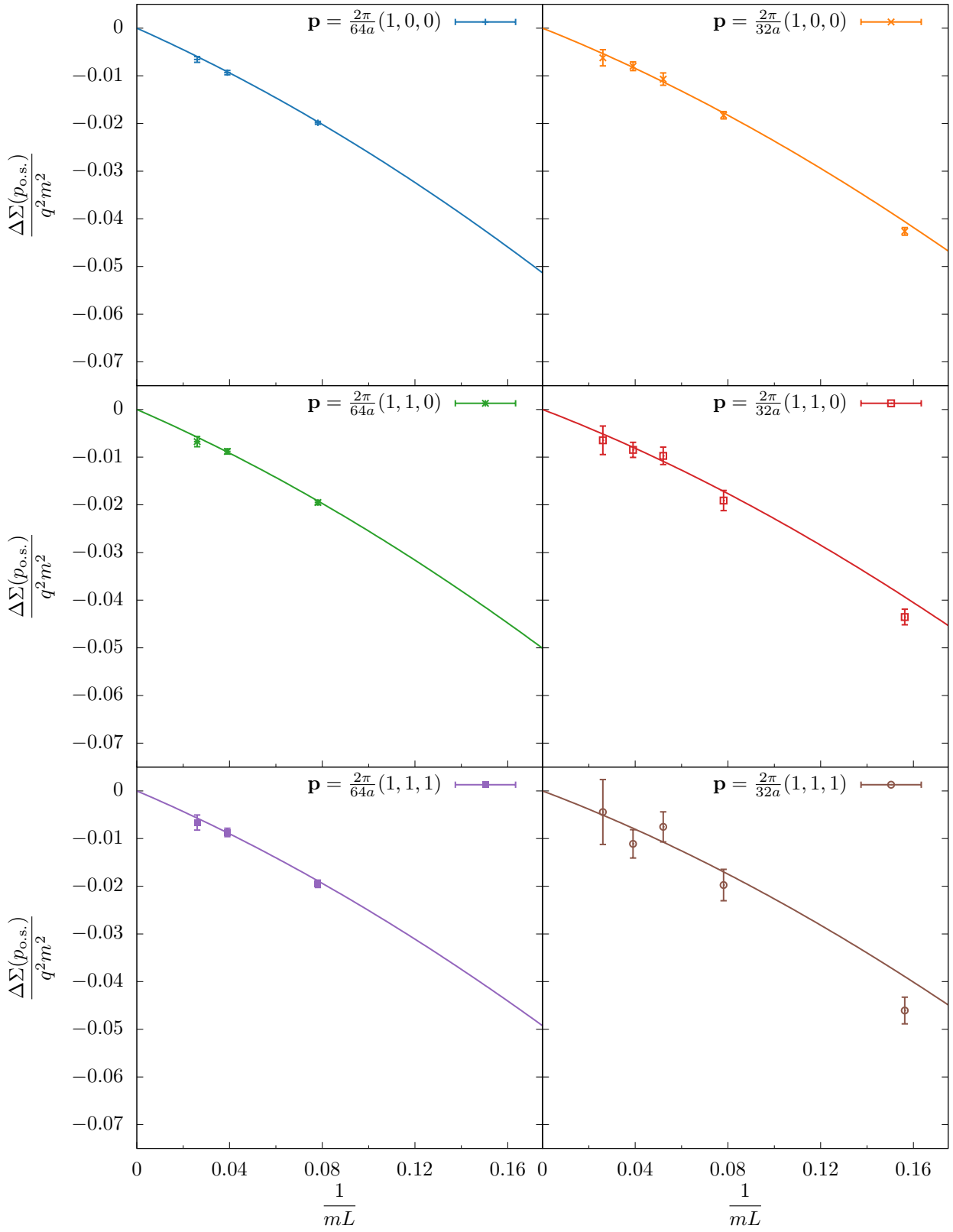

FIGURE 7.5: Volume scaling of the scalar on-shell self energy for momenta of various directions and magnitudes. Other details are identical to Fig. 7.4.

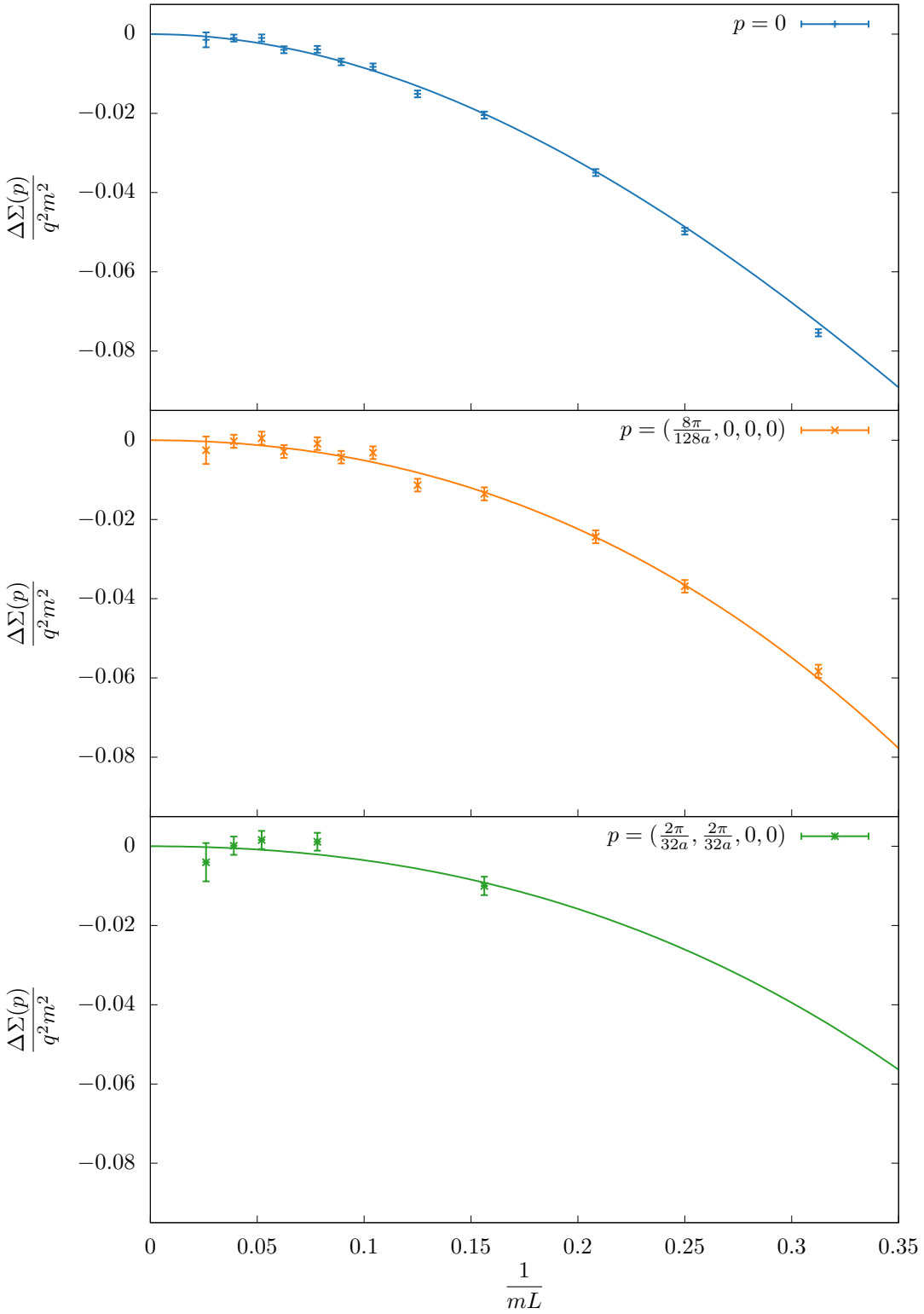

FIGURE 7.6: Volume scaling of the scalar self energy for off-shell momenta with various orientations. The points come from the lattice scalar QED$_L$ simulations described in Sec. 7.1 and the dashed line is the analytical prediction Eq. (7.34).

self energy are calculated in several infrared-improved schemes, and compared with analytical predictions.

In principle, knowledge of the analytic form of leading QED_L FV effects is sufficient to subtract them from quantities calculated in finite volume, in order to obtain the infinite-volume values. As such, an improved numerical scheme in which FV effects are suppressed seems unnecessary. However, if the FV effects are large then the computational resources required to accurately perform the required subtraction will be significant, prohibiting precision calculations of some quantities in QED_L. In addition, in studies of systems with multiple charged hadrons, such as scattering processes, the FV corrections to the masses of incoming and outgoing particles can affect subsequent calculations. An infrared-improved scheme in which the hadrons are already close to their infinite-volume mass could simplify these subsequent calculations.

The method introduced in [7] is to replace the QED_L gauge action in Eq. (5.12) by an "infrared-improved" action

$$S_{\gamma,w}\left[\tilde{A}\right] = \frac{1}{2V}\sum_{k_0}\sum_{\mathbf{k}}{}' \frac{\hat{k}^2}{1+w_{|\mathbf{n}|^2}}\sum_{\mu}\left|\tilde{A}_\mu\left(k\right)\right|^2 , \tag{7.59}$$

where $\mathbf{n} = \frac{L}{2\pi}\mathbf{k}$ and the $w_{|\mathbf{n}|^2}$ are real coefficients which are non-zero only for a finite number of values of $|\mathbf{n}|$. Because of this property, the contributions from the $w_{|\mathbf{n}|^2}$ vanish in the infinite-volume limit. The additional constraint $w_{|\mathbf{n}|^2} > -1$ is required to preserve the positivity of the action. Using this improved action, FV effects such as those described by Eqs. (7.30) and (7.34) keep the same form, but with the $c_{j,k}(\mathbf{v})$ coefficients replaced by

$$c^{(w)}_{j,k}(\mathbf{v}) = c_{j,k}(\mathbf{v}) + \sum_{\mathbf{n}}{}' \frac{w_{|\mathbf{n}|^2}}{|\mathbf{n}|^j\left(1-\mathbf{v}\cdot\hat{\mathbf{n}}\right)^k}, \quad c^{(w)}_j = c^{(w)}_{j,k}(\mathbf{0}) . \tag{7.60}$$

Consider the on-shell self energy in the rest frame ($\mathbf{v} = \mathbf{0}$). We can see from Eq. (7.30) that the $\mathcal{O}\left(1/L\right)$ FV effects will be completely removed in an infrared-improved scheme where $c^{(w)}_2 = 0$. With the minimal choice $w_N = 0$ for all $N > 1$, Eq. (7.60) can be solved to find

$$w_1 = -\frac{1}{6}c_2 = -\frac{\pi}{6}c_1 , \tag{7.61}$$

which modifies the $\mathcal{O}\left(1/L^2\right)$ coefficient to become $c^{(w)}_1 = (1-\pi)c_1$.

By additionally allowing w_2 to be non-zero, we can try to remove the $\mathcal{O}\left(1/L\right)$ and $\mathcal{O}\left(1/L^2\right)$ corrections by solving Eq. (7.60) for $c^{(w)}_1 = c^{(w)}_2 = 0$. This results in the linear system

$$c_2 + 6w_1 + 6w_2 = 0 , \tag{7.62}$$

$$c_1 + 6w_1 + 6\sqrt{2}w_2 = 0 , \tag{7.63}$$

which gives

Improvement	w_1	w_2	$c_2^{(w)}$	$c_1^{(w)}$
None	0	0	-8.91363292	-2.83729748
$\mathcal{O}\left(\frac{1}{L}\right)$	1.48560549	0	0	6.07633544
cumulative $\mathcal{O}\left(\frac{1}{L^2}\right)$	0.86681632	0	-3.71273496	2.36360048
cumulative $\mathcal{O}\left(\frac{1}{L^2}\right) + \mathcal{O}\left(\frac{1}{L^3}\right)$	2.04145881	-0.93739607	-2.28925650	1.45738594

TABLE 7.4: Summary of improvement weight factors and FV coefficients according to the improvement prescriptions for the mass of charged hadrons described in Sec. 7.2.5. Values from cumulative improvement prescriptions are given for the reference scale $\mu_0 = mL_0 = 4$.

$$w_1 = -\frac{1}{6}\left(1+\sqrt{2}\right)\left(\sqrt{2}\pi - 1\right)c_1\,, \tag{7.64}$$

$$w_2 = \frac{1}{6}\left(1+\sqrt{2}\right)(\pi - 1)\,c_1\,. \tag{7.65}$$

Evaluating this, we find $w_2 = -2.44492857\ldots$, which violates the condition $w_N > -1$ required for positivity of the action. It is therefore not possible to simultaneously remove the $\mathcal{O}(1/L)$ and $\mathcal{O}\left(1/L^2\right)$ FV effects for all volumes using this method.

We could instead try to cancel the sum of $\mathcal{O}(1/L)$ and $\mathcal{O}\left(1/L^2\right)$ effects for a reference volume $\mu_0 = mL_0$, by solving for the condition

$$\frac{c_2^{(w)}}{4\pi^2\mu_0} + \frac{c_1^{(w)}}{2\pi\mu_0^2} = 0\,. \tag{7.66}$$

Using a single weight w_1, Eq. (7.66) is satisfied by

$$w_1 = -\frac{\pi}{6}\frac{2+\mu_0}{2\pi+\mu_0}c_1\,. \tag{7.67}$$

Using two weights w_1 and w_2, Eq. (7.66) can be simultaneously satisfied along with the suppression of FV effects up to $\mathcal{O}\left(1/L^3\right)$ for the self energy of a spin-$\frac{1}{2}$ particle (calculated in [7]) by the choice

$$w_1 = \frac{1}{6}\frac{2\sqrt{2}\pi + \mu_0 + 4\pi c_1 + 2\pi\mu_0 c_1}{2\sqrt{2}\pi - 4\pi - \mu_0}\,, \tag{7.68}$$

$$w_2 = -\frac{1}{6}\frac{2\pi + \mu_0 + 2\pi c_1 + \pi\mu_0 c_1}{2\sqrt{2}\pi - 4\pi - \mu_0}\,. \tag{7.69}$$

The three choices of weights introduced here are summarised in Table 7.4, for reference volume $\mu_0 = 4$.

Infrared improvement is implemented in our numerical setup by generating photon fields using the same procedure as for QED$_L$, with $\tilde{A}_\mu(k)$ for modified modes drawn from a Gaussian distribution with variance $\frac{2V}{\hat{k}^2}\left(1 + w_{|\mathbf{n}|^2}\right)$. Improved gauge ensembles of 100 configurations have been generated for each choice of improvement weights in Table 7.4, for 5 volumes. The rest-frame self energy (mass-squared) FV effect calculated on each of these ensembles is plotted in Fig. 7.7, along with the analytical predictions from Eq. (7.30) with the improved coefficients in Table 7.4.

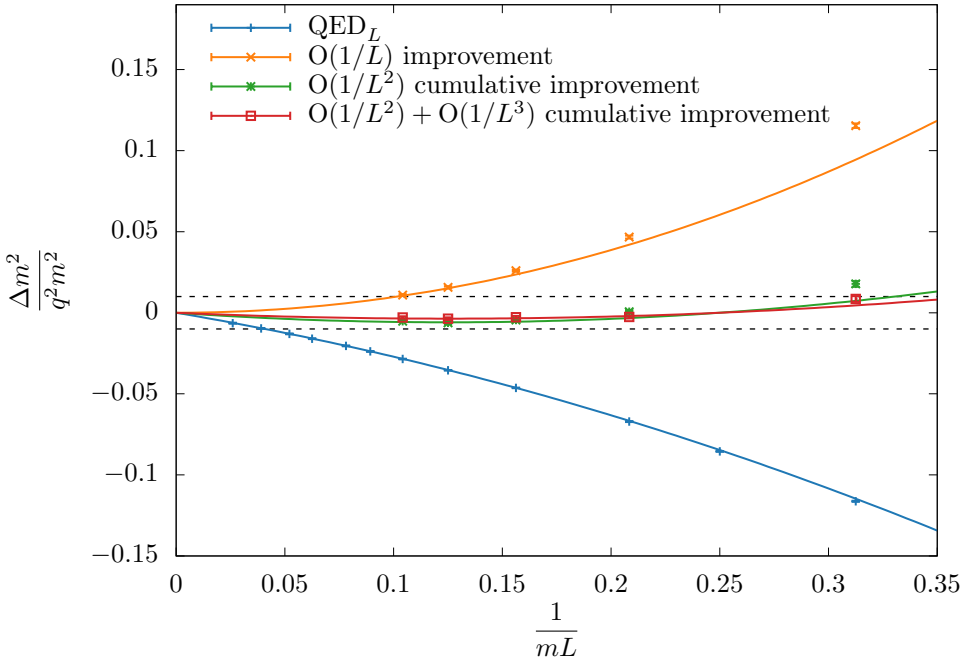

FIGURE 7.7: FV contributions to the mass-squared of a scalar particle in QED$_L$, and the improved versions described in Sec. 7.2.5. The points correspond to lattice scalar QED simulations, with photon actions improved using the method described in Sec. 7.2.5. The lines are the analytical predictions in Eq. (7.30), with the improved coefficients given in Table 7.4. The dashed lines indicate the regions within which the FV contributions are below 1% relative to the electromagnetic corrections to the mass.

Although the $\mathcal{O}(1/L)$ FV effects can be removed exactly for all volumes, the $\mathcal{O}\left(1/L^2\right)$ effects are magnified in the resulting improved scheme. The total FV effects in the $\mathcal{O}(1/L)$ improved scheme are larger than those in QED$_L$ for $mL \sim 4$, as can be seen in Fig. 7.7, and this improvement choice is therefore of limited use in lattice calculations. The cumulative $\mathcal{O}\left(1/L^2\right)$ and $\mathcal{O}\left(1/L^2\right) + \mathcal{O}\left(1/L^3\right)$ prescriptions, in contrast, suppress the relative mass-squared FV corrections to sub-percent level for volumes $mL \geq 4$, which would be comparable to or smaller than other systematics in most state-of-the-art numerical calculations.

To check that the infrared improvement method has been implemented correctly in numerical calculations, the difference between the self energy in improved and unimproved schemes can be calculated analytically. From the infrared-improved action Eq. (7.59), the photon propagator is

$$D_{\mu\nu}^{(w)}(k) = \frac{1 + \omega_{|\mathbf{n}|^2}}{\hat{k}^2}\,, \tag{7.70}$$

and each term in the sum in Eq. (7.54) gains a factor of $\left(1 + \omega_{|\mathbf{n}|^2}\right)$. The self energy difference $\Sigma^{(w)}(p_{\text{o.s.}}) - \Sigma(p_{\text{o.s.}})$ is then given by Eq. (7.54) with each term in the sum weighted by $w_{|\mathbf{n}|^2}$. Since only a small subset of the weights are non-zero, this difference can be easily calculated. All numerical points in Fig. 7.7 have been checked and found to be in perfect agreement with this calculation, providing confidence that the numerical implementation is correct.

It appears in Fig. 7.7 that there is a discrepancy between the numerical data and the analytical prediction Eq. (7.30) at smaller volumes in the improved cases, while the agreement is better in the QED$_L$ calculation without improvement. The magnitude of this discrepancy is consistent

with $\mathcal{O}\left(e^{-mL}\right)$ corrections which are neglected in the analytical calculation, so it appears that there is suppression of exponential corrections that is broken by the improvement procedure.

7.3 HVP finite volume effects

Having demonstrated the lattice scalar QED$_L$ method by calculating QED FV effects for the scalar self energy, this method can be applied to the numerical calculation of leading QED$_L$ FV effects for the HVP. In this section, HVP FV effects are calculated numerically and compared with analytical expressions derived in [8].

As introduced in Sec. 4.3, the HVP form factor is defined through the HVP tensor $\Pi_{\mu\nu}(Q) = a^4 \sum_{x\in\Lambda} C_{\mu\nu}(x) \left[e^{-iQ\cdot x} - 1\right]$, where

$$C_{\mu\nu}(x) = \langle V_\mu(x) V_\nu(0)\rangle \tag{7.71}$$

is the electromagnetic current 2-point function to be calculated on the lattice. We expect the FV behaviour of the HVP to be dominated by the lowest-energy state, which is the two-pion state, so we calculate the HVP in scalar QED$_L$ using the action defined in Sec. 7.1.1.

7.3.1 Conserved vector current

Consider an infinitesimal $U(1)$ gauge transformation, of the form

$$\begin{aligned} \phi(x) &\to \phi'(x) = (1 + i\varepsilon(x))\,\phi(x)\,, \\ \phi^*(x) &\to (\phi'(x))^* = (1 - i\varepsilon(x))\,\phi^*(x)\,. \end{aligned} \tag{7.72}$$

The change to the scalar QED action Eq. (7.2) under this transformation is

$$\begin{aligned} \delta S[\phi, A] &= S\left[\phi', A\right] - S[\phi, A] \\ &= \frac{a^4}{2} \sum_x \frac{i\varepsilon(x)}{a} \sum_\mu \delta^*_\mu \left[\phi^*(x)\, e^{iqaA_\mu(x)} \phi(x + a\hat{\mu}) - \phi^*(x + a\hat{\mu})\, e^{-iqaA_\mu(x)} \phi(x)\right]. \end{aligned} \tag{7.73}$$

The vector Ward identity $\langle \delta S\rangle = 0$ is satisfied by the condition

$$\sum_\mu \delta^*_\mu V_\mu(x) = 0\,, \tag{7.74}$$

with the conserved current

$$V_\mu(x) = \frac{i}{a}\left[\phi^*(x)\, e^{iqaA_\mu(x)} \phi(x + a\hat{\mu}) - \phi^*(x + a\hat{\mu})\, e^{-iqaA_\mu(x)} \phi(x)\right]. \tag{7.75}$$

7.3.2 Contact term

The conserved vector current in Eq. (7.75) is a non-local operator, containing a gauge link. A contact term therefore arises in the conserved vector two-point function when the conserved vector currents at the source and sink coincide. This contact term is derived using the Ward identity

$$\langle \delta V_\mu (x) \rangle - \langle V_\mu (x) \, \delta S \rangle = 0 \, . \tag{7.76}$$

Under the transformation in Eq. (7.72), the change in the conserved vector current is

$$\delta V_\mu (x) = -i\varepsilon (x) \, \delta^*_\mu \left[\phi^* (x) \, e^{iqaA_\mu (x)} \phi (x + a\hat{\mu}) + \phi^* (x + a\hat{\mu}) \, e^{-iqaA_\mu (x)} \phi (x) \right] , \tag{7.77}$$

and

$$V_\mu (x) \, \delta S = \frac{a^4}{2} \sum_y \frac{i\varepsilon (y)}{a} V_\mu (x) \sum_\nu \delta^*_\nu V_\nu (y) \, . \tag{7.78}$$

Combining Eqs. (7.76)–(7.78) gives

$$\sum_\nu \delta^*_\nu \left[\frac{i}{a} \langle V_\mu (x) \, V_\nu (y) \rangle + 2i\delta (x - y) \, \delta_{\mu\nu} \langle T_\mu (x) \rangle \right] = 0 \, , \tag{7.79}$$

where

$$T_\mu (x) = \phi^* (x) \, e^{iqaA_\mu (x)} \phi (x + a\hat{\mu}) + \phi^* (x + a\hat{\mu}) \, e^{-iqaA_\mu (x)} \phi (x) \, . \tag{7.80}$$

The transversality of the HVP is therefore recovered by deriving it from the correlation function

$$C_{\mu\nu} (x) = \langle V_\mu (x) \, V_\nu (0) \rangle + 2\delta (x) \, \delta_{\mu\nu} \langle T_\mu (x) \rangle \, , \tag{7.81}$$

where the second term on the right-hand side is the contact term.

However, it is not necessary to calculate this contact term in the lattice simulation. Due to the delta function of position, the contact-term contribution to the HVP tensor $\Pi_{\mu\nu} (q)$ has no momentum dependence, and this contribution is removed when the zero-mode of $\Pi_{\mu\nu}$ is subtracted as in Eq. (4.25). It is therefore sufficient to construct the HVP tensor from the correlation function defined in Eq. (7.71).

7.3.3 Conserved vector two-point function

Using the conserved vector current defined in Eq. (7.75), the electromagnetic vector two-point function is

$$\begin{aligned} C_{\mu\nu}(x) \equiv \langle V_\mu(x) V_\nu(0)\rangle = \frac{1}{a^2}\big[&\langle \phi^*(x) U_\mu(x) \phi(x+a\hat{\mu}) \phi^*(a\hat{\nu}) U_\nu^\dagger(0) \phi(0)\rangle \\ &- \langle \phi^*(x+a\hat{\mu}) U_\mu^\dagger(x) \phi(x) \phi^*(a\hat{\nu}) U_\nu^\dagger(0) \phi(0)\rangle \\ &- \langle \phi^*(x) U_\mu(x) \phi(x+a\hat{\mu}) \phi^*(0) U_\nu(0) \phi(a\hat{\nu})\rangle \\ &+ \langle \phi^*(x+a\hat{\mu}) U_\mu^\dagger(x) \phi(x) \phi^*(0) U_\nu(0) \phi(a\hat{\nu})\rangle\big] \\ = \frac{2}{a^2}\Re\big[&\langle \phi^*(x) U_\mu(x) \phi(x+a\hat{\mu}) \phi^*(a\hat{\nu}) U_\nu^\dagger(0) \phi(0)\rangle \\ &- \langle \phi^*(x+a\hat{\mu}) U_\mu^\dagger(x) \phi(x) \phi^*(a\hat{\nu}) U_\nu^\dagger(0) \phi(0)\rangle\big], \end{aligned} \tag{7.82}$$

where the angle brackets denote the expectation value over both scalar and gauge fields. Denoting the expectation values over scalar fields and gauge fields respectively with the subscripts ϕ and γ, and denoting the scalar propagator as $G(x \mid y) \equiv \langle \phi^*(x)\phi(y)\rangle_\phi$, we can use Wick contractions to write Eq. (7.82) as

$$\begin{aligned} C_{\mu\nu}(x) = \big\langle 2\Re\big[&G^\dagger(0 \mid x) U_\mu(x) G(a\hat{\nu} \mid x+a\hat{\mu}) U_\nu^\dagger(0) - G^\dagger(0 \mid x+a\hat{\mu}) U_\mu^\dagger(x) G(a\hat{\nu} \mid x) U_\nu^\dagger(0)\big]\big\rangle_\gamma \\ &+ \text{ disconnected terms}, \end{aligned} \tag{7.83}$$

The "disconnected terms" are all contributions which contain more than one scalar loop. However, at $\mathcal{O}(\alpha)$ the only non-zero disconnected term is

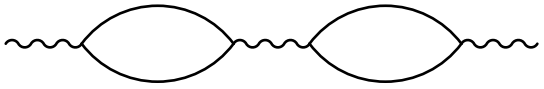

which is one-particle reducible to two tree-level HVP diagrams, and therefore no disconnected diagrams need to be included in our calculation.

The scalar propagators in Eq. (7.83) can be rewritten in terms of Dirac deltas and the inverse of the Δ operator defined in Eq. (7.6):

$$\begin{aligned} C_{\mu\nu}(x) = \big\langle 2\Re\big[&\left(\Delta^{-1}\delta(x)\right)^\dagger U_\mu(x) \left(\tau_\mu \Delta^{-1}\delta(x-a\hat{\nu})\right) U_\nu^\dagger(0) \\ &- \left(\tau_\mu \Delta^{-1}\delta(x)\right)^\dagger U_\mu^\dagger(x) \left(\Delta^{-1}\delta(x-a\hat{\nu})\right) U_\nu^\dagger(0)\big]\big\rangle_\gamma . \end{aligned} \tag{7.84}$$

Calculation of all components of $C_{\mu\nu}(x)$ therefore requires five point-to-all scalar propagators, from point sources at $x = 0$ and $x = a\hat{\nu}$, which can be calculated up to $\mathcal{O}\left(q^2\right)$ using the method described in Sec. 7.1.2.

The gauge links $U_\mu(x)$ which appear in the conserved vector current at the source and sink can also be expanded in powers of the charge q:

$$U_\mu(x) = 1 + iqaA_\mu(x) - \frac{1}{2}q^2a^2A_\mu^2(x) + \mathcal{O}\left(q^3\right). \tag{7.85}$$

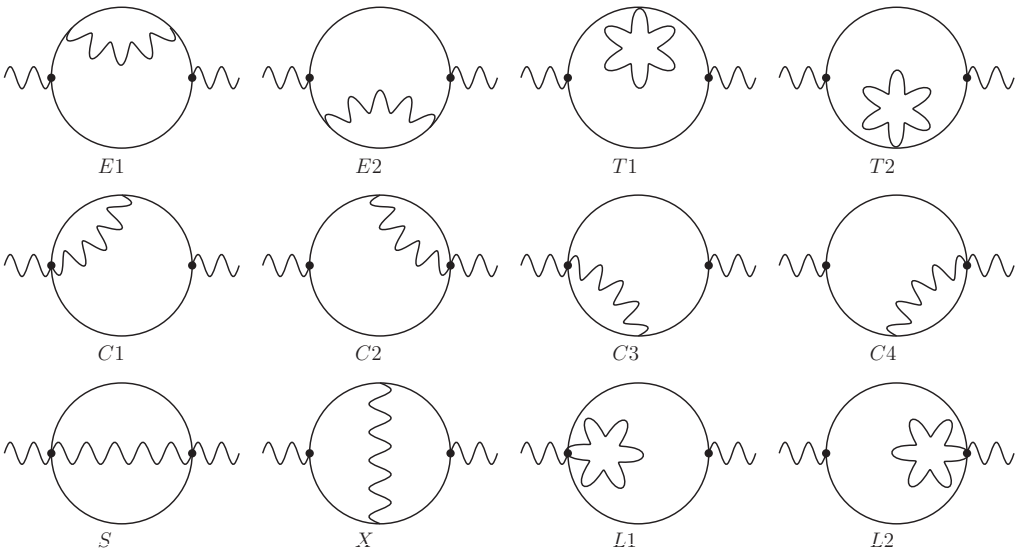

FIGURE 7.8: The twelve NLO diagrams which contribute to the HVP in lattice scalar QED. Dots represent the conserved vector current coupling to external photons.

There are twelve $\mathcal{O}(\alpha)$ terms in the expansion of Eq. (7.84), which are shown in Fig. 7.8. Seeing that some of these diagrams are equal up to relabelling of momenta in the loops, we are left with six topologically distinct diagrams, which we call the embedded sunrise (E), contact (C), embedded tadpole (T), sunset (S), photon exchange (X) and lattice-only (L) diagrams. The L diagrams are an artifact of the non-locality of the conserved current, and vanish in the continuum limit.

7.3.4 Reducing the computational cost

The bulk of the computation time required to calculate $C_{\mu\nu}$ comes from the scalar propagator inversions. As stated earlier, the calculation requires 5 scalar propagators, with each term involving the contraction of a propagator from $x = 0$ with a propagator from $x = a\hat{\nu}$. However, at next-to-leading order (NLO) we require the $\mathcal{O}(q^2)$ contributions to at most one of the two propagators in any given diagram. Making use of translation invariance, we can always choose this to be the propagator from $x = 0$. We therefore only need to compute the four propagators from sources at $x = a\hat{\nu}$ to $\mathcal{O}(q)$ (note that the construction of diagram X requires the $\mathcal{O}(q)$ contributions to all 5 scalar propagators). The calculation of a scalar propagator up to $\mathcal{O}(q)$ requires 12 FFTs, compared with 32 FFTs for a propagator at $\mathcal{O}(q^2)$, so by computing the $\mathcal{O}(q^2)$ corrections for only one of the five propagators, the total number of FFTs required (and therefore, approximately, the total computation time) is reduced by a factor of 1/2.

7.3.5 Renormalisation

Since the finite volume corrections are an infrared effect and the renormalisation procedure deals with UV divergences, one might naïvely expect that the FV correction could be calculated with unrenormalised quantities.

This assumption appears to be valid for the scalar self energy, as seen from the results in Sec. 7.2.4 where we did not renormalise the theory. However, it turns out that this is not the case for the

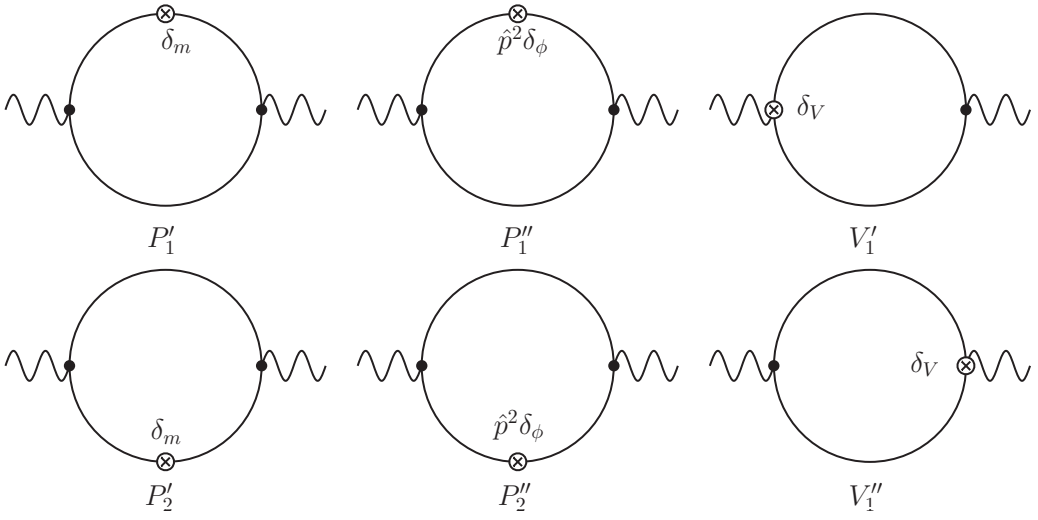

FIGURE 7.9: Additional 1-loop counterterm diagrams required to renormalise the HVP.

HVP. The interplay between UV and IR effects arises because this is a 2-loop calculation. This means that we can have contributions where the momentum passing through the photon loop can be large (UV), while the momentum passing through the other loop is small (IR). We now see that the FV corrections arising from the IR loop can be amplified by the UV-divergent part of the UV loop in the unrenormalised theory.

In scalar QED the scalar 2-point function $\Sigma(p^2)$ is quadratically divergent. It can be written as

$$\Sigma(p^2) = \underbrace{\Sigma(0)}_{\text{quadratic}} + \underbrace{p^2 \frac{d\Sigma(0)}{dp^2}}_{\text{logarithmic}} + \underbrace{\tilde{\Sigma}(p^2)}_{\text{UV finite}} . \tag{7.86}$$

We rewrite the bare quantities using the renormalised ones: $\phi_0 = \sqrt{Z_\phi}\phi$, $A_0^\mu = \sqrt{Z_A}A^\mu$, $m_0 = Z_m m$, $q_0 = Z_q q$. The counterterms present in the lattice theory are:

1. $(Z_\phi - 1)\hat{p}^2\phi^\dagger\phi \equiv \delta_\phi \hat{p}^2\phi^\dagger\phi$,
2. $(Z_\phi Z_m - 1)\phi^\dagger\phi \equiv \delta_m\phi^\dagger\phi$,
3. $(Z_q Z_\phi\sqrt{Z_A} - 1)(iq)(\widehat{p_1 + p_2})^\mu\phi^\dagger A_\mu\phi = \delta_V(iq)(\widehat{p_1 + p_2})^\mu\phi^\dagger A_\mu\phi$,
4. $-(Z_q^2 Z_\phi Z_A - 1)q^2\phi^\dagger\phi A_\mu A^\mu$,
5. $(Z_A - 1)\frac{1}{4}F_{\mu\nu}F^{\mu\nu}$.

The last counterterm does not contribute in our case. The remaining counterterm diagrams give rise to new 1-loop diagrams: momentum-independent propagator correction (P'), momentum-dependent propagator correction (P'') and vertex correction (V'). There is also a tadpole correction (T'), but it vanishes when the zero mode is subtracted. The total renormalised NLO contribution to the HVP is $2T + 2E + 2P' + 2P'' + 4C + X + 2V' + S + 2L$.

We use the following renormalisation conditions:

$$\Sigma(0) = 0\,, \tag{7.87}$$
$$\Sigma(p = p^*) = 0\,, \tag{7.88}$$
$$\Gamma^\mu(0, k = p^*) = k^\mu\,. \tag{7.89}$$

Here, Σ is the scalar two-point function and $\Gamma^\mu(p,k)$ is the amputated 3-point scalar-scalar photon function with incoming scalar with momentum p and photon with momentum k. The first condition fixes $\delta_m \equiv (Z_m Z_\phi - 1)$ while the second one fixes $\delta_\phi \equiv Z_\phi - 1$. The third condition ensures that $Z_q Z_\phi \sqrt{Z_A} = Z_\phi$ so that $Z_q = 1/\sqrt{Z_A}$ and $\delta_V = \delta_\phi$.

The renormalised scalar 2-point function can be written as

$$\Sigma(\hat{q}^2) = S(q) + T(q) + \delta_m + \hat{q}^2 \delta_\phi\,, \tag{7.90}$$

where S and T are the sunset and tadpole diagrams in Fig. 7.1, respectively, and deltas are the counterterm coefficients to be determined from renormalisation conditions. For convenience, we can choose to split $\delta_m = \delta_m^T + \delta_m^S$ and $\delta_\phi = \delta_\phi^T + \delta_\phi^S$ in such a way that the renormalisation conditions are satisfied by imposing

$$S(0) + \delta_m^S = 0\,, \tag{7.91}$$
$$T(0) + \delta_m^T = 0\,, \tag{7.92}$$
$$S(p^*) + \delta_m^S + (\hat{p}^*)^2\, \delta_\phi^S = 0\,, \tag{7.93}$$
$$T(p^*) + \delta_m^T + (\hat{p}^*)^2\, \delta_\phi^T = 0\,, \tag{7.94}$$

for a chosen reference momentum p^*. We now focus on the tadpole contribution. We can write

$$T(q) = -q^2 \int_{-\pi/a}^{\pi/a} \frac{d^4k}{(2\pi)^4} \frac{1}{\hat{k}^2} \sum_\mu \cos(p^\mu) \tag{7.95}$$
$$= -q^2 \left(4 - \frac{\hat{p}}{2}\right) z_0\,, \tag{7.96}$$

where $z_0 \equiv \int_k 1/\hat{k}^2 = 0.154933$.

Imposing the renormalisation conditions gives

$$\delta_m^T = 4q^2 z_0\,, \tag{7.97}$$
$$\delta_\phi^T = -0.5 q^2 z_0\,. \tag{7.98}$$

It can be noted that at infinite volume $T(p) + \delta_m^T + \hat{p}^2 \delta_\phi^T = 0$ for all values of p.

Similarly, the sunset counterterms can be calculated using

$$S(p) = q^2 \int_{-\pi/a}^{\pi/a} \frac{d^4k}{(2\pi)^4} \frac{\widehat{2p+k}^2}{\hat{k}^2 \left(\widehat{p+k}^2 + m^2\right)} \,. \tag{7.99}$$

Setting $am = 0.2$ and $ap^* = 2\pi/128$ gives

$$\delta_m^S = -0.152913 q^2 \,, \tag{7.100}$$
$$\delta_\phi^S = -0.068590 q^2 \,. \tag{7.101}$$

In our numerical calculation, the additional counterterm diagrams are

$$P' = 2\delta_m \Re\left[\left(\Delta_0^{-1}\delta(x)\right)^\dagger \left(\tau_\mu \Delta_0^{-1}\Delta_0^{-1}\delta(x-a\hat{\nu})\right) - \left(\tau_\mu \Delta_0^{-1}\delta(x)\right)^\dagger \left(\Delta_0^{-1}\Delta_0^{-1}\delta(x-a\hat{\nu})\right)\right] , \tag{7.102}$$

$$P'' = 2\delta_\phi \Re\left[\left(\Delta_0^{-1}\delta(x)\right)^\dagger \left(\tau_\mu \Delta_0^{-1}\mathcal{F}^{-1}\hat{p}^2\mathcal{F}\Delta_0^{-1}\delta(x-a\hat{\nu})\right) - \left(\tau_\mu \Delta_0^{-1}\delta(x)\right)^\dagger \left(\Delta_0^{-1}\mathcal{F}^{-1}\hat{p}^2\mathcal{F}\Delta_0^{-1}\delta(x-a\hat{\nu})\right)\right] ,$$

$$V' = 2\delta_\phi \Re\left[\left(\Delta_0^{-1}\delta(x)\right)^\dagger \left(\tau_\mu \Delta_0^{-1}\delta(x-a\hat{\nu})\right) - \left(\tau_\mu \Delta_0^{-1}\delta(x)\right)^\dagger \left(\Delta_0^{-1}\delta(x-a\hat{\nu})\right)\right] . \tag{7.103}$$

The cost of computing these diagrams is negligible, since they do not depend on the gauge field.

7.3.6 Analytical FV effects

The electromagnetic FV effects on the HVP have been calculated analytically in scalar QED$_L$ [8]. The leading effects for each of the diagrams E, T, C, S and X are found to be $\mathcal{O}\left(1/L^2\right)$. The analytical expressions for each of the 5 diagrams are given in appendix B. Note that these results are from a continuum calculation, so diagram L is not included.

Summing all contributions, the $\mathcal{O}\left(1/L^2\right)$ terms cancel and the leading effect is $\mathcal{O}\left(1/L^3\right)$. The total FV effect is

$$\Delta\Pi(Q^2) = \frac{c_0}{m^3L^3}\left(-\frac{16}{3}\Omega_{0,3} - \frac{5}{3}\Omega_{2,2} + \frac{40}{9}\Omega_{2,3} - \frac{3}{8}\Omega_{4,1} + \frac{7}{6}\Omega_{4,2} + \frac{8}{9}\Omega_{4,3}\right) + \mathcal{O}\left(\frac{1}{L^4}, e^{-mL}\right) , \tag{7.104}$$

where the $\Omega_{\alpha,\beta}$ are defined in appendix B. The absence of FV effects larger than $\mathcal{O}\left(1/L^3\right)$ is universal [8].

7.3.7 Comparison with analytical expressions

We have calculated the HVP form factor in scalar QED_L on lattices with time extent $T = 128$, for 8 different spatial volumes $16 \leq L \leq 64$, with bare scalar mass $am = 0.2$. We used ensembles of 40000 QED_L photon field configurations for each volume $L \leq 48$, and 10000 field configurations for $L = 56$ and $L = 64$. This calculation was implemented using the Grid library [201].

In order to compare our numerical data from lattice calculations with analytical FV expressions, a calculation of the infinite-volume HVP is also required. The analytical expressions for diagrams E, T, C, S and X, from lattice perturbation theory, are given in appendix A. For the results shown below, the infinite-volume values are obtained by numerically integrating these expressions using the `vegas` algorithm [203].

The `vegas` algorithm can also be used to numerically calculate the finite volume momentum sums over the integrands for diagrams E, T, C, S and X, providing an alternative method with which to check the lattice results. This can be achieved by using the identity

$$\sum_{p=0}^{N} f(p) = \int_0^{N+1} dp f(\lfloor p \rfloor)\,. \tag{7.105}$$

We find excellent agreement between lattice results and numerical results obtained using this method, providing confidence that the lattice calculation has been implemented correctly. The agreement between these two sets of numerical results can be seen in Figs. 7.10 – 7.13. Further numerical calculations by the authors of [8] indicate that the errors from the `vegas` calculations are underestimated, explaining the significant discrepancy between some of these points and the analytical curves.

In Figs. 7.10 – 7.12, numerical lattice results are compared with analytical expressions in appendix B for the combinations of diagrams $2E + 2P'^{(E)} + 2P''^{(E)}$, $2T + 2P'^{(T)} + 2P''^{(T)}$ and $4C + S + X + 2L + 2V'$, respectively. In Fig. 7.13 the total $\mathcal{O}(\alpha)$ HVP is compared with the analytical expression Eq. (7.104). We find that the lattice results agree with the analytical results for small $m_R L$, up to small discrepancies which we attribute to small cutoff effects which enter at the two-loop level. For larger $m_R L$ we begin to see larger discrepancies between the lattice data and the analytical expressions, particularly in Figs. 7.12 and 7.13, but these discrepancies are consistent with the size of $\mathcal{O}\left(\frac{1}{(mL)^4}, e^{-mL}\right)$ corrections which are neglected in the analytical calculations.

It is evident from Figs. 7.10 – 7.12 that the largest $\mathcal{O}(\alpha)$ contribution to the infinite-volume HVP is from diagram E. The FV effects are largest, and have opposite signs, for the E and T diagrams, while the FV effects for the combination $4C + S + X + 2L + 2V'$ are significantly smaller. The FV effect on the total $\mathcal{O}(\alpha)$ HVP is notably smaller than the effect on diagrams E and T separately, as a result of the cancellation of $\mathcal{O}\left(\frac{1}{L^2}\right)$ effects.

We can see from Fig. 7.13 that the FV effect for the total HVP is a few percent of the infinite-volume QED correction, for $m_R L \gtrsim 4$. Since the QED correction is itself an $\mathcal{O}(1\%)$ effect on the full HVP, the QED FV effects are sufficiently small to be negligible in lattice QCD+QED calculations at the current precision.

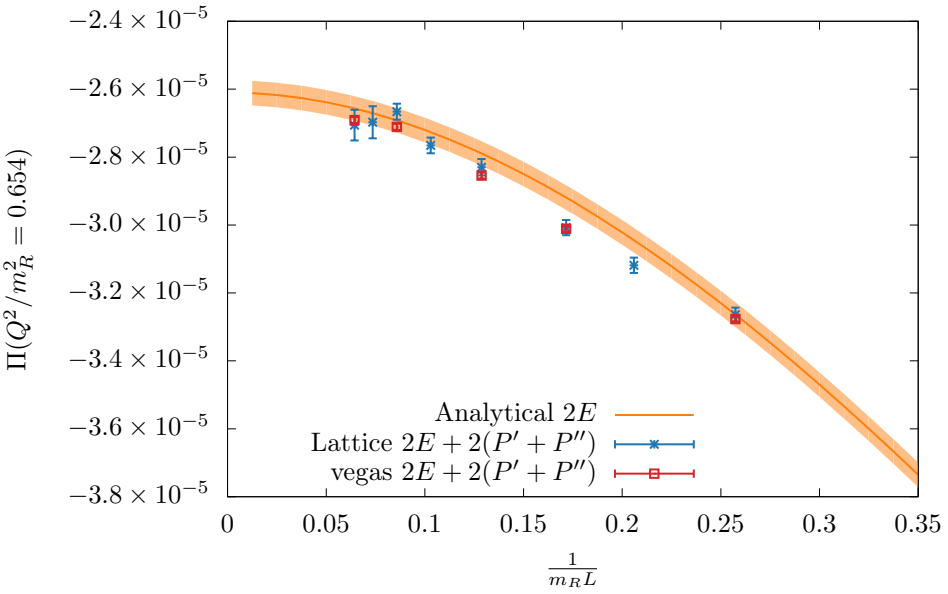

FIGURE 7.10: Renormalised contribution $2E + 2P'^{(E)} + 2P''^{(E)}$ to the HVP with momentum $Q^2 = 0.654 m_R^2$. The blue crosses are from numerical lattice scalar QED_L calculations, the red squares are calculated using `vegas`, and the orange line is the analytical expression $2\Delta\Pi_E$, defined in appendix B. The shaded band is the uncertainty from the calculation of the infinite-volume limit.

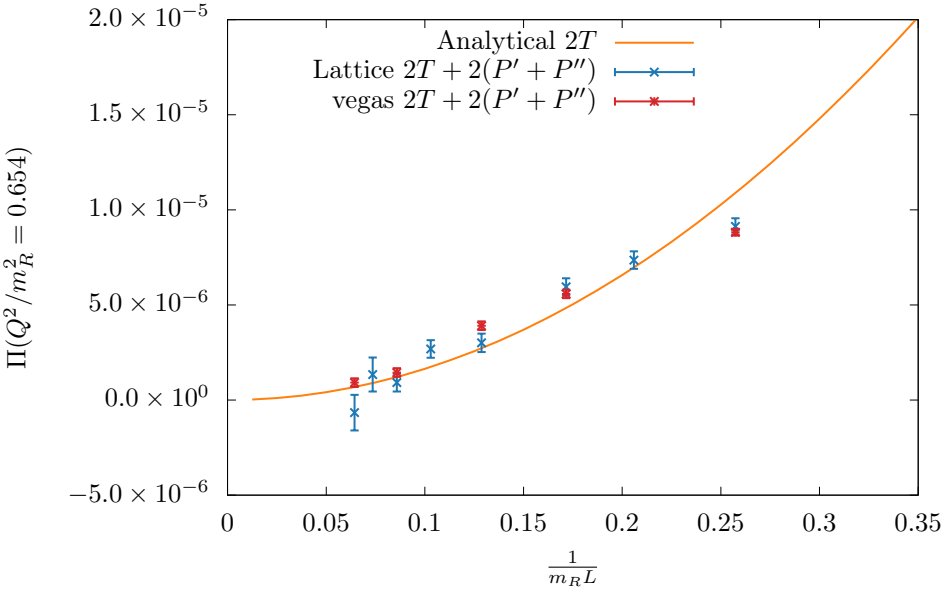

FIGURE 7.11: Renormalised contribution $2T + 2P'^{(T)} + 2P''^{(T)}$ to the HVP with momentum $Q^2 = 0.654 m_R^2$. The blue crosses are from numerical lattice scalar QED_L calculations, the red squares are calculated using `vegas`, and the orange line is the analytical expression $2\Delta\Pi_T$, defined in appendix B.

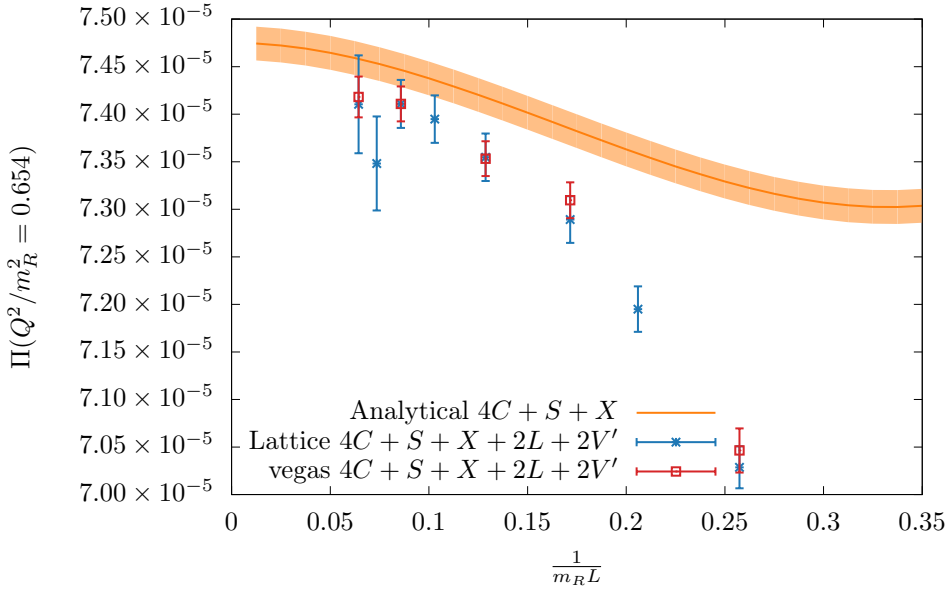

FIGURE 7.12: Renormalised contribution $4C+S+X+2L+2V'$ to the HVP with momentum $Q^2 = 0.654m_R^2$. The blue crosses are from numerical lattice scalar QED_L calculations, the red squares are calculated using `vegas`, and the orange line is the analytical expression $4\Delta\Pi_C + \Delta\Pi_S + \Delta\Pi_X$, defined in appendix B. The shaded band is the uncertainty from the calculation of the infinite-volume limit.

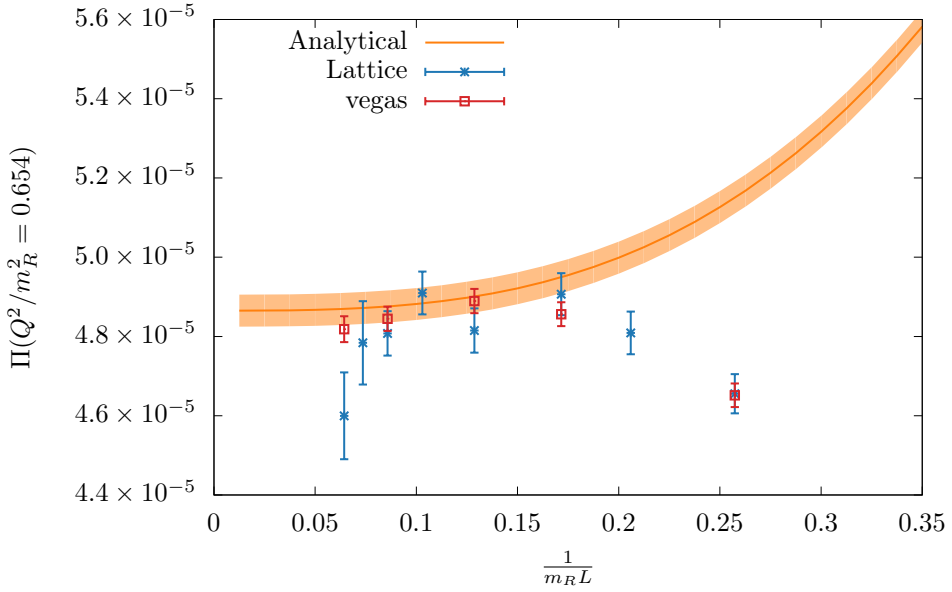

FIGURE 7.13: Total $\mathcal{O}(\alpha)$ HVP correction with momentum $Q^2 = 0.654m_R^2$. The blue crosses are from numerical lattice scalar QED_L calculations, the red squares are calculated using `vegas`, and the orange line is the analytical expression Eq. (7.104). The shaded band is the uncertainty from the calculation of the infinite-volume limit.

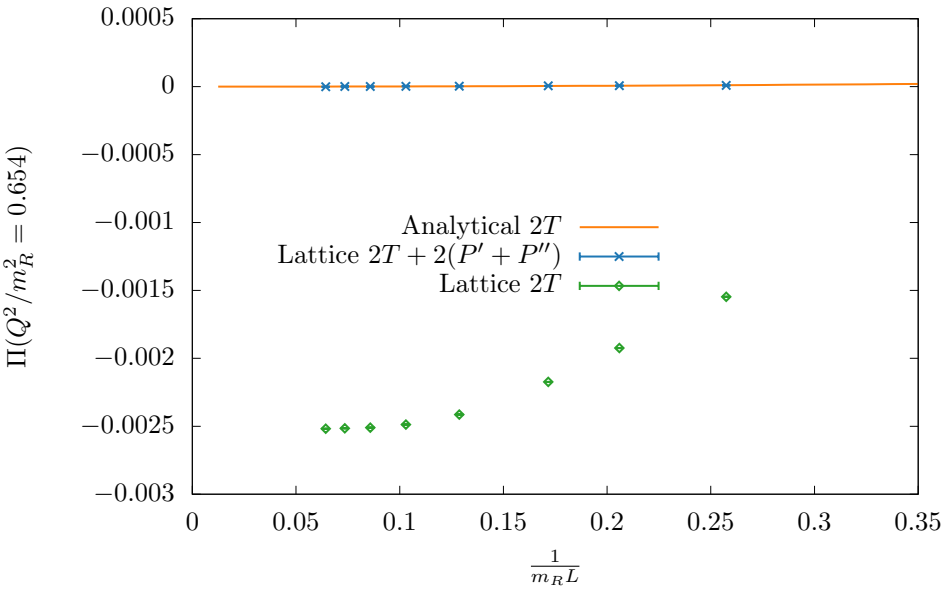

FIGURE 7.14: Unrenormalised embedded tadpole contribution $2T$ (green diamonds), and corresponding renormalised contribution $2T + 2P'^{(T)} + 2P''^{(T)}$ (blue crosses). The orange line is the analytical expression $2\Delta\Pi_T$, defined in appendix B.

In Fig. 7.14, the unrenormalised embedded tadpole contribution $2T$ and renormalised contribution $2T + 2P'^{(T)} + 2P''^{(T)}$ are plotted together. It is clear that the unrenormalised contribution suffers from a large exponential FV effect, which is removed by subtracting the counterterms.

7.4 Summary

We have developed an efficient numerical method for calculating QED_L FV effects, using lattice scalar QED as an effective field theory. This method uses fast Fourier transforms, along with stochastic photon fields, to invert scalar propagators, and is computationally cheap compared with lattice QCD simulations. The method has been implemented in the Grid library [201] so that good performance can be achieved on a range of computational architectures, and so that it can be easily extended to calculate QED FV effects for different quantities.

We have used our numerical method to calculate QED_L FV effects for the scalar self-energy in on-shell and off-shell moving frames. These numerical results are compared with analytical calculations of the same effects, and are found to be in good agreement up to effects proportional to e^{-mL} which are neglected in the analytical calculation. The extraction of the on-shell self energy from lattice correlators is affected by severe excited-state contamination at large volumes, due to the absence of a mass gap in QED. In lattice scalar QED we can remove these excited state contributions through exact analytical calculations, but this would not be possible in a non-perturbative theory. This contamination may be a problem for large-volume lattice QCD+QED calculations in the future.

We have implemented a method of infrared improvement in our numerical framework, by weighting low-energy modes of the photon action to suppress leading FV effects. We have demonstrated that this method can be used to generate QED gauge ensembles on which hadron mass FV effects are suppressed below $\mathcal{O}(1\%)$ for all volumes $mL \gtrsim 4$.

In addition to the scalar self energy, we have calculated QED_L FV effects for the HVP, and again compared with analytical calculations of these effects. Through this comparison the presence of divergent FV effects became apparent. This is a result of mixing between UV and IR effects in the two-loop diagrams, and the theory must be renormalised to calculate the correct FV effects on the lattice. After calculating and subtracting the appropriate counterterms, our lattice results are found to be consistent with the analytical predictions up to small cutoff effects and terms neglected in the analytical calculation, and in excellent agreement with results obtained through direct numerical integration of the lattice perturbation theory expressions. The leading QED FV effect for the HVP is found to be $\mathcal{O}\left(1/L^3\right)$, making these effects negligible in current state-of-the-art lattice QCD+QED calculations.

We have found the process of implementing lattice scalar QED simulations, and comparing with analytical calculations, extremely valuable for understanding various methodological features of lattice QED simulations, including the correct treatment of cut-off effects and excited state contributions. We have shown this method to be efficient for numerically calculating QED FV effects, and it would be well-suited for calculating FV effects on other quantities for which analytical results are not known and would be difficult to calculate.

Chapter 8

Conclusions

High-precision lattice QCD calculations are now reaching a precision at which systematic errors arising from the assumption of isospin symmetry are becoming significant, so it is necessary to include electromagnetic effects in these calculations. Several methods for including QED on the lattice have been proposed and used by the lattice field theory community. In this thesis, two of these methods are compared to objectively determine which can provide better precision at fixed computational cost. Isospin-breaking corrections to the hadronic vacuum polarisation and its contribution to the anomalous magnetic moment of the muon have also been calculated, in an exploratory calculation with unphysical masses, for the first time.

The photon is a massless particle, and the range of electromagnetic interactions is infinite, unlike QCD for which the spectrum has a mass gap. The resulting effects of restricting QED to a finite volume are therefore large, typically scaling as powers of the inverse volume. As a result, it is important to correct for finite volume effects in lattice calculations which include QED. Since the volume scaling is sensitive to the low-energy modes of a system, the leading FV effects are typically insensitive to UV effects such as hadron structure and discretisation and can be calculated in an effective theory. An efficient lattice method for numerical scalar QED calculations has been derived and used to calculate leading QED FV effects for the meson self energy and the HVP in the QED_L scheme, and the results are found to be in good agreement with analytical calculations.

In Chapter 5, two methods for calculating QED corrections on the lattice are introduced: a non-perturbative method involving generation of stochastic $U(1)$ gauge fields, and a method based on a perturbative expansion of the path integral in powers of the electromagnetic charge. Both methods have been used in the electro-quenched approximation, allowing for the re-use of $SU(3)$ gauge ensembles generated at considerable cost by the RBC/UKQCD collaboration. In Chapter 6, I implemented and used the stochastic method to calculate QED corrections to meson masses and the HVP on a $24^3 \times 64$ lattice QCD gauge ensemble with larger-than-physical quark masses, and these results were compared with calculations using the perturbative method on the same QCD gauge ensemble. Different methods were required to extract QED corrections to meson masses from data using the two different methods, because data from the stochastic method contain corrections from all orders in α while data from the perturbative method include only the $\mathcal{O}(\alpha)$ corrections. We find meson masses obtained using the two different methods to

be in agreement, up to $\mathcal{O}\left(\alpha^2\right)$ effects which are present only in the stochastic data, and which we are able to resolve at the precision achieved here.

We have calculated QED corrections to the HVP and its contribution to a_μ, both from the QED correction to the electromagnetic vector 2-point function and to the multiplicative renormalisation Z_V of the local vector current. As for the meson masses, the QED corrections to the HVP from both methods are found to be consistent up to $\mathcal{O}\left(\alpha^2\right)$ effects. The QED correction to a_μ from the up quark cannot be resolved from zero with the statistics used here, but the statistical error places an upper bound of 1% for this correction. The QED correction to a_μ from the strange quark is found to be 0.1%. Strong isospin-breaking corrections to the HVP are also calculated, by using different masses for the valence up and down quarks, and are found to be $\approx 0.9\%$. Although no attempt was made to extrapolate these results to the physical point, we conclude that isospin-breaking corrections must be included in a calculation of a_μ to achieve a precision of 1%.

The two methods investigated require different numbers of quark propagator inversions per gauge configuration, and consequently their computational cost differs. Comparing results obtained from the two methods, we find that the stochastic method produces statistical errors which are a factor of 1.5-2 smaller than from the perturbative method, at the same computational cost. An alternative proposal, to use a perturbative expansion of the path integral with the photon propagator estimated from stochastic photon fields, is found in [177] to produce smaller statistical errors than the perturbative method used in this work. Since this method requires fewer propagator inversions than the perturbative method, and will produce identical results to the stochastic method up to $\mathcal{O}\left(\alpha^2\right)$ corrections, this finding is consistent with our own.

In Chapter 7 a method for numerical calculation of QED_L FV effects using scalar QED simulations is derived. Photon field configurations are generated as for the stochastic method, and scalar propagators are calculated up to $\mathcal{O}\left(\alpha\right)$ using fast Fourier transforms. These simulations are computationally cheap compared with full QCD+QED simulations, allowing for precise numerical calculations of FV effects. This method has been implemented in the Grid library [201], with the intention that it can be easily extended to calculate FV effects for new quantities in the future while achieving good performance on the next generation of computing resources.

In Sec. 7.2 this lattice scalar QED framework has been used to calculate QED_L FV effects for the self energy of a scalar particle, extending previous studies of meson mass FV effects to moving frames. Methods are derived to extract the self energy from the lattice scalar 2-point function, for both on-shell and off-shell momentum. A careful treatment of discretisation effects is made, as the high precision achieved in our numerical calculations enables these effects to be resolved. Extraction of the on-shell self energy is affected by significant contamination from excited-state contributions to the scalar 2-point function, due to the absence of an energy gap between the ground state and first excited state in the infinite-volume limit. At large volumes, we find that hundreds or thousands of individual exponential corrections must be subtracted from the correlators, which can only be achieved here by calculating these corrections analytically. This would not be possible in a non-perturbative theory, and the issue of excited-state contamination may be a problem for future lattice QCD+QED calculations in large volumes. The volume scaling of the scalar self energy is found to be in good agreement with analytical predictions, up to a discrepancy which is consistent with exponential corrections excluded in the analytical calculations.

A technique to suppress QED FV effects by tuning a subset of momentum modes of the photon action, a technique we call "infrared improvement", is implemented in lattice scalar QED calculations. We find that this technique gives the expected suppression of FV effects for the scalar squared mass, consistent with analytical predictions, and demonstrate a choice of tuning parameters which suppresses hadron mass FV effects to $< 1\%$ for typical volumes used in state-of-the-art lattice calculations.

Leading QED_L FV effects for the HVP are calculated using lattice scalar QED in Sec. 7.3. Through comparison of numerical and analytical calculations of these effects it became apparent that the FV effects are divergent due to mixing between IR and UV effects at the two-loop level. Renormalisation is required to remove these divergent exponential FV effects, and a scheme for calculating the required counterterms is defined. After renormalisation we find that the volume dependence of the numerical results is well described by analytical predictions, up to small cutoff effects which enter at the two-loop level and $\mathcal{O}\left(1/L^4, e^{-mL}\right)$ effects which are neglected in the analytical calculations. The leading FV correction for each of the $\mathcal{O}(\alpha)$ diagrams contributing to the HVP is $\mathcal{O}\left(1/L^2\right)$ but these effects cancel in the total $\mathcal{O}(\alpha)$ correction, leaving $\mathcal{O}\left(1/L^3\right)$ terms as the leading corrections. The absence of $\mathcal{O}\left(1/L^2\right)$ effects is universal, although the remaining $\mathcal{O}\left(1/L^3\right)$ effects are not, and for $mL \sim 4$ these effects are of $\mathcal{O}(1\%)$ of the QED correction, and are therefore negligible in lattice calculations of the HVP at the current precision.

The lattice calculations of HVP FV effects have been checked by direct numerical integration of lattice perturbation theory integrals, and excellent agreement is found between these two numerical calculations, although it appears that the errors are underestimated in the direct numerical integration. The process of implementing scalar QED calculations on the lattice has proved valuable for understanding features including the problem of excited-state contamination and the constraint on infrared improvement parameters imposed by requiring positivity of the action.

Several simplifications were made in our calculation of isospin-breaking corrections to the HVP. For a calculation at the physical point, the lattice spacing and quark masses must be retuned so that they correspond to the physical masses in the presence of QED. Contributions from quark-disconnected diagrams must also be included. A full calculation of the HVP contribution to a_μ, including isospin-breaking corrections, has been made by the RBC/UKQCD collaboration in [133], and several other recent lattice HVP calculations have also included isospin-breaking corrections [132, 134, 135, 158]. Lattice calculations of other quantities, such as hadron decays, are also reaching a precision at which isospin-breaking corrections are becoming significant, and it is hoped that the work presented in this thesis will be useful in the calculation of isospin-breaking corrections and QED finite-volume effects for these quantities.

Appendix A

NLO HVP diagrams in lattice perturbation theory

This appendix contains analytical expressions for the integrands of the lattice-discretised diagrams E, T, C, S and X shown in Fig. 7.8. The external photon momentum is Q, and the scalar and photon loop momenta are p and k respectively.

$$(T) = \frac{4\sum_{\mu,i}\cos\left(ap_\mu\right)\,\sin^2\left(a\frac{(2p-Q)_i}{2}\right)}{\left(\hat{p}^2+m^2\right)^2\left(\left(\widehat{p-Q}\right)^2+m^2\right)\hat{k}^2} \tag{A.1}$$

$$(E) = \frac{-16\sum_{\mu,i}\sin^2\left(a\frac{(2p-Q)_i}{2}\right)\sin^2\left(a\frac{(2p-k)_\mu}{2}\right)}{\left(\hat{p}^2+m^2\right)^2\left(\left(\widehat{p-Q}\right)^2+m^2\right)\left(\left(\widehat{p-k}\right)^2+m^2\right)\hat{k}^2} \tag{A.2}$$

$$(S) = \frac{-4\sum_{i}\cos^2\left(a\frac{(2p+k-Q)_i}{2}\right)}{\left(\hat{p}^2+m^2\right)\left(\left(\widehat{k+p-Q}\right)^2+m^2\right)\hat{k}^2} \tag{A.3}$$

$$(C) = \frac{8\sum_{i}\sin\left(a\frac{(2p-Q)_i}{2}\right)\,\sin\left(a\frac{(2p-k)_i}{2}\right)\,\cos\left(a\frac{(2p-k-Q)_i}{2}\right)}{\left(\hat{p}^2+m^2\right)\left(\left(\widehat{p-Q}\right)^2+m^2\right)\left(\left(\widehat{k-p}\right)^2+m^2\right)\hat{k}^2} \tag{A.4}$$

$$(X) = \frac{-16\sum_{\mu,i}\sin\left(a\frac{(2p-Q)_i}{2}\right)\,\sin\left(a\frac{(2p-2k-Q)_i}{2}\right)\,\sin\left(a\frac{(2p-k)_\mu}{2}\right)\,\sin\left(a\frac{(2p-k-2Q)_\mu}{2}\right)}{\left(\hat{p}^2+m^2\right)\left(\left(\widehat{p-Q}\right)^2+m^2\right)\left(\left(\widehat{k-p}\right)^2+m^2\right)\left(\left(\widehat{p-k-Q}\right)^2+m^2\right)\hat{k}^2} \tag{A.5}$$

Appendix B

Analytical QED_L FV effects for NLO HVP diagrams

In this appendix, analytical expressions for the QED_L FV effects on NLO contributions to the HVP are reproduced from [8]. The FV effects for the diagrams E, T, C, S and X shown in Fig. 7.8 are:

$$\begin{aligned}\Delta\Pi_E(z) =& \frac{c_1}{\pi m^2 L^2}\left(-\frac{4}{3}\,\Omega_{-1,3}+\frac{1}{2}\,\Omega_{1,2}+\frac{4}{3}\,\Omega_{1,3}-\frac{1}{4}\,\Omega_{3,1}\right)+\frac{1}{m^3L^3}\left(-\frac{8}{3}\,\Omega_{0,3}+\frac{32}{3}\,\Omega_{0,4}\right.\\ &\left.+\frac{1}{16}\,\Omega_{2,2}+\frac{10}{3}\,\Omega_{2,2}-\frac{32}{3}\,\Omega_{2,4}-\frac{23}{128}\,\Omega_{4,1}+\frac{5}{16}\,\Omega_{4,2}-\frac{2}{3}\,\Omega_{4,3}\right)+\mathcal{O}\left(\frac{1}{L^4},e^{-mL}\right),\end{aligned} \tag{B.1}$$

$$\begin{aligned}\Delta\Pi_C(z) =& \frac{c_1}{\pi m^2 L^2}\frac{1}{8}\,\Omega_{3,1}+\frac{1}{m^3L^3}\left(+\frac{8}{3}\,\Omega_{0,3}+\frac{1}{6}\,\Omega_{2,2}-\frac{8}{3}\,\Omega_{2,2}+\frac{1}{8}\,\Omega_{4,1}-\frac{1}{6}\,\Omega_{4,2}\right)\\ &+\mathcal{O}\left(\frac{1}{L^4},e^{-mL}\right),\end{aligned} \tag{B.2}$$

$$\Delta\Pi_T(z) = \frac{c_1}{\pi m^2 L^2}\frac{1}{4}\,\Omega_{3,1}+\mathcal{O}\left(\frac{1}{L^4},e^{-mL}\right), \tag{B.3}$$

$$\Delta\Pi_S(z) = \frac{c_1}{\pi m^2 L^2}\left(-\frac{1}{4}\,\Omega_{3,1}\right)+\frac{1}{m^3L^3}\left(-2\,\Omega_{2,2}-\frac{1}{4}\,\Omega_{4,1}\right)+\mathcal{O}\left(\frac{1}{L^4},e^{-mL}\right), \tag{B.4}$$

$$\begin{aligned}\Delta\Pi_X(z) =& \frac{c_1}{\pi m^2 L^2}\left(\frac{8}{3}\,\Omega_{-1,3}-\Omega_{1,2}-\frac{8}{3}\,\Omega_{1,3}-\frac{1}{4}\,\Omega_{3,1}\right)\\ &+\frac{1}{m^3L^3}\left(-\frac{128}{3}\,\Omega_{-2,4}-\frac{16}{3}\,\Omega_{0,3}+64\,\Omega_{0,4}-\frac{11}{24}\,\Omega_{2,2}+\frac{20}{3}\,\Omega_{2,2}\right.\\ &\left.-\frac{64}{3}\,\Omega_{2,4}-\frac{17}{64}\,\Omega_{4,1}+\frac{29}{24}\,\Omega_{4,2}-\frac{4}{3}\,\Omega_{4,3}\right)+\mathcal{O}\left(\frac{1}{L^4},e^{-mL}\right),\end{aligned} \tag{B.5}$$

where $z=-Q^2/m^2$ for external momentum Q^2. The functions $\Omega_{\alpha,\beta}(z)$ are defined as

$$\Omega_{\alpha,\beta}(z) = \frac{1}{2\pi^2}\int_0^\infty dx\, x^2\omega_{\alpha,\beta}(x,z)\,, \tag{B.6}$$

$$\omega_{\alpha,\beta}(x,z) = \frac{1}{(x^2-1)^{\frac{\alpha}{2}}\left[z+4(x^2+1)\right]^\beta}\,, \tag{B.7}$$

and for any positive integer couple (α, β) such that $\alpha + 2\beta > 3$, $\Omega_{\alpha,\beta}(z)$ is a linear combination of the following six functions and their derivatives:

$$
\begin{aligned}
\Omega_{2,1}(z) &= \frac{1}{8\pi z}\left(\sqrt{4+z}-2\right)\,, \\
\Omega_{3,1}(z) &= \frac{1}{4\pi^2 z}\left\{\sqrt{1+\frac{4}{z}}\log\left[\frac{1}{2}\left(z+\sqrt{z(z+4)}+2\right)\right]-2\right\}\,, \\
\Omega_{4,1}(z) &= \frac{1}{8\pi z^2}\left(z-4\sqrt{z+4}+8\right)\,, \\
\Omega_{5,1}(z) &= \frac{1}{6\pi^2 z^{\frac{5}{2}}}\left\{z^{\frac{3}{2}}+12\sqrt{z}-6\sqrt{z+4}\log\left[\frac{1}{2}\left(z+\sqrt{z(z+4)}+2\right)\right]\right\}\,, \\
\Omega_{0,2}(z) &= \frac{1}{64\pi\sqrt{z+4}}\,, \\
\Omega_{1,2}(z) &= \frac{1}{16\pi^2 z^2(z+4)}\left\{z(z+4)-2\sqrt{z(z+4)}\log\left[\frac{1}{2}\left(z+\sqrt{z(z+4)}+2\right)\right]\right\}\,.
\end{aligned}
\tag{B.8}
$$

Bibliography

[1] F. Jegerlehner and A. Nyffeler, "The muon $g-2$," *Physics Reports* **477** no. 1, (2009) 1–110.

[2] T. Blum, R. Zhou, T. Doi, M. Hayakawa, T. Izubuchi, S. Uno, and N. Yamada, "Electromagnetic mass splittings of the low lying hadrons and quark masses from 2 + 1 flavor lattice QCD + QED," *Physical Review D* **82** no. 9, (2010) 094508. http://link.aps.org/doi/10.1103/PhysRevD.82.094508.

[3] P. Boyle, V. Gülpers, J. Harrison, A. Jüttner, C. Lehner, A. Portelli, and C. Sachrajda, "Isospin breaking corrections to meson masses and the hadronic vacuum polarization: a comparative study," *Journal of High Energy Physics* **2017** no. 9, (2017) 153. https://doi.org/10.1007/JHEP09(2017)153.

[4] P. Boyle, V. Gülpers, J. Harrison, A. Jüttner, A. Portelli, and C. Sachrajda, "Electromagnetic Corrections to Meson Masses and the HVP," *PoS* **LATTICE2016** (2016) 172, arXiv:1612.05962 [hep-lat].

[5] P. Boyle, V. Gülpers, J. Harrison, A. Jüttner, A. Portelli, and C. Sachrajda, "Numerical investigation of finite-volume effects for the HVP," *EPJ Web Conf.* **175** (2018) 06022.

[6] P. Boyle, V. Gülpers, J. Harrison, A. Jüttner, C. Lehner, A. Portelli, and C. Sachrajda, "Isospin Breaking Corrections to the HVP with Domain Wall Fermions," *EPJ Web Conf.* **175** (2018) 06024, arXiv:1710.07190 [hep-lat].

[7] Z. Davoudi, J. Harrison, A. Jüttner, A. Portelli, and M. J. Savage, "Theoretical aspects of quantum electrodynamics in a finite volume with periodic boundary conditions," *Phys. Rev. D* **99** (Feb, 2019) 034510. https://link.aps.org/doi/10.1103/PhysRevD.99.034510.

[8] J. Bijnens, J. Harrison, N. Hermansson-Truedsson, T. Janowski, A. Jüttner, and A. Portelli, "Electromagnetic finite-size effects to the hadronic vacuum polarization," arXiv:1903.10591 [hep-lat].

[9] T. Aoyama, M. Hayakawa, T. Kinoshita, and M. Nio, "Tenth-Order QED Contribution to the Electron g - 2 and an Improved Value of the Fine Structure Constant," *Physical Review Letters* **109** no. 11, (2012) 111807. http://link.aps.org/doi/10.1103/PhysRevLett.109.111807.

[10] **Particle Data Group** Collaboration, M. Tanabashi *et al.*, "Review of Particle Physics," *Phys. Rev. D* **98** (2018) 030001. https://link.aps.org/doi/10.1103/PhysRevD.98.030001.

[11] **ATLAS** Collaboration, G. Aad *et al.*, "Observation of a new particle in the search for the Standard Model Higgs boson with the ATLAS detector at the LHC," *Physics Letters B* **716** no. 1, (2012) 1 – 29. http://www.sciencedirect.com/science/article/pii/S037026931200857X.

[12] **CMS** Collaboration, S. Chatrchyan *et al.*, "Observation of a new boson at a mass of 125 GeV with the CMS experiment at the LHC," *Physics Letters B* **716** no. 1, (2012) 30 – 61. http://www.sciencedirect.com/science/article/pii/S0370269312008581.

[13] **Planck** Collaboration, P. A. R. Ade *et al.*, "Planck 2015 results - XIII. Cosmological parameters," *A&A* **594** (2016) A13. https://doi.org/10.1051/0004-6361/201525830.

[14] M. Fertl, "Next generation muon g-2 experiment at FNAL," *Hyperfine Interactions* **237** no. 1, (2016) 94. https://doi.org/10.1007/s10751-016-1304-7.

[15] M. Otani, "Status of the Muon $g-2$/EDM Experiment at J-PARC (E34)," *JPS Conf. Proc.* **8** (2015) . http://journals.jps.jp/doi/pdf/10.7566/JPSCP.8.025008.

[16] G. Abbiendi *et al.*, "Measuring the leading hadronic contribution to the muon $g-2$ via μe scattering," *Eur. Phys. J.* **C77** no. 3, (2017) 139, arXiv:1609.08987 [hep-ex].

[17] **FLAG** Collaboration, S. Aoki *et al.*, "Review of lattice results concerning low-energy particle physics," *The European Physical Journal C* **77** no. 2, (2017) 112. https://doi.org/10.1140/epjc/s10052-016-4509-7.

[18] A. Duncan, E. Eichten, and H. Thacker, "Electromagnetic Splittings and Light Quark Masses in Lattice QCD," *Physical Review Letters* **76** no. 21, (1996) 3894–3897. http://link.aps.org/doi/10.1103/PhysRevLett.76.3894.

[19] G. M. de Divitiis, R. Frezzotti, V. Lubicz, G. Martinelli, R. Petronzio, G. C. Rossi, F. Sanfilippo, S. Simula, and N. Tantalo, "Leading isospin breaking effects on the lattice," *Physical Review D* **87** no. 11, (2013) 114505. https://inspirehep.net/record/1224545/.

[20] R. Horsley, Y. Nakamura, D. Pleiter, P. E. L. Rakow, G. Schierholz, H. Stüben, R. D. Young, and J. M. Zanotti, "Electromagnetic splitting of quark and pseudoscalar meson masses from dynamical QCD + QED," *PoS* **Lattice2013** (2014) 499, arXiv:1311.4554 [hep-lat].

[21] S. Borsanyi, S. Durr, Z. Fodor, C. Hoelbling, S. D. Katz, S. Krieg, L. Lellouch, T. Lippert, A. Portelli, K. K. Szabo, and B. C. Toth, "Ab initio calculation of the neutron-proton mass difference," *Science* **347** no. 6229, (2015) 1452–1455. http://www.sciencemag.org/content/347/6229/1452.short.

[22] A. Duncan, E. Eichten, and R. Sedgewick, "Computing electromagnetic effects in fully unquenched QCD," *Physical Review D* **71** no. 9, (2005) 094509. http://link.aps.org/doi/10.1103/PhysRevD.71.094509.

[23] S. Uno and M. Hayakawa, "QED in Finite Volume and Finite Size Scaling Effect on Electromagnetic Properties of Hadrons," *Progress of Theoretical Physics* **120** no. 3, (2008) 413–441. http://ptp.oxfordjournals.org/cgi/doi/10.1143/PTP.120.413.

[24] M. G. Endres, A. Shindler, B. C. Tiburzi, and A. Walker-Loud, "Massive Photons: An Infrared Regularization Scheme for Lattice QCD + QED," *Phys. Rev. Lett.* **117** (2016) 072002. https://link.aps.org/doi/10.1103/PhysRevLett.117.072002.

[25] B. Lucini, A. Patella, A. Ramos, and N. Tantalo, "Charged hadrons in local finite-volume QED+QCD with C* boundary conditions," *Journal of High Energy Physics* **2016** no. 2, (2016) 76. https://doi.org/10.1007/JHEP02(2016)076.

[26] F. Zwicky, "On the Masses of Nebulae and of Clusters of Nebulae," *Astrophysical Journal* **86** (1937) 217.

[27] **Super-Kamiokande** Collaboration, Y. Fukuda *et al.*, "Evidence for Oscillation of Atmospheric Neutrinos," *Phys. Rev. Lett.* **81** (1998) 1562–1567. https://link.aps.org/doi/10.1103/PhysRevLett.81.1562.

[28] **SNO** Collaboration, Q. Ahmad and others, "Direct Evidence for Neutrino Flavor Transformation from Neutral-Current Interactions in the Sudbury Neutrino Observatory," *Phys. Rev. Lett.* **89** (2002) 011301. https://link.aps.org/doi/10.1103/PhysRevLett.89.011301.

[29] P. A. M. Dirac, "The Quantum Theory of the Electron," *Proceedings of the Royal Society A: Mathematical, Physical and Engineering Sciences* **117** no. 778, (1928) 610–624. http://rspa.royalsocietypublishing.org/cgi/doi/10.1098/rspa.1928.0023.

[30] P. Clifford, "Applications of Grassman's Extensive Algebra," *American Journal of Mathematics* **1** (1878) 350–358.

[31] W. Pauli, "Zur Quantenmechanik des magnetischen Elektrons," *Zeitschrift für Physik* **43** no. 9, (1927) 601–623. https://doi.org/10.1007/BF01397326.

[32] R. P. Feynman, "Space-Time Approach to Non-Relativistic Quantum Mechanics," *Rev. Mod. Phys.* **20** (1948) 367–387. https://link.aps.org/doi/10.1103/RevModPhys.20.367.

[33] L. Lorenz, "XXXVIII. On the identity of the vibrations of light with electrical currents," *The London, Edinburgh, and Dublin Philosophical Magazine and Journal of Science* **34** no. 230, (1867) 287–301. https://doi.org/10.1080/14786446708639882.

[34] O. Heaviside, "XXXIX. On the electromagnetic effects due to the motion of electrification through a dielectric," *The London, Edinburgh, and Dublin Philosophical Magazine and Journal of Science* **27** no. 167, (1889) 324–339. https://doi.org/10.1080/14786448908628362.

[35] L. Faddeev and V. Popov, "Feynman diagrams for the Yang-Mills field," *Physics Letters B* **25** no. 1, (1967) 29 – 30. http://www.sciencedirect.com/science/article/pii/0370269367900676.

[36] L. D. Landau and I. M. Khalatnikov, "The gauge transformation of the Green function for charged particles," *Sov. Phys. JETP* **2** (1956) 69. [Zh. Eksp. Teor. Fiz.29,89(1955)].

[37] R. P. Feynman, "Space-Time Approach to Quantum Electrodynamics," *Phys. Rev.* **76** (1949) 769–789. https://link.aps.org/doi/10.1103/PhysRev.76.769.

[38] S. Tomonaga, "On a Relativistically Invariant Formulation of the Quantum Theory of Wave Fields," *Progress of Theoretical Physics* **1** no. 2, (1946) 27–42. http://dx.doi.org/10.1143/PTP.1.27.

[39] J. Schwinger, "On Quantum-Electrodynamics and the Magnetic Moment of the Electron," *Phys. Rev.* **73** (1948) 416–417. https://link.aps.org/doi/10.1103/PhysRev.73.416.

[40] J. Schwinger, "Quantum Electrodynamics. I. A Covariant Formulation," *Physical Review* **74** (1948) 1439–1461.

[41] R. P. Feynman, "The Theory of Positrons," *Phys. Rev.* **76** (1949) 749–759. https://link.aps.org/doi/10.1103/PhysRev.76.749.

[42] R. P. Feynman, "Mathematical Formulation of the Quantum Theory of Electromagnetic Interaction," *Phys. Rev.* **80** (1950) 440–457. https://link.aps.org/doi/10.1103/PhysRev.80.440.

[43] F. J. Dyson, "The Radiation Theories of Tomonaga, Schwinger, and Feynman," *Phys. Rev.* **75** (1949) 486–502. https://link.aps.org/doi/10.1103/PhysRev.75.486.

[44] F. J. Dyson, "The S Matrix in Quantum Electrodynamics," *Phys. Rev.* **75** (1949) 1736–1755. https://link.aps.org/doi/10.1103/PhysRev.75.1736.

[45] G. 't Hooft, "Dimensional regularization and the renormalization group," *Nuclear Physics B* **61** (1973) 455 – 468. http://www.sciencedirect.com/science/article/pii/0550321373903763.

[46] S. Weinberg, "New Approach to the Renormalization Group," *Phys. Rev. D* **8** (1973) 3497–3509. https://link.aps.org/doi/10.1103/PhysRevD.8.3497.

[47] C. N. Yang and R. L. Mills, "Conservation of Isotopic Spin and Isotopic Gauge Invariance," *Phys. Rev.* **96** (1954) 191–195. https://link.aps.org/doi/10.1103/PhysRev.96.191.

[48] H. Fritzsch, M. Gell-Mann, and H. Leutwyler, "Advantages of the color octet gluon picture," *Physics Letters B* **47** no. 4, (1973) 365 – 368. http://www.sciencedirect.com/science/article/pii/0370269373906254.

[49] M. Gell-Mann, "Symmetries of Baryons and Mesons," *Phys. Rev.* **125** (1962) 1067–1084. https://link.aps.org/doi/10.1103/PhysRev.125.1067.

[50] D. J. Gross and F. Wilczek, "Ultraviolet Behavior of Non-Abelian Gauge Theories," *Phys. Rev. Lett.* **30** (1973) 1343–1346. https://link.aps.org/doi/10.1103/PhysRevLett.30.1343.

[51] H. D. Politzer, "Reliable Perturbative Results for Strong Interactions?," *Phys. Rev. Lett.* **30** (1973) 1346–1349. https://link.aps.org/doi/10.1103/PhysRevLett.30.1346.

[52] K. G. Wilson, "Confinement of quarks," *Physical Review D* **10** no. 8, (1974) 2445–2459. http://link.aps.org/doi/10.1103/PhysRevD.10.2445.

[53] J. Goldstone, A. Salam, and S. Weinberg, "Broken Symmetries," *Phys. Rev.* **127** (1962) 965–970. https://link.aps.org/doi/10.1103/PhysRev.127.965.

[54] S. Weinberg, "A Model of Leptons," *Phys. Rev. Lett.* **19** (1967) 1264–1266. https://link.aps.org/doi/10.1103/PhysRevLett.19.1264.

[55] S. L. Glashow, "Partial-symmetries of weak interactions," *Nuclear Physics* **22** no. 4, (1961) 579 – 588. http://www.sciencedirect.com/science/article/pii/0029558261904692.

[56] P. W. Higgs, "Broken Symmetries and the Masses of Gauge Bosons," *Phys. Rev. Lett.* **13** (1964) 508–509. https://link.aps.org/doi/10.1103/PhysRevLett.13.508.

[57] P. Higgs, "Broken symmetries, massless particles and gauge fields," *Physics Letters* **12** no. 2, (1964) 132 – 133. http://www.sciencedirect.com/science/article/pii/0031916364911369.

[58] F. Englert and R. Brout, "Broken Symmetry and the Mass of Gauge Vector Mesons," *Phys. Rev. Lett.* **13** (1964) 321–323. https://link.aps.org/doi/10.1103/PhysRevLett.13.321.

[59] G. S. Guralnik, C. R. Hagen, and T. W. B. Kibble, "Global Conservation Laws and Massless Particles," *Phys. Rev. Lett.* **13** (1964) 585–587. https://link.aps.org/doi/10.1103/PhysRevLett.13.585.

[60] J. C. Ward, "An Identity in Quantum Electrodynamics," *Phys. Rev.* **78** (1950) 182–182. https://link.aps.org/doi/10.1103/PhysRev.78.182.

[61] Y. Takahashi, "On the generalized Ward identity," *Il Nuovo Cimento (1955-1965)* **6** no. 2, (1957) 371–375. https://doi.org/10.1007/BF02832514.

[62] E. Noether, "Invariant variation problems," *Transport Theory and Statistical Physics* **1** no. 3, (1971) 186–207. https://doi.org/10.1080/00411457108231446.

[63] S. L. Adler, "Axial-Vector Vertex in Spinor Electrodynamics," *Phys. Rev.* **177** (1969) 2426–2438. https://link.aps.org/doi/10.1103/PhysRev.177.2426.

[64] J. S. Bell and R. Jackiw, "A PCAC puzzle: $\pi 0 \to \gamma\gamma$ in the σ-model," *Il Nuovo Cimento A (1965-1970)* **60** no. 1, (1969) 47–61. https://doi.org/10.1007/BF02823296.

[65] G. 't Hooft, "How instantons solve the U(1) problem," *Physics Reports* **142** no. 6, (1986) 357 – 387. http://www.sciencedirect.com/science/article/pii/0370157386901171.

[66] W. Heisenberg, "Über den Bau der Atomkerne. I," *Zeitschrift für Physik* **77** no. 1, (1932) 1–11. https://doi.org/10.1007/BF01342433.

[67] E. Wigner, "On the Consequences of the Symmetry of the Nuclear Hamiltonian on the Spectroscopy of Nuclei," *Phys. Rev.* **51** (1937) 106–119. https://link.aps.org/doi/10.1103/PhysRev.51.106.

[68] M. Gell-Mann, "The Symmetry group of vector and axial vector currents," *Physics Physique Fizika* **1** (1964) 63–75.

[69] M. Gell-Mann, "The Eightfold Way: A Theory of strong interaction symmetry,".

[70] M. Gell-Mann, R. J. Oakes, and B. Renner, "Behavior of Current Divergences under $SU_3 \times SU_3$," *Phys. Rev.* **175** (1968) 2195–2199. https://link.aps.org/doi/10.1103/PhysRev.175.2195.

[71] F. Hansen, "Finite-size effects in spontaneously broken SU(N) × SU(N) theories," *Nuclear Physics B* **345** no. 2, (1990) 685 – 708. http://www.sciencedirect.com/science/article/pii/0550321390904053.

[72] **Budapest-Marseille-Wuppertal** Collaboration, S. Dürr *et al.*, "Lattice QCD at the physical point meets $SU(2)$ chiral perturbation theory," *Phys. Rev. D* **90** (2014) 114504. https://link.aps.org/doi/10.1103/PhysRevD.90.114504.

[73] A. Bazavov *et al.*, "Staggered chiral perturbation theory in the two-flavor case and SU(2) analysis of the MILC data," *PoS* **LATTICE2010** (2010) 083, arXiv:1011.1792 [hep-lat].

[74] S. Borsányi, S. Dürr, Z. Fodor, S. Krieg, A. Schäfer, E. E. Scholz, and K. K. Szabó, "SU(2) chiral perturbation theory low-energy constants from 2+1 flavor staggered lattice simulations," *Phys. Rev. D* **88** (2013) 014513. https://link.aps.org/doi/10.1103/PhysRevD.88.014513.

[75] P. A. Boyle, N. H. Christ, N. Garron, C. Jung, A. Jüttner, C. Kelly, R. D. Mawhinney, G. McGlynn, D. J. Murphy, S. Ohta, A. Portelli, and C. T. Sachrajda, "Low energy constants of $SU(2)$ partially quenched chiral perturbation theory from $N_f = 2 + 1$ domain wall QCD," *Phys. Rev. D* **93** (2016) 054502. https://link.aps.org/doi/10.1103/PhysRevD.93.054502.

[76] J. Goldstone, "Field theories with "Superconductor" solutions," *Il Nuovo Cimento (1955-1965)* **19** no. 1, (1961) 154–164. https://doi.org/10.1007/BF02812722.

[77] C. Gattringer and C. B. Lang, *Quantum Chromodynamics on the Lattice*, vol. 788 of *Lecture Notes in Physics*. Springer Berlin Heidelberg, Berlin, Heidelberg, 2010. http://link.springer.com/10.1007/978-3-642-01850-3.

[78] T. DeGrand and C. DeTar, *Lattice Methods for Quantum Chromodynamics*. World Scientific Publishing, 2006.

[79] G. C. Wick, "Properties of Bethe-Salpeter Wave Functions," *Phys. Rev.* **96** (1954) 1124–1134. https://link.aps.org/doi/10.1103/PhysRev.96.1124.

[80] K. G. Wilson and J. Kogut, "The renormalization group and the ϵ expansion," *Physics Reports* **12** no. 2, (1974) 75 – 199. http://www.sciencedirect.com/science/article/pii/0370157374900234.

[81] M. Lüscher and P. Weisz, "On-shell improved lattice gauge theories," *Communications in Mathematical Physics* **97** no. 1, (1985) 59–77. https://doi.org/10.1007/BF01206178.

[82] P. Weisz, "Continuum limit improved lattice action for pure Yang-Mills theory (I)," *Nuclear Physics B* **212** no. 1, (1983) 1 – 17. http://www.sciencedirect.com/science/article/pii/0550321383905953.

[83] "Continuum limit improved lattice action for pure Yang-Mills theory (II): P. Weisz and R. Wohlert, Nucl. Phys. B236 (1984) 397," *Nuclear Physics B* **247** no. 2, (1984) 544 – 545. http://www.sciencedirect.com/science/article/pii/0550321384905637.

[84] Y. Iwasaki, "Renormalization Group Analysis of Lattice Theories and Improved Lattice Action. II. Four-dimensional non-Abelian SU(N) gauge model," arXiv:1111.7054 [hep-lat].

[85] Y. Iwasaki and T. Yoshié, "Renormalization group improved action for SU(3) lattice gauge theory and the string tension," *Physics Letters B* **143** no. 4, (1984) 449 – 452. http://www.sciencedirect.com/science/article/pii/0370269384915004.

[86] Y. Iwasaki, "Renormalization group analysis of lattice theories and improved lattice action: Two-dimensional non-linear O(N) sigma model," *Nuclear Physics B* **258** (1985) 141 – 156. http://www.sciencedirect.com/science/article/pii/0550321385906066.

[87] M. Bochicchio, L. Maiani, G. Martinelli, G. Rossi, and M. Testa, "Chiral symmetry on the lattice with Wilson fermions," *Nuclear Physics B* **262** no. 2, (1985) 331 – 355. http://www.sciencedirect.com/science/article/pii/0550321385902901.

[88] H. Nielsen and M. Ninomiya, "A no-go theorem for regularizing chiral fermions," *Physics Letters B* **105** no. 2, (1981) 219 – 223. http://www.sciencedirect.com/science/article/pii/0370269381910261.

[89] P. H. Ginsparg and K. G. Wilson, "A remnant of chiral symmetry on the lattice," *Phys. Rev. D* **25** (1982) 2649–2657. https://link.aps.org/doi/10.1103/PhysRevD.25.2649.

[90] D. B. Kaplan, "A method for simulating chiral fermions on the lattice," *Physics Letters B* **288** no. 3-4, (1992) 342–347. http://linkinghub.elsevier.com/retrieve/pii/037026939291112M.

[91] Y. Shamir, "Chiral fermions from lattice boundaries," *Nuclear Physics B* **406** no. 1, (1993) 90 – 106. http://www.sciencedirect.com/science/article/pii/055032139390162I.

[92] Y. Shamir, "Constraints on the existence of chiral fermions in interacting lattice theories," *Phys. Rev. Lett.* **71** (1993) 2691–2694. https://link.aps.org/doi/10.1103/PhysRevLett.71.2691.

[93] Y. Shamir, "Anomalies and chiral defect fermions," *Nuclear Physics B* **417** no. 1, (1994) 167 – 180. http://www.sciencedirect.com/science/article/pii/0550321394905428.

[94] V. Furman and Y. Shamir, "Axial symmetries in lattice QCD with Kaplan fermions," *Nuclear Physics B* **439** no. 1, (1995) 54 – 78. http://www.sciencedirect.com/science/article/pii/055032139500031M.

[95] R. C. Brower, H. Neff, and K. Orginos, "Möbius Fermions: Improved Domain Wall Chiral Fermions," *Nuclear Physics B - Proceedings Supplements* **140** (2005) 686 – 688. http://www.sciencedirect.com/science/article/pii/S092056320400920X. LATTICE 2004.

[96] R. Brower, H. Neff, and K. Orginos, "Möbius Fermions," *Nuclear Physics B - Proceedings Supplements* **153** no. 1, (2006) 191 – 198. http://www.sciencedirect.com/science/article/pii/S0920563206000296. Proceedings of the Workshop on Computational Hadron Physics.

[97] T. Blum *et al.*, "Quenched lattice QCD with domain wall fermions and the chiral limit," *Phys. Rev. D* **69** (2004) 074502. https://link.aps.org/doi/10.1103/PhysRevD.69.074502.

[98] P. T. Matthews and A. Salam, "The Green's functions of quantised fields," *Il Nuovo Cimento (1943-1954)* **12** no. 4, (1954) 563–565. https://doi.org/10.1007/BF02781302.

[99] P. T. Matthews and A. Salam, "Propagators of quantized field," *Il Nuovo Cimento (1955-1965)* **2** no. 1, (1955) 120–134. https://doi.org/10.1007/BF02856011.

[100] N. Metropolis, A. W. Rosenbluth, M. N. Rosenbluth, A. H. Teller, and E. Teller, "Equation of State Calculations by Fast Computing Machines," *The Journal of Chemical Physics* **21** no. 6, (1953) 1087–1092. https://doi.org/10.1063/1.1699114.

[101] S. Duane, A. Kennedy, B. J. Pendleton, and D. Roweth, "Hybrid Monte Carlo," *Physics Letters B* **195** no. 2, (1987) 216 – 222. http://www.sciencedirect.com/science/article/pii/037026938791197X.

[102] G. C. Wick, "The Evaluation of the Collision Matrix," *Physical Review* **80** no. 2, (1950) 268–272. http://link.aps.org/doi/10.1103/PhysRev.80.268.

[103] M. R. Hestenes and E. Stiefel, "Methods of conjugate gradients for solving linear systems," *Journal of Research of the National Bureau of Standards* **49** no. 6, (1952) 409–436. http://ci.nii.ac.jp/naid/10007226409/en/.

[104] S.-J. Dong and K.-F. Liu, "Stochastic estimation with Z_2 noise," *Physics Letters B* **328** no. 1, (1994) 130 – 136. http://www.sciencedirect.com/science/article/pii/0370269394904405.

[105] **UKQCD** Collaboration, M. Foster and C. Michael, "Quark mass dependence of hadron masses from lattice QCD," *Phys. Rev. D* **59** (1999) 074503. https://link.aps.org/doi/10.1103/PhysRevD.59.074503.

[106] **RBC & UKQCD** Collaboration, P. Boyle, C. Kelly, R. Kenway, and A. Jüttner, "Use of stochastic sources for the lattice determination of light quark physics," *Journal of High Energy Physics* **2008** no. 08, (2008) 086. http://stacks.iop.org/1126-6708/2008/i=08/a=086.

[107] M. Lüscher, "Volume dependence of the energy spectrum in massive quantum field theories," *Communications in Mathematical Physics* **104** no. 2, (1986) 177–206. https://doi.org/10.1007/BF01211589.

[108] G. Colangelo, S. Dürr, and C. Haefeli, "Finite volume effects for meson masses and decay constants," *Nuclear Physics B* **721** no. 1, (2005) 136 – 174. http://www.sciencedirect.com/science/article/pii/S0550321305004268.

[109] J. W. Tukey, "Bias and confidence in not-quite large samples," *Ann. Math. Statist.* **29** (1958) 614.

[110] B. Efron, *Bootstrap Methods: Another Look at the Jackknife*, pp. 569–593. Springer New York, New York, NY, 1992. https://doi.org/10.1007/978-1-4612-4380-9_41.

[111] T. Blum, "Lattice Calculation of the Lowest-Order Hadronic Contribution to the Muon Anomalous Magnetic Moment," *Physical Review Letters* **91** no. 5, (2003) 052001. http://link.aps.org/doi/10.1103/PhysRevLett.91.052001.

[112] A. Czarnecki and W. J. Marciano, "Muon anomalous magnetic moment: A harbinger for "new physics"," *Physical Review D* **64** no. 1, (2001) 013014. http://link.aps.org/doi/10.1103/PhysRevD.64.013014.

[113] **Muon g-2** Collaboration, G. W. Bennett *et al.*, "Final report of the E821 muon anomalous magnetic moment measurement at BNL," *Physical Review D* **73** no. 7, (2006) 072003. http://link.aps.org/doi/10.1103/PhysRevD.73.072003.

[114] R. Carey, K. Lynch, J. Miller, B. Roberts, W. Morse, Y. Semertzides, V. Druzhinin, B. Khazin, I. Koop, I. Logashenko, and S. Redin, "The New (g-2) Experiment: A proposal to measure the muon anomalous magnetic moment to ± 0.14 ppm precision," tech. rep., Fermi National Accelerator Laboratory (FNAL), Batavia, IL (United States), 2009. http://www.osti.gov/servlets/purl/952029-2TyrgK/.

[115] M. Davier, A. Hoecker, B. Malaescu, and Z. Zhang, "Reevaluation of the hadronic vacuum polarisation contributions to the Standard Model predictions of the muon $g-2$ and $\alpha(m_Z^2)$ using newest hadronic cross-section data," *The European Physical Journal C* **77** no. 12, (2017) 827. https://doi.org/10.1140/epjc/s10052-017-5161-6.

[116] Jegerlehner, Fred, "Muon g - 2 theory: The hadronic part," *EPJ Web Conf.* **166** (2018) 00022. https://doi.org/10.1051/epjconf/201816600022.

[117] A. Keshavarzi, D. Nomura, and T. Teubner, "Muon $g-2$ and $\alpha(M_Z^2)$: A new data-based analysis," *Phys. Rev. D* **97** (2018) 114025. https://link.aps.org/doi/10.1103/PhysRevD.97.114025.

[118] C. Aubin and T. Blum, "Calculating the hadronic vacuum polarization and leading hadronic contribution to the muon anomalous magnetic moment with improved staggered quarks," *Physical Review D* **75** no. 11, (2007) 114502. http://link.aps.org/doi/10.1103/PhysRevD.75.114502.

[119] M. D. Morte, B. Jäger, A. Jüttner, and H. Wittig, "Towards a precise lattice determination of the leading hadronic contribution to $(g-2)_\mu$," *Journal of High Energy Physics* **2012** no. 3, (2012) 55. http://link.springer.com/10.1007/JHEP03(2012)055.

[120] A. Francis, V. Gülpers, G. Herdoíza, G. von Hippel, H. Horch, B. Jäger, H. B. Meyer, E. Shintani, and H. Wittig, "Lattice QCD Studies of the Leading Order Hadronic Contribution to the Muon $g-2$," in *International Conference on High Energy Physics 2014 (ICHEP 2014) Valencia, Spain, July 2-9, 2014*. 2014. arXiv:1411.3031 [hep-lat]. https://inspirehep.net/record/1327485/files/arXiv:1411.3031.pdf.

[121] V. Gülpers, A. Francis, B. Jäger, H. Meyer, G. von Hippel, and H. Wittig, "The leading disconnected contribution to the anomalous magnetic moment of the muon," *PoS* **LATTICE201** (2014) 128, arXiv:1411.7592 [hep-lat].

[122] X. Feng, K. Jansen, M. Petschlies, and D. B. Renner, "Two-Flavor QCD Correction to Lepton Magnetic Moments at Leading Order in the Electromagnetic Coupling," *Physical Review Letters* **107** no. 8, (2011) 081802. http://link.aps.org/doi/10.1103/PhysRevLett.107.081802.

[123] **ETM** Collaboration, F. Burger, X. Feng, G. Hotzel, K. Jansen, M. Petschlies, and D. B. Renner, "Four-flavour leading-order hadronic contribution to the muon anomalous magnetic moment," *Journal of High Energy Physics* **2014** no. 2, (2014) 99. http://link.springer.com/10.1007/JHEP02(2014)099.

[124] B. Chakraborty, C. T. H. Davies, G. C. Donald, R. J. Dowdall, J. Koponen, G. P. Lepage, T. Teubner, and T. Teubner, "Strange and charm quark contributions to the anomalous magnetic moment of the muon," *Physical Review D* **89** no. 11, (2014) 114501. http://link.aps.org/doi/10.1103/PhysRevD.89.114501.

[125] **HPQCD** Collaboration, B. Chakraborty, C. T. H. Davies, P. G. de Oliveira, J. Koponen, G. P. Lepage, and R. S. Van de Water, "Hadronic vacuum polarization contribution to a_μ from full lattice QCD," *Phys. Rev. D* **96** (2017) 034516. https://link.aps.org/doi/10.1103/PhysRevD.96.034516.

[126] P. Boyle, L. D. Debbio, E. Kerrane, and J. Zanotti, "Lattice determination of the hadronic contribution to the muon $g-2$ using dynamical domain wall fermions," *Physical Review D* **85** no. 7, (2012) 074504. http://link.aps.org/doi/10.1103/PhysRevD.85.074504.

[127] T. Blum, P. A. Boyle, T. Izubuchi, L. Jin, A. Jüttner, C. Lehner, K. Maltman, M. Marinkovic, A. Portelli, and M. Spraggs, "Calculation of the hadronic vacuum polarization disconnected contribution to the muon anomalous magnetic moment," arXiv:1512.09054. http://arxiv.org/abs/1512.09054.

[128] **RBC/UKQCD** Collaboration, T. Blum *et al.*, "Lattice calculation of the leading strange quark-connected contribution to the muon $g-2$," *Journal of High Energy Physics* **2016** no. 4, (2016) 63. http://link.springer.com/10.1007/JHEP04(2016)063.

[129] G. S. Bali and G. Endrődi, "Hadronic vacuum polarization and muon $g-2$ from magnetic susceptibilities on the lattice," *Phys. Rev. D* **92** (2015) 054506. https://link.aps.org/doi/10.1103/PhysRevD.92.054506.

[130] S. Borsanyi, Z. Fodor, T. Kawanai, S. Krieg, L. Lellouch, R. Malak, K. Miura, K. K. Szabo, C. Torrero, and B. Toth, "Slope and curvature of the hadron vacuum polarization at vanishing virtuality from lattice QCD," arXiv:1612.02364 [hep-lat].

[131] M. Della Morte, A. Francis, V. Gülpers, G. Herdoíza, G. von Hippel, H. Horch, B. Jäger, H. B. Meyer, A. Nyffeler, and H. Wittig, "The hadronic vacuum polarization contribution to the muon $g-2$ from lattice QCD," *Journal of High Energy Physics* **2017** no. 10, (2017) 20. https://doi.org/10.1007/JHEP10(2017)020.

[132] **ETM** Collaboration, D. Giusti, V. Lubicz, G. Martinelli, F. Sanfilippo, and S. Simula, "Strange and charm HVP contributions to the muon $(g-2)$ including QED corrections with twisted-mass fermions," *Journal of High Energy Physics* **2017** no. 10, (2017) 157. https://doi.org/10.1007/JHEP10(2017)157.

[133] **RBC and UKQCD** Collaboration, T. Blum *et al.*, "Calculation of the Hadronic Vacuum Polarization Contribution to the Muon Anomalous Magnetic Moment," *Phys. Rev. Lett.* **121** (2018) 022003. https://link.aps.org/doi/10.1103/PhysRevLett.121.022003.

[134] **Budapest-Marseille-Wuppertal** Collaboration, S. Borsanyi *et al.*, "Hadronic Vacuum Polarization Contribution to the Anomalous Magnetic Moments of Leptons from First Principles," *Phys. Rev. Lett.* **121** (2018) 022002. https://link.aps.org/doi/10.1103/PhysRevLett.121.022002.

[135] Bussone, Andrea, Della Morte, Michele, and Janowski, Tadeusz, "Electromagnetic corrections to the hadronic vacuum polarization of the photon within QED_L and QED_M," *EPJ Web Conf.* **175** (2018) 06005. https://doi.org/10.1051/epjconf/201817506005.

[136] J. P. Miller, E. de Rafael, and B. L. Roberts, "Muon (g - 2): experiment and theory," *Reports on Progress in Physics* **70** no. 5, (2007) 795–881. http://stacks.iop.org/0034-4885/70/i=5/a=R03?key=crossref.22c023ce7833f0c49b0e325b34858c21.

[137] R. L. Garwin, D. P. Hutchinson, S. Penman, and G. Shapiro, "Accurate Determination of the μ^+ Magnetic Moment," *Physical Review* **118** no. 1, (1960) 271–283. http://link.aps.org/doi/10.1103/PhysRev.118.271.

[138] G. Charpak, F. J. M. Farley, R. L. Garwin, T. Muller, J. C. Sens, V. L. Telegdi, and A. Zichichi, "Measurement of the Anomalous Magnetic Moment of the Muon," *Physical Review Letters* **6** no. 3, (1961) 128–132. http://link.aps.org/doi/10.1103/PhysRevLett.6.128.

[139] J. Bailey, W. Bartl, G. Von Bochmann, R. Brown, F. Farley, H. Jöstlein, E. Picasso, and R. Williams, "Precision measurement of the anomalous magnetic moment of the muon," *Physics Letters B* **28** no. 4, (1968) 287–290. http://linkinghub.elsevier.com/retrieve/pii/037026936890261X.

[140] J. Bailey *et al.*, "Final report on the CERN muon storage ring including the anomalous magnetic moment and the electric dipole moment of the muon, and a direct test of relativistic time dilation," *Nuclear Physics B* **150** (1979) 1–75. http://linkinghub.elsevier.com/retrieve/pii/055032137990292X.

[141] **Muon g-2** Collaboration, G. W. Bennett *et al.*, "Measurement of the Positive Muon Anomalous Magnetic Moment to 0.7 ppm," *Physical Review Letters* **89** no. 10, (2002) 101804. http://link.aps.org/doi/10.1103/PhysRevLett.89.101804.

[142] A. Czarnecki, W. J. Marciano, and A. Vainshtein, "Refinements in electroweak contributions to the muon anomalous magnetic moment," *Phys. Rev. D* **67** (2003) 073006. https://link.aps.org/doi/10.1103/PhysRevD.67.073006.

[143] C. Gnendiger, D. Stöckinger, and H. Stöckinger-Kim, "The electroweak contributions to $(g-2)_\mu$ after the Higgs-boson mass measurement," *Phys. Rev. D* **88** (2013) 053005. https://link.aps.org/doi/10.1103/PhysRevD.88.053005.

[144] B. Krause, "Higher-order hadronic contributions to the anomalous magnetic moment of leptons," *Physics Letters B* **390** no. 1, (1997) 392 – 400. http://www.sciencedirect.com/science/article/pii/S0370269396013469.

[145] A. Kurz, T. Liu, P. Marquard, and M. Steinhauser, "Hadronic contribution to the muon anomalous magnetic moment to next-to-next-to-leading order," *Physics Letters B* **734** (2014) 144 – 147. http://www.sciencedirect.com/science/article/pii/S0370269314003529.

[146] J. Bijnens and J. Prades, "The hadronic light-by-light contribution to the muon anomalous magnetic moment: where do we stand?," *Modern Physics Letters A* **22** no. 11, (2007) 767–782. https://doi.org/10.1142/S0217732307022992.

[147] K. Melnikov and A. Vainshtein, "Hadronic light-by-light scattering contribution to the muon anomalous magnetic moment reexamined," *Phys. Rev. D* **70** (2004) 113006. https://link.aps.org/doi/10.1103/PhysRevD.70.113006.

[148] M. Knecht and A. Nyffeler, "Hadronic light-by-light corrections to the muon $g-2$: The pion-pole contribution," *Phys. Rev. D* **65** (2002) 073034. https://link.aps.org/doi/10.1103/PhysRevD.65.073034.

[149] J. Bijnens, E. Pallante, and J. Prades, "Comment on the pion pole part of the light-by-light contribution to the muon $g-2$," *Nuclear Physics B* **626** no. 1, (2002) 410 – 411. http://www.sciencedirect.com/science/article/pii/S0550321302000743.

[150] J. Prades, E. de Rafael, and A. Vainshtein, "The Hadronic Light-by-Light Scattering Contribution to the Muon and Electron Anomalous Magnetic Moments," *Adv. Ser. Direct. High Energy Phys.* **20** (2009) 303–317. https://www.worldscientific.com/doi/abs/10.1142/9789814271844_0009.

[151] E. de Rafael, "Hadronic contributions to the muon $g-2$ and low-energy QCD," *Physics Letters B* **322** no. 3, (1994) 239 – 246. http://www.sciencedirect.com/science/article/pii/0370269394911142.

[152] C. Aubin, T. Blum, P. Chau, M. Golterman, S. Peris, and C. Tu, "Finite-volume effects in the muon anomalous magnetic moment on the lattice," *Phys. Rev. D* **93** (2016) 054508. https://link.aps.org/doi/10.1103/PhysRevD.93.054508.

[153] D. Bernecker and H. B. Meyer, "Vector correlators in lattice QCD: Methods and applications," *The European Physical Journal A* **47** no. 11, (2011) 148. https://doi.org/10.1140/epja/i2011-11148-6.

[154] **JLQCD** Collaboration, E. Shintani *et al.*, "S Parameter and Pseudo Nambu-Goldstone Boson Mass from Lattice QCD," *Phys. Rev. Lett.* **101** (2008) 242001. https://link.aps.org/doi/10.1103/PhysRevLett.101.242001.

[155] X. Feng, S. Hashimoto, G. Hotzel, K. Jansen, M. Petschlies, and D. B. Renner, "Computing the hadronic vacuum polarization function by analytic continuation," *Physical Review D* **88** no. 3, (2013) 034505. http://link.aps.org/doi/10.1103/PhysRevD.88.034505.

[156] A. Portelli and L. Del Debbio, "Finite volume hadronic vacuum polarisation at arbitrary momenta." Presented at The 33rd International Symposium on Lattice Field Theory, July 2015.

[157] H. B. Meyer and H. Wittig, "Lattice QCD and the anomalous magnetic moment of the muon," *Progress in Particle and Nuclear Physics* **104** (2019) 46 – 96. http://www.sciencedirect.com/science/article/pii/S014664101830084X.

[158] **Fermilab Lattice, HPQCD, and MILC** Collaboration, B. Chakraborty *et al.*, "Strong-Isospin-Breaking Correction to the Muon Anomalous Magnetic Moment from Lattice QCD at the Physical Point," *Phys. Rev. Lett.* **120** (2018) 152001. https://link.aps.org/doi/10.1103/PhysRevLett.120.152001.

[159] E. Shintani, "Progress of lattice calculation of light-by-light contribution to muon g-2," *Nuclear and Particle Physics Proceedings* **273** (2016) 1624–1630.

[160] M. Hayakawa, T. Blum, T. Izubuchi, and N. Yamada, "Hadronic light-by-light scattering contribution to the muon $g-2$ from lattice QCD : Methodology," *PoS* **LAT2005** (2005) 353, arXiv:hep-lat/0509016.

[161] T. Blum, S. Chowdhury, M. Hayakawa, and T. Izubuchi, "Hadronic Light-by-Light Scattering Contribution to the Muon Anomalous Magnetic Moment from Lattice QCD," *Physical Review Letters* **114** no. 1, (2015) 012001. http://link.aps.org/doi/10.1103/PhysRevLett.114.012001.

[162] T. Blum, N. Christ, M. Hayakawa, T. Izubuchi, L. Jin, and C. Lehner, "Lattice calculation of hadronic light-by-light contribution to the muon anomalous magnetic moment," *Phys. Rev. D* **93** (2016) 014503. https://link.aps.org/doi/10.1103/PhysRevD.93.014503.

[163] T. Blum, N. Christ, M. Hayakawa, T. Izubuchi, L. Jin, C. Jung, and C. Lehner, "Connected and Leading Disconnected Hadronic Light-by-Light Contribution to the Muon Anomalous Magnetic Moment with a Physical Pion Mass," *Phys. Rev. Lett.* **118** (2017) 022005. https://link.aps.org/doi/10.1103/PhysRevLett.118.022005.

[164] T. Blum, N. Christ, M. Hayakawa, T. Izubuchi, L. Jin, C. Jung, and C. Lehner, "Using infinite volume, continuum QED and lattice QCD for the hadronic light-by-light contribution to the muon anomalous magnetic moment," arXiv:1705.01067. http://arxiv.org/abs/1705.01067.

[165] J. Green, O. Gryniuk, G. von Hippel, H. B. Meyer, and V. Pascalutsa, "Lattice QCD Calculation of Hadronic Light-by-Light Scattering," *Phys. Rev. Lett.* **115** (2015) 222003. https://link.aps.org/doi/10.1103/PhysRevLett.115.222003.

[166] J. Green, N. Asmussen, O. Gryniuk, G. von Hippel, H. B. Meyer, A. Nyffeler, and V. Pascalutsa, "Direct calculation of hadronic light-by-light scattering," *PoS* **LATTICE2015** (2016) 109, arXiv:1510.08384 [hep-lat].

[167] N. Asmussen, J. Green, H. B. Meyer, and A. Nyffeler, "Position-space approach to hadronic light-by-light scattering in the muon $g-2$ on the lattice," *PoS* **LATTICE2016** (2016) 164, arXiv:1609.08454 [hep-lat].

[168] A. Gérardin, J. Green, O. Gryniuk, G. von Hippel, H. B. Meyer, V. Pascalutsa, and H. Wittig, "Hadronic light-by-light scattering amplitudes from lattice QCD versus dispersive sum rules," arXiv:1712.00421 [hep-lat].

[169] Asmussen, Nils, Gérardin, Antoine, Green, Jeremy, Gryniuk, Oleksii, von Hippel, Georg, Meyer, Harvey B., Nyffeler, Andreas, Pascalutsa, Vladimir, and Wittig, Hartmut, "Hadronic light-by-light scattering contribution to the muon $g-2$ on the lattice," *EPJ Web Conf.* **179** (2018) 01017. https://doi.org/10.1051/epjconf/201817901017.

[170] Asmussen, Nils, Gérardin, Antoine, Meyer, Harvey B., and Nyffeler, Andreas, "Exploratory studies for the position-space approach to hadronic light-by-light scattering in the muon $g-2$," *EPJ Web Conf.* **175** (2018) 06023. https://doi.org/10.1051/epjconf/201817506023.

[171] R. Horsley, Y. Nakamura, H. Perlt, D. Pleiter, P. E. L. Rakow, G. Schierholz, A. Schiller, R. Stokes, H. Stüben, R. D. Young, and J. M. Zanotti, "QED effects in the pseudoscalar meson sector," *Journal of High Energy Physics* **2016** no. 4, (2016) 93. https://doi.org/10.1007/JHEP04(2016)093.

[172] R. Horsley, Y. Nakamura, H. Perlt, D. Pleiter, P. E. L. Rakow, G. Schierholz, A. Schiller, R. Stokes, H. Stüben, R. D. Young, and J. M. Zanotti, "Isospin splittings of meson and baryon masses from three-flavor lattice QCD + QED," *Journal of Physics G: Nuclear and Particle Physics* **43** no. 10, (2016) 10LT02. http://stacks.iop.org/0954-3899/43/i=10/a=10LT02.

[173] **Budapest-Marseille-Wuppertal** Collaboration, S. Borsanyi *et al.*, "Isospin splittings in the light-baryon octet from lattice QCD and QED.," *Physical review letters* **111** no. 25, (2013) 252001. https://inspirehep.net/record/1237923?ln=en.

[174] T. Blum, T. Doi, M. Hayakawa, T. Izubuchi, N. Yamada, and N. Yamada, "Determination of light quark masses from the electromagnetic splitting of pseudoscalar meson masses computed with two flavors of domain wall fermions," *Physical Review D* **76** no. 11, (2007) 114508. http://link.aps.org/doi/10.1103/PhysRevD.76.114508.

[175] Z. Fodor, C. Hoelbling, S. Krieg, L. Lellouch, T. Lippert, A. Portelli, A. Sastre, K. K. Szabo, and L. Varnhorst, "Up and down quark masses and corrections to Dashen's theorem from lattice QCD and quenched QED," arXiv:1604.07112 [hep-lat].

[176] N. Carrasco, V. Lubicz, G. Martinelli, C. T. Sachrajda, N. Tantalo, C. Tarantino, and M. Testa, "QED corrections to hadronic processes in lattice QCD," *Phys. Rev. D* **91** (2015) 074506. https://link.aps.org/doi/10.1103/PhysRevD.91.074506.

[177] **RM123** Collaboration, D. Giusti *et al.*, "Leading isospin-breaking corrections to pion, kaon, and charmed-meson masses with twisted-mass fermions," *Phys. Rev. D* **95** (2017) 114504. https://link.aps.org/doi/10.1103/PhysRevD.95.114504.

[178] Giusti, Davide, Lubicz, Vittorio, Martinelli, Guido, Sanfilippo, Francesco, and Simula, Silvano, "HVP contributions to the muon (g-2) including QED corrections with twisted-mass fermions," *EPJ Web Conf.* **175** (2018) 06006. https://doi.org/10.1051/epjconf/201817506006.

[179] S. Aoki, K.-I. Ishikawa, N. Ishizuka, K. Kanaya, Y. Kuramashi, Y. Nakamura, Y. Namekawa, M. Okawa, Y. Taniguchi, A. Ukawa, N. Ukita, T. Yoshié, and T. Yoshié, "1 + 1 + 1 flavor QCD + QED simulation at the physical point," *Physical Review D* **86** no. 3, (2012) 034507. http://link.aps.org/doi/10.1103/PhysRevD.86.034507.

[180] T. Ishikawa, T. Blum, M. Hayakawa, T. Izubuchi, C. Jung, and R. Zhou, "Full QED+QCD Low-Energy Constants through Reweighting," *Physical Review Letters* **109** no. 7, (2012) 072002. http://link.aps.org/doi/10.1103/PhysRevLett.109.072002.

[181] V. Lubicz, G. Martinelli, C. T. Sachrajda, F. Sanfilippo, S. Simula, and N. Tantalo, "Finite-volume QED corrections to decay amplitudes in lattice QCD," *Phys. Rev. D* **95** (2017) 034504. https://link.aps.org/doi/10.1103/PhysRevD.95.034504.

[182] Z. Davoudi and M. J. Savage, "Finite-volume electromagnetic corrections to the masses of mesons, baryons, and nuclei," *Physical Review D* **90** no. 5, (2014) 054503. http://journals.aps.org/prd/abstract/10.1103/PhysRevD.90.054503.

[183] Z. Fodor, C. Hoelbling, S. Katz, L. Lellouch, A. Portelli, K. Szabo, and B. Toth, "Quantum electrodynamics in finite volume and nonrelativistic effective field theories," *Physics Letters B* **755** (2016) 245 – 248. http://www.sciencedirect.com/science/article/pii/S0370269316000642.

[184] L. Polley, "Boundaries for $SU(3)_c \times U(1)_l$ lattice gauge theory with a chemical potential", journal="Zeitschrift für Physik C Particles and Fields,". https://doi.org/10.1007/BF01555844.

[185] U.-J. Wiese, "C- and G-periodic QCD at finite temperature," *Nuclear Physics B* **375** no. 1, (1992) 45 – 66. http://www.sciencedirect.com/science/article/pii/0550321392903337.

[186] A. Kronfeld and U.-J. Wiese, "SU(N) gauge theories with C-periodic boundary conditions (I). Topological structure," *Nuclear Physics B* **357** no. 2, (1991) 521 – 533. http://www.sciencedirect.com/science/article/pii/055032139190479H.

[187] A. Kronfeld and U.-J. Wiese, "SU(N) gauge theories with C-periodic boundary conditions (II). Small-volume dynamics," *Nuclear Physics B* **401** no. 1, (1993) 190 – 205. http://www.sciencedirect.com/science/article/pii/0550321393903026.

[188] **RC*** Collaboration, M. Hansen, B. Lucini, A. Patella, and N. Tantalo, "Gauge invariant determination of charged hadron masses," *Journal of High Energy Physics* **2018** no. 5, (2018) 146. https://doi.org/10.1007/JHEP05(2018)146.

[189] G. E. P. Box and M. E. Muller, "A Note on the Generation of Random Normal Deviates," *The Annals of Mathematical Statistics* **29** no. 2, (1958) 610–611. http://projecteuclid.org/euclid.aoms/1177706645.

[190] M. Lüscher, "A portable high-quality random number generator for lattice field theory simulations," *Computer Physics Communications* **79** no. 1, (1994) 100–110. http://www.sciencedirect.com/science/article/pii/0010465594902321.

[191] **RBC and UKQCD** Collaboration, C. Allton *et al.*, "Physical results from 2 + 1 flavor domain wall QCD and SU(2) chiral perturbation theory," *Physical Review D* **78** no. 11, (2008) 114509. http://link.aps.org/doi/10.1103/PhysRevD.78.114509.

[192] **RBC/UKQCD** Collaboration, P. A. Boyle *et al.*, "The kaon semileptonic form factor in N f = 2 + 1 domain wall lattice QCD with physical light quark masses," *Journal of High Energy Physics* **2015** no. 6, (2015) 164. http://link.springer.com/10.1007/JHEP06(2015)164.

[193] **RBC and UKQCD** Collaboration, T. Blum *et al.*, "Domain wall QCD with physical quark masses," *Phys. Rev. D* **93** (2016) 074505. https://link.aps.org/doi/10.1103/PhysRevD.93.074505.

[194] **Budapest-Marseille-Wuppertal** Collaboration, A. Portelli *et al.*, "Electromagnetic corrections to light hadron masses," *PoS* **LATTICE2010** (2010) 121, arXiv:1011.4189 [hep-lat].

[195] **RM123** Collaboration, G. M. de Divitiis *et al.*, "Isospin breaking effects due to the up-down mass difference in lattice QCD," *Journal of High Energy Physics* **2012** no. 4, (2012) 124. https://doi.org/10.1007/JHEP04(2012)124.

[196] C. Aubin, T. Blum, M. Golterman, and S. Peris, "Model-independent parametrization of the hadronic vacuum polarization and g-2 for the muon on the lattice," *Phys. Rev. D* **86** (2012) 054509. https://link.aps.org/doi/10.1103/PhysRevD.86.054509.

[197] J.-W. Lee and B. C. Tiburzi, "Finite volume corrections to the electromagnetic mass of composite particles," *Phys. Rev. D* **93** (2016) 034012. https://link.aps.org/doi/10.1103/PhysRevD.93.034012.

[198] M. E. Matzelle and B. C. Tiburzi, "Finite-Volume Corrections to Electromagnetic Masses for Larger-Than-Physical Electric Charges," arXiv:1702.01296. http://arxiv.org/abs/1702.01296.

[199] J. W. Cooley and J. W. Tukey, "An algorithm for the machine calculation of complex Fourier series," *Math. Comp.* **19** (1965) 297–301. https://doi.org/10.2307/2003354.

[200] R. Barrett, M. Berry, T. F. Chan, J. Demmel, J. Donato, J. Dongarra, V. Eijkhout, R. Pozo, C. Romine, and H. van der Vorst, *Templates for the Solution of Linear Systems: Building Blocks for Iterative Methods*. Society for Industrial and Applied Mathematics, 1994.

[201] P. Boyle, A. Yamaguchi, G. Cossu, and A. Portelli, "Grid: A next generation data parallel C++ QCD library," arXiv:1512.03487. http://arxiv.org/abs/1512.03487.

[202] Wolfram Research, Inc., "Mathematica, Version 10.4.1." http://www.wolfram.com/mathematica/, 2016.

[203] G. P. Lepage, "A new algorithm for adaptive multidimensional integration," *Journal of Computational Physics* **27** (1978) 192–203.